Title
Biologically Inspired Photocatalytically Active Membranes for Water Treatment

Author
Kinsinger, Nichola

Publication Date
2013

UNIVERSITY OF CALIFORNIA
RIVERSIDE

Biologically Inspired Photocatalytically Active Membranes for Water Treatment

A Dissertation submitted in partial satisfaction
of the requirements for the degree of

Doctor of Philosophy

in

Chemical and Environmental Engineering

by

Nichola M Kinsinger

June 2013

Dissertation Committee:
    Dr. David Kisailus, Chairperson
    Dr. Sharon Walker
    Dr. Mark Matsumoto

The Dissertation of Nichola M Kinsinger is approved:

____

____

____
Committee Chairperson

University of California, Riverside

ACKNOWLEDGMENTS

First, I would like express my appreciation to my advisor Dr. David Kisailus for his guidance and support throughout my PhD research. I would also like to thank my dissertation committee members, Dr. Sharon L. Walker and Dr. Mark Matsumoto, for their advice and guidance through this process. I would like to extend my appreciation to all of the professors in the Chemical and Environmental Engineering Department and staff members for their aid and support.

I am also grateful to all of the members of Dr. Kisailus' lab group, current and former, specifically Dr. Dongsheng Li, Dr. Lessa Grunenfelder, John Johnson, Christopher Salinas, and Wenting Hou. Special thanks to the undergraduate researchers who worked with me throughout my graduate career including Ashley Wong, Fabian Villalobos, Luke Turalich, Ian Miller, Alexander Dudchenko, Kyle Nelson, Letia Solomon, Christian Alcaraz, Nataly Dakak, Pablo Cortez, and Taahira Major.

I am very thankful and grateful to the Department of Defense, Office of Naval Research who funded my National Science and Engineering Graduate Fellowship which has supported me and my research during the last three years.

Lastly, I would like to thank my family and friends for all of their support and encouragement specifically, my mother, Sue Kinsinger who is a strong, professional woman role model and always supports me, and my husband, Jordan Barta who also supports and encourages me to pursue my education.

DEDICATION

This dissertation is dedicated to my mother, my late father, Thomas Kinsinger, and my husband for all of their love, support, and encouragement in all of my endeavors.

ABSTRACT OF THE DISSERTATION

Biologically Inspired Photocatalytically Active Membranes for Water Treatment

by

Nichola M Kinsinger

Doctor of Philosophy, Graduate Program in Chemical and Environmental Engineering
University of California, Riverside, June 2013
Dr. David Kisailus, Chairperson

There is an alarming increase of a variety of new chemicals that are now being discharged into the wastewater system causing increased concern for public health and safety because many are not removed by typical wastewater treatment practices. Titanium Dioxide (TiO_2) is a heterogeneous photocatalytic material that rapidly and completely mineralizing organics without harmful byproducts. TiO_2 is synthesized by various methods, which lack the necessary control of crystal size, phase, and morphological features that yield optimized semiconductor materials. Mineralizing organisms demonstrate how nature can produce elegant structures at room temperature through controlled organic-mineral interactions.

Here, we utilize biologically-inspired scaffolds to template the nucleation and growth of inorganic materials such as TiO_2, which aid in controlling the size and phase of these particles and ultimately, their properties. Nanosized rutile and anatase particles were synthesized under solution conditions at relatively low temperatures and mild pH conditions. The effects of reaction conditions on phase and grain size were investigated and discussed from coordination chemistry and coarsening mechanisms. Photocatalytic characterization of TiO_2 phase mixtures was performed to investigate their synergistic effect. The suspension conditions of these catalytic nanomaterials were modulated to optimize the degradation rate of organic analytes.

Through the addition of an organic scaffold during the synthesis reaction, a mechanically robust (elastic) composite material containing titanium dioxide (TiO_2) nanoparticles was produced. This composite was subsequently heat-treated to produce a porous, high surface area TiO_2 nanoparticulate membrane. Processing conditions were investigated to characterize the growth and phase transformation of TiO_2, which ultimately impacts photocatalytic performance. These bulk porous TiO_2 structures can be fabricated and tailored to act as stand-alone photocatalytic membranes, eliminating the need for nanoparticle recovery systems, thereby reducing processing costs and increasing amount of viable applications of photocatalytic systems.

TABLE OF CONTENTS

ACKNOWLEDGMENTS iv

DEDICATION v

ABSTRACT OF THE DISSERTATION vi

TABLE OF CONTENTS viii

LIST OF FIGURES xii

LIST OF TABLES xx

Chapter 1. Introduction 1

- 1.1 Motivation and Background. 2
  - 1.1.1 Current Organic Contaminants and Water Resources. 2
  - 1.1.2 Current Water Treatment Technologies. 6
- 1.2 Photocatalytic Oxidation of Organic Contaminants. 9
  - 1.2.1 Historic Overview. 9
  - 1.2.2 Photocatalyst Oxidation Processes. 10
  - 1.2.3 Titanium Dioxide as a Photocatalyst Material. 11
  - 1.2.4 Current Heterogeneous Photocatalytic Reactor Designs. 16
  - 1.2.5 Application of Titania nanoparticles. 17
- 1.3 Synthesis of Titanium Dioxide. 21
  - 1.3.1 Vapor Phase Synthesis. 21
  - 1.3.2 Solution-based Synthesis. 22
  - 1.3.3 Sintering. 23
- 1.4 Biologically Inspired Synthesis of TiO_2. 24

1.5 Objective and Scope. 25

1.5.1 Specific Objectives. 27

Chapter 2. Nucleation and crystal growth of nanocrystalline anatase rutile phase TiO_2 from a water soluble precursor 30

Abstract 31

2.1 Introduction 32

2.2 Preparation of materials. 34

2.3 Material Characterizations. 34

2.4 Results and Discussion. 35

2.4.1 Hydrothermal Conditions: pH, organometallic precursor, time. 36

2.4.2 Phase Development. 40

2.4.3 Growth Mechanism. 46

2.5 Conclusions 51

Chapter 3. Synergistic Effect of pH and Phase in a Nanocrystalline Titania Photocatalyst 52

Abstract 53

3.1 Introduction. 54

3.2 Experimental. 57

3.2.1 Preparation of materials. 57

3.2.2 Material Characterization. 57

3.2.3 Photocatalytic Performance. 59

3.3 Results and Discussion. 60

3.3.1 Material Characterization. 60

3.3.2 Kinetics of Photocatalytic Degradation: Effect of pH and Anatase-Rutile Ratio. 66

3.4 Conclusions....75

3.5 Acknowledgements....76

Chapter 4. Photocatalytic Titanium Dioxide Composite 77

Abstract....78

4.1 Introduction....79

4.2 Preparation of materials. 81

4.3 Material Characterization. 83

4.4 Results and Discussions....85

4.4.1 Phase development....85

4.4.2 Structural characterization of TiO_2-polymer composite. 92

4.5 Conclusion. 95

Chapter 5. Grain growth and phase transformation within porous photocatalytic membrane....96

Abstract....97

5.1 Introduction....99

5.2 Materials and Methods....102

5.2.1 Material Characterization....103

5.2.2 Photocatalytic Performance. 106

5.3 Results and Discussion. 107

5.3.1 Isochronal Crystal growth and phase transformation. 107

5.3.2 Isothermal Crystal growth and phase transformation. 115

5.3.3 Photocatalytic Characterization of Selected Isochronally Fired Materials. .124

5.3.4 Effect of reduced processing temperature on crystal growth and phase transformation. 128

5.4 Conclusions. 143

5.5 Acknowledgements. 144

Chapter 6. Conclusions 145

Chapter 7. References 153

Appendix. Investigation of Processing Parameters for Enhanced Membrane Structural Integrity 179

Introduction. 180

Materials and Methods. 182

Material Characterization. 182

Results and Discussions. 183

Conclusions. 191

Appendix References. 192

LIST OF FIGURES

Figure 1: EDCs levels in different water samples [1, 15]. 4

Figure 2: General mechanism of photocatalytic oxidation of water to produce hydroxyl radicals that rapidly and completely mineralize organics. Light with energy greater than the bandgap of the heterogeneous photocatalytic material excites an electron from the valance band to the conduction band creating a hole (h^+) in the valance band which oxidizes water absorbed on the surface to produce hydroxyl radicals[42]. 11

Figure 3: Schematic of photoexcitation in TiO_2 with the potential de-excitation events. D represents the electron donor species; A represents the electron acceptor species; (-) represents the excited electron; (+) represents the hole [45]. 14

Figure 4: Schematic of electron transfer between rutile and anatase TiO_2 particles resulting in a photocatalytic reaction [70]. 16

Figure 5: Schematic of nanoparticle implementation for a water or wastewater treatment plant. 19

Figure 6. X-ray diffraction of TiO_2 nanocrystals formed at 150°C and A) pH 7.8, B) pH 9, C) pH 10, D) pH 11 versus time. 38

Figure 7. FTIR spectra of TiO_2 nanocrystals formed at 150°C for A) 1 hour at different pH conditions and B) 12 hours at different pH conditions; C) at pH 7.8 as a function of increasing time, and D) pH adjusted precursor prior to heat treatment (liquid FTIR samples). 39

Figure 8. Illustrations of the TiO_6 octahedral arrangements in a) rutile, b), anatase, and c) brookite. 41

Figure 9. A) Structure of TiBALDH with dashed lines demonstrating its octahedral structure. B) Illustration of TiBALDH precursor with hydrolytically stable lactato ligands, forcing condensation along the z-axis. C) Illustration of TiBALDH cleavage by nucleophilic attack by the OH- at the a) Ti metal center and at b) bi-dentate ligands (shown by blue dotted lines) which allows for two condensation reactions in the x-y plane of the coordination sphere to occur simultaneously, yielding edge-sharing bonds. 43

Figure 10. Bright field TEM images of TiO_2 synthesized at pH 7.8 / 150°C. Selected area diffraction patterns inserted for phase identification........ 47

Figure 11. Bright field TEM images of rutile and anatase (circled) TiO2 crystals synthesized at pH 9 at 150°C for a) 12 hours and b) 72 hours. Selected area diffraction patterns and d-spacing measurements (3.51Å: (101) planes of anatase; 3.24Å: (110) places of rutile) inserted for phase identification. 48

Figure 12. Bright field TEM images of Anatase TiO_2 crystals synthesized at pH 11 / 150°C for a) 12 hours and B) 72 hours with subsequent crystallite size distributions........ 50

Figure 13: A) X-Ray diffraction patterns and B) Bright field TEM micrographs (with selected area diffraction patterns inserted) of mixed phase TiO_2 (Anatase/Rutile) formed hydrothermally at pH = 9, 150ºC at different times. 63

Figure 14: Zeta potential curves of the mixed phase TiO_2 nanoparticles with increasing relative rutile concentration, suspended in 0.01M NaCl solution........................ 65

Figure 15: Bright field TEM micrographs of anatase TiO_2 particles synthesized at pH = 9, 150°C for 36 hours suspended at a) pH = 4, b) pH = 7, and c) pH = 10 with subsequent particle size distributions.. 66

Figure 16: Photocatalytic degradation of MB versus time. Reactions were performed using TiO_2 suspensions (500mg/L TiO_2, 1mW/cm^2 UV light intensity) at A) pH = 4, B) pH = 7, C) pH = 10. D) Initial degradation rate of MB versus % rutile in TiO_2 suspensions at pH = 4, 7, and 10 (lines drawn only as a guide). 68

Figure 17: A) Proposed mechanism of charge separation between anatase and rutile during photocatalysis. B) Proposed mechanism of charge separation between anatase and rutile during photocatalysis at different suspension pHs on charge transfer to oxidation and reduction species... 72

Figure 18: a) Bright field TEM micrographs of TiO_2 particles without Pt nanocrystal deposition, Pt deposition on 12% rutile material for 6 hr at pH = 7 b) Low magnification, c) high magnification, d) energy dispersive spectra of photocatalyst materials post Pt deposition at pH4 (TEM image not shown) and pH7. Selected area electron diffraction patterns are inserted for phase identification. EDS spectra are representative spectra from five regions samples. 74

Figure 19. X-ray diffraction of TiO_2 nanocrystals formed at 150°C, pH 9 with A) No PVA added, B) PVA:Ti 1:100,000, C) PVA:Ti 1:100 with increasing reaction

time, and D) PVA:Ti 1:100 with increasing annealing temperature in air. (* indicates crystalline PVA). 87

Figure 20. A) Anatase crystallite diameters (calculated using the Scherer equation using FWHM values obtained via XRD) with and without PVA with increasing reaction durations. B) FTIR spectra of TiO_2 nanocrystals formed at 150°C pH 9 with PVA (PVA:Ti ratio 1:100,000), with increasing reaction time. 89

Figure 21. Bright-field TEM micrographs of TiO_2-polymer composites annealed in air for 1 hour at A) 25°C, B) 400°C, C) 600°C, and D) 800°C. Selected Area Diffraction Patterns (SADP, inserted in the top right of each micrograph) were used for phase identification. 90

Figure 22. A) Image of TiO_2-PVA composite (directly from the reactor) formed from hydrothermal reaction at 150°C. SEM images of cube-sections of TiO_2-PVA composites after annealing in air for 1 hour at B) 400°C, C) 600°C, and D) 800°C. E) Specific surface area and crystallite diameters of TiO_2-polymer composites with increasing annealing temperatures demonstrating the reduction of surface area with significant grain growth. 91

Figure 23. A) Illustration of polymer interactions to form the elastic composite structure. B) X-Ray elemental maps and a SEM image of the sectioned TiO_2-Polymer composite (without annealing)... 92

Figure 24. TGA analyses of A) PVA only B) FTIR spectra of TiO_2-PVA composites formed at 150°C pH 9, annealed at increasing temperatures................................ 94

Figure 25: Representative X-ray Diffraction patterns of A) TiO_2 powders without PVA; B) TiO_2 prepared with PVA (composites). 109

Figure 26: Anatase and Rutile crystal size and percent rutile of composite materials versus firing temperature A) TiO_2 powders without PVA; B) TiO_2 prepared with PVA (composites). 110

Figure 27: TGA of A) TiO_2 powders without PVA; B) TiO_2 prepared with PVA (composites) under the different air flow conditions. 112

Figure 28: Synchrotron map of membrane fired at 800°C for 1 hour at an air flow rate of $10cm^3/min$. A) X-ray transmission map (relative to sample thickness), B) percentage of rutile (0-100% scale), C) percentage of rutile (0-60% scale) and D) optical micrograph of scanned sample. 114

Figure 29: Pore size distributions of composite materials after firing as measured using N_2 adsorption. 115

Figure 30: Crystal sizes of anatase and rutile, and fraction of rutile versus temperature at air flow rates of 10cc/min and 100cc/min. 117

Figure 31: Plot of the function $y=(D_a/D_0)^3/(1-\alpha)-1$ versus time for composites fired at A) 800°C, B) 850°C, and C)900°C with air flow rates of $10cm^3/min$ and $100cm^3/min$ to model rutile interface and surface nucleation. D) Plot of ideal function y with phase 1 IN and phase 2 IN and SN identified. 122

Figure 32: Photocatalytic degradation of MB versus time. Reactions were performed using TiO_2 materials prepared by firing 150°C composites at A) $10cm^3/min$ and B) $100cm^3/min$ air flow suspended at pH = 7 (500mg/L TiO_2, $1mW/cm^2$ UV light

intensity) and C) Initial degradation rate of MB versus temperature at air flow rate of 10cm^3/min and 100cm^3/min (lines drawn only as a guide). 126

Figure 33: Specific surface area (as determined by low pressure 5-point BET adsorption) of composite materials initially prepared at 150°C and subsequently annealed in air. 126

Figure 34: XRD patterns for the green composite materials synthesized at pH9 80°C for 15 minutes, 1 hour, and 12 hours; * denotes crystalline PVA peaks, • denotes broad amorphous peak, † denotes broad anatase peak. 129

Figure 35: XRD patterns for the isochronally fired composite materials synthesized at pH = 9 for 12 hours at 80°C (top); 150°C (middle); and (bottom) anatase and rutile crystallite sizes, percent rutile vs. annealing temperature................................. 132

Figure 36: Transmission Electron Microscope micrographs of membrane materials initially prepared at 80°C for 12 hours and subsequently heated isochronally at 400°C, 600°C, 700°C, and 800°C for 1 hour.. 133

Figure 37: Representative Scanning Electron Microscope micrograph of a porous membrane initially prepared at 80°C for 1 hour and subsequently fired at 800°C for 1 hour.. 134

Figure 38: A) Anatase and Rutile crystal diameters and % Rutile vs. Temperature (as determined by XRD) for samples initially synthesized at pH = 9 at 80°C and 150°C for 12 hours without PVA and subsequently annealed at 400°C, 600°C, 700°C and 800°C for 1 hour. B) Anatase and Rutile crystal diameters and %

Rutile vs. Temperature for samples prepared at 80°C for different synthesis durations: 15minutes, 1, 2, and 12 hours. 135

Figure 39: Differential Scanning Calorimetry of composites initially prepared at 80°C and 150°C and heated at 10°C/min to 800°C in argon flowing at 20cm^3/min. .. 137

Figure 40: (a) Pore size distribution of membrane materials, initially prepared at 80°C and annealed at different temperatures, (b) pore size distribution of the composite material initially prepared at 80°C and fired at 800°C for 1 hour, and (c) low resolution Scanning Electron micrograph of a membrane initially prepared at 80°C for 15 minutes, and fired at 800°C for 1 hour. 140

Figure 41: EDS maps of 1mm^2 area of green composites: Red-Carbon; Blue-Titanium142

Figure 42: Future POU application of this membrane technology. 152

Figure 43: X-ray diffraction of membrane (fired at 800°C, 1 hour, 100cm^3/min) prior to secondary growth and after secondary growth at 200°C for 3 hours under acidic solution conditions. 184

Figure 44: Scanning Electron Micrographs of membrane following secondary growth at 200°C for 3 hours under acidic solution conditions and subsequent firing at 800°C for 1 hour in air. 185

Figure 45: Scanning Electron Micrograph of nanoparticles prepared by hydrothermal synthesis for 3 hours at 200°C under acidic conditions.................................... 186

Figure 46: X-ray diffraction of nanoparticles prepared by hydrothermal synthesis for 3 hours at 200°C under acidic conditions 187

Figure 47: Scanning Electron Micrograph of nanoparticles prepared by hydrothermal synthesis for 3 hours at 200°C under acidic conditions (without membrane, on the left) and particle size distribution of the corresponding preparation conditions (on the right). 189

Figure 48: Scanning Electron Micrograph of TiO_2 nanoparticles prepared by hydrothermal synthesis for 3 hours at 200°C under acidic conditions. 190

LIST OF TABLES

Table 1: Removal performance of EDCs by treatment processes [1, 2]. 7

Table 2. Frequencies of the $\nu(OCO)_{asym}$ and $\nu(OCO)_{sym}$ for 25°C reaction with increasing pH (liquid FTIR samples). 45

Table 3. Frequencies of the $\nu(OCO)_{asym}$ and $\nu(OCO)_{sym}$ for pH 7.8 reaction with increasing time. 45

Table 4: Surface area vs. Percentage of rutile... 63

Table 5: Fitted interface and surface nucleation model parameters 123

Table 6: Percentage of organic removal by membrane materials fired at 700°C under both $10cm^3$/min and $100cm^3$/min.. 127

Table 7: Average surface area (as determined by low pressure 5-point BET adsorption) of composite materials initially prepared at 80°C and subsequently annealed in air. 141

Chapter 1.
Introduction

1.1 Motivation and Background.

Rising amounts of new chemicals are being discharged into the wastewater system due to the rapid emergence of technology and industry. The increasing sensitivity of current measurement techniques has led to the identification of new contaminants that were previously thought to be removed by drinking and wastewater treatments, but were below the detection limit. The presence of such compounds is causing increased concern for public health and safety [1]. Pharmaceuticals and personal care products (PPCPs), surfactants, and various industrial chemicals were previously not believed to be problematic are known to be endocrine disrupting compounds (EDCs) and are currently not removed by typical wastewater treatment practices [1]. To accommodate the ever-increasing demand for clean drinkable water and the alarming increase in the use of personal care products and pharmaceuticals (PCPPs), new treatment methods must be implemented to remove these hazardous compounds and to degrade them to non-harmful constituents.

1.1.1 Current Organic Contaminants and Water Resources.

Pharmaceuticals and personal care products (PPCPs), surfactants, and various industrial chemicals are known to be endocrine disrupting compounds (EDCs) and are currently not removed by typical wastewater treatment practices. An EDC is defined by the United States Environmental Protection Agency (EPA) as “an exogenous agent that interferes with synthesis, secretion, transport, metabolism, binding action, or elimination of natural blood-borne hormones that are present in the body and are responsible for homeostasis, reproduction, and developmental process" [2-4]. Although there are varying opinions on the definition of EDCs, three major classes of these compounds that are generally accepted are estrogenic, androgenic, and thyroidal [2]. The estrogenic and androgenic compounds mimic or block natural estrogen and testosterone respectively, and the thyroidal compounds affect the thyroid [2]. EDCs also include a variety of natural and synthetic chemicals used as industrial solvents/lubricants and their byproducts, plastics, plasticizers, pesticides, fungicides, and pharmaceutical agents [4]. With the increase of industry (especially the research and production of pharmaceuticals), the spectrum of these compounds is continuing to expand along with their unknown potential health risks [1, 5-7].

Within California, water management has been recognized as a critical issue to ensure the state's wealth and economic well-being [8]. This includes conveyance and quality of water throughout the state [8]. In order to support the population and economy, Southern California imports up to 70% of its water supply, mostly from Northern California, for approximately 18 million people and its agricultural areas [8, 9]. This is causing concerns over environmental, economical, and societal impacts to the Sacramento-San Joaquin Delta, Mono Basin, and Owens Valley [8, 9]. There is continued industry and population growth in Southern California and the costs of water development are increasing due to the associated environmental costs and impacts [9, 10]. Water recycling is becoming increasingly necessary to address the increasing demands of Southern California and to mitigate the environmental impacts on Northern California's waterways as it cannot be assumed that the supply will fully recover [8, 9, 11, 12]. Many water supplies are currently supplemented inadvertently with treated wastewater effluent discharged into rivers, streams, and lakes that are used downstream as drinking water sources [1, 13, 14].

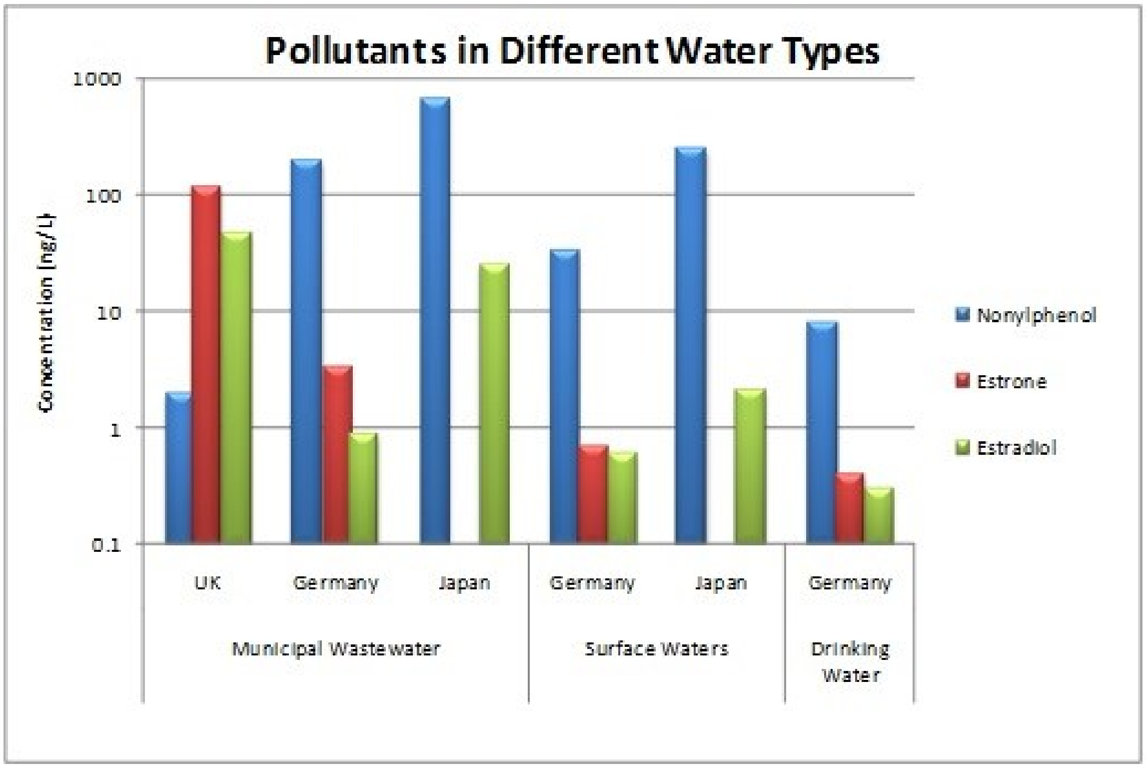

Figure 1: EDCs levels in different water samples [1, 15].

Worldwide there is also a growing crisis of limited clean fresh water sources causing concern for human health as well as ecological concerns with the emergence of these untreated compounds in the wastewater effluent. EDCs and PPCPs have been found in drinking water sources both domestically and internationally on the order of μg/L to ng/L, indicating that the current wastewater treatment technologies are not adequately removing these compounds (as illustrated in Figure 1) [1, 15-19]. The increased use of such waters to supplement drinking water sources is increasing concern over health and safety [1, 12, 13, 20]. Many such compounds have long half lives designed for the benefit of the industrial and pharmaceutical applications[4]. Since these compounds do not decay easily, even compounds banned decades ago are still observed in the environment[4]. Other such EDCs may not be as persistent however, but are so frequently used such as Bisphenol A (BPA) that there is high human exposure. Despite the low concentration of various compounds typically observed, the broad spectrum of compounds that may have additive or synergistic health effects and since there is a significant lag between exposure and the manifestation of symptoms causes great human and ecological health concern[4, 19, 21].

In areas of water scarcity, wastewater recycling and aquifer recharge are attractive to augment water supplies. Since it was first introduced in 1961, reclaimed wastewater in Los Angeles county is currently composed one-third of the water used to recharge aquifers [14]. However, such use of wastewater effluents to increases the likelihood of such contaminants occurring in drinking water [5, 6]. One of the most challenging aspects of such water reuse is the large variety of compounds that may be present from consumer and household, industrial, and agricultural sources and the inability to detect their presence [5, 6]. These compounds are typically low in concentration (<1μg/L), which is below the minimum testing concentration currently set by the Food and Drug Administration (FDA) [1, 5, 6]. Even though this concentration is far below therapeutic doses, little is known about the long-term chronic exposure to a cocktail of organic compounds which may include PPCPs and compounds not designed for human consumption such as flame retardants, solvents, dyes, and fuels [5, 6]. Alarmingly, one study detected a combination of 11-17 different organics in finished water from a drinking water treatment facility [19].

1.1.2 Current Water Treatment Technologies.

Existing water and wastewater treatment facilities are mostly designed for the removal of the well-known "priority" pollutants specified in current regulations [1, 5, 19, 22-24]. Typical wastewater treatment systems include treatment of the influent by a series of stages: pretreatment, primary sedimentation, biological reactor and secondary sedimentation. The pretreatment involves coarse and fine screening to remove large matter in the liquid stream and aeration chambers to remove grit and fat. Following the pretreatment, the primary sedimentation stage uses compounds to flocculate and coagulate the suspended particles to aid in sedimentation. The biological reactor breaks down the biodegradable compounds in the water using activated sludge processes. The secondary sedimentation removes the activated sludge from the water stream following the bioreactor with the supernatant being the effluent from the wastewater treatment plant [17]. Additional treatment stages maybe added which may include the addition of chlorine or some disinfecting agent to the effluent stream after leaving the secondary sedimentation process depending on treatment requirements [20].

Within the wastewater treatment system or even within a drinking water treatment system, various options are available for advanced treatment processes depending on the source water and contaminants present. Some common, effective treatment processes to treat such contaminants previously discussed are Powder Activated Carbon (PAC), Chlorination, and Ozonation (Table 1) [1, 24]. However, PAC adsorbs the compounds but does not degrade the compounds; instead, PAC transfers the contamination to a new phase[1, 25, 26]. Several hydrophobic compounds have been observed to be persistent even after activated carbon filtration [19]. Chlorination is a common disinfectant and oxidizer used to treat potential pathogens and has been shown to react with many such organic contaminants. Unfortunately, chlorination frequently produces chlorinated byproducts that may be more hazardous (such as trihalomethanes (THMs) [24, 27]. EDCs and PPCPs have been found in drinking water sources on the order of µg/L to ng/L, indicating that the current wastewater environmental, and drinking water treatment processes are not adequately removing these compounds causing increasing concern for public health and safety [1, 16, 17, 19, 28, 29].

Table 1: Removal performance of EDCs by treatment processes [1, 2].

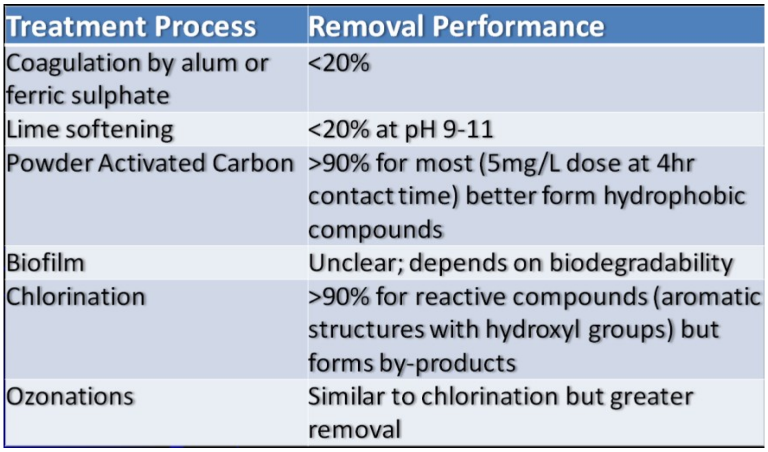

Treatment Process	Removal Performance
Coagulation by alum or ferric sulphate	<20%
Lime softening	<20% at pH 9-11
Powder Activated Carbon	>90% for most (5mg/L dose at 4hr contact time) better form hydrophobic compounds
Biofilm	Unclear; depends on biodegradability
Chlorination	>90% for reactive compounds (aromatic structures with hydroxyl groups) but forms by-products
Ozonations	Similar to chlorination but greater removal

Membrane filtration is another advanced treatment technology that has received increased attention since reverse osmosis can be used to treat brackish or salt water to drinking water quality standards [30, 31]. Membranes are typically polymer based made from cellulose acetate and polysulfone for example supported by a porous structural substrate [30]. There are two operating geometries typically used which include dead-end and cross-flow filtration [30]. There are four general categories that are used to describe membrane filtration based on the size of the impurities that are removed: microfiltration (MF), ultrafiltration (UF), nanofiltration (NF), and reverse osmosis (RO) [30]. Typically, MF and UF are used for separation of particulate from liquid streams where NF and RO can be used to remove solutes [30, 31]. RO can effectively remove such residual contaminants however the due to the small pores sizes required for this level of filtration significant pressures are required increasing operating costs and limiting applications since typical household water pressures are below the necessary pressure (minimum pressure for RO, ca. 200 psig, which is much higher than the 80 psig of a typical household) [30, 32]. An effective alternative is NF since the molecular weight cutoff can be as low as 100g/mol, which is lower than many EDCs and pharmaceuticals such as ibuprofen and estradiol. NF can operate at pressures as low as 70psig which is feasible for a household application [30]. However ,biofouling and scaling our major limitations with such membrane filtration processes [30, 31]. Back flushing or brief treatment with an acid can be used to remove biological films and dissolve scale formation however this requires down time and degrades the polymer material of the membrane [30].

1.2 Photocatalytic Oxidation of Organic Contaminants.

1.2.1 Historic Overview.

In 1918 TiO_2 became available as a new white pigment to replace lead oxide due to its known deleterious health effects [33, 34]. With the introduction of this new pigment, the paints deteriorated more rapidly by fading and "chalking" (development of a powder layer on surface) when exposed to sunlight [33, 35, 36]. Based on these observations there were many photoactivity studies performed dating back to the 1930's that document the photo-bleaching of dyes by various oxides such as TiO_2, ZnO, and Sb_2O_3 which all absorb in the UV region [35, 36]. Additional oxides were observed to have a similar affect just not as rapid and these oxides absorbed light below UV light energies which is associated with the bandgap energy of the materials [36]. However, the reduced bandgap relates to a reduced oxidation and/or reduction potential of the materials [37].

Further investigation into this observed photoactivity resulted in numerous studies that focused on zinc oxide in the 1950's in which the production of hydrogen peroxide was observed [38]. This ability was of great interest due to the possibility of converting solar energy into a chemical system [38]. In the last 40 years, TiO_2 became the primary focus for photocatalytic studies due to the discovery by Fujishima and Honda of its ability to effectively photocatalytically split water [39-41].

1.2.2 Photocatalyst Oxidation Processes.

A promising treatment technology is photocatalytic degradation of such emerging contaminants via hydroxyl radical (OH•) oxidation. The Environmental Protection Agency has inventoried and verified more than 800 compounds that that are effectively mineralized by OH• [42]. OH• completely mineralizes a broad range of compounds to carbon dioxide and water under ambient conditions [42-48]. Complete mineralization of the pollutant eliminates the concern of secondary byproducts that are formed when using other oxidation agents such as chlorine [27, 49-51]. There are many methods to produce OH• with the aid of ultra-violet radiation (UV) such as hydrogen peroxide, ozone, semiconductors [47]. While all of these processes produce OH• when coupled with UV, semiconducting materials are distinctly advantageous since they are heterogeneous catalysts that can be integrated and isolated from the effluent liquid stream to be recycled and reused in the system [43].

The general mechanism of radical generation by a semiconducting material is illustrated in Figure 2. Light with energy ($h\nu$) greater than the bandgap of the material excites an electron from the valence band to the conduction band. The charge vacancy (hole, h+) in the valence band left by the excited electron subsequently oxidizes adsorbed water on the surface of the catalyst producing OH• that rapidly and completely mineralizes organics to carbon dioxide, water, and inorganic acids [42, 43, 52-55]. The excited electron (e^-) in the conduction band reduces dissolved oxygen absorbed on the catalyst surface that may also participate in the degradation reactions[42, 43, 52-55]. The hole can also perform as the oxidizing agent by oxidizing the contaminant directly bypassing the water oxidation step [41].

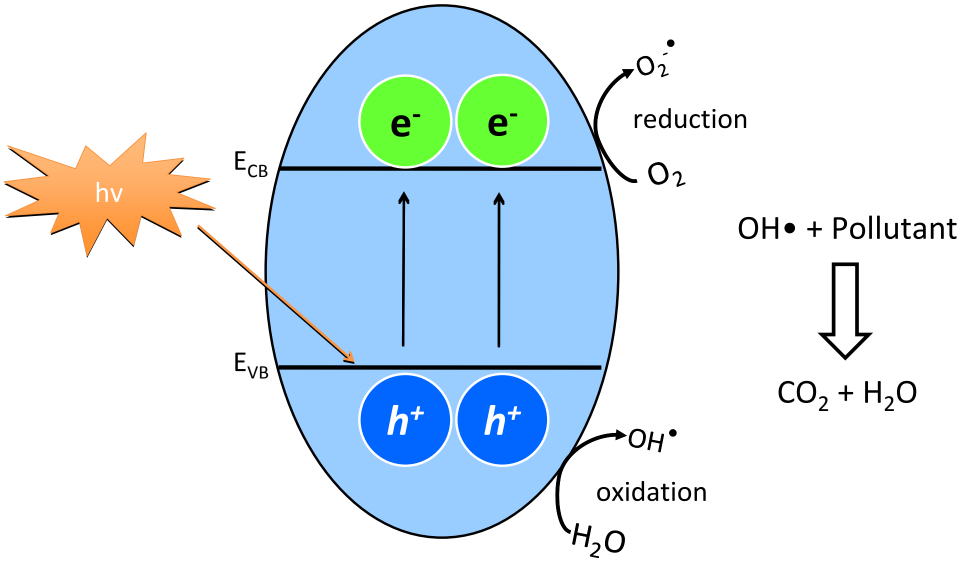

Figure 2: General mechanism of photocatalytic oxidation of water to produce hydroxyl radicals that rapidly and completely mineralize organics. Light with energy greater than the bandgap of the heterogeneous photocatalytic material excites an electron from the valance band to the conduction band creating a hole (h^+) in the valance band which oxidizes water absorbed on the surface to produce hydroxyl radicals[42].

1.2.3 Titanium Dioxide as a Photocatalyst Material.

Titanium dioxide (TiO_2) has been widely used as an advanced semiconductor for many years and has been demonstrated to be effective as a heterogeneous photocatalyst for the oxidation of organic compounds in water when exposed to UV irradiation [43, 47, 52-54, 56, 57]. TiO_2 is an inexpensive semiconducting material that has an energy band gap of approximately 3.0 to 3.2 eV, small enough that electrons in the valence band can be excited to the conduction band by the UV portion of the electromagnetic spectrum [45, 46]. The UV energy (hν) is equal to or greater than this bandgap thereby exciting a valence electron to the conduction band as discussed in Figure 2 [42, 45, 49].

Titanium is the fourth most abundant metal and the ninth most abundant element component in the earth's crust (~0.63%) [34, 45]. It is found bound in minerals like ilmentite (titanium iron oxide) and perovskite (calcium titanium oxide), in addition to the more pure mineral forms of titanium dioxide: anatase, brookite, and rutile (which may contain up to 10% iron impurities) [34]. Approximately 98% of the world's production of TiO_2 is used for pigments; however in the last 40 years, it has become the focus of photocatalytic research since the discovery by Fujishima and Honda of its ability to photocatalytically to split water [34, 39]. Nanoceramics, such as TiO_2, have attracted much attention or their unique properties such as photoactivity, corrosion resistance, high surface area, phase stability, and enhanced sinterability [58-63]. Such advanced ceramics are 17% of a multibillion dollar ceramic industry and with such a large industry there is constant competition to become more efficient and to reduce processing costs [63]. TiO_2 specifically is very attractive material for such applications since it is inexpensive, abundant, photo-stable, and non-toxic [25, 26, 64, 65]. In 2005, approximately 2000 tons of nanoscale TiO_2 were produced, 65% of which were used for personal care products such as topical sun screens and cosmetics and is even used as pigments if food products [66].

1.2.3.1 Crystal Phases of Titanium Dioxide.

Three photocatalytically relevant phases of TiO_2 are anatase, brookite, and rutile; however, anatase and rutile have been observed to be the most photocatalytically active phases. Rutile is considered the thermodynamically stable phase of TiO_2; anatase and brookite, metastable phases, will eventually transform to rutile irreversibly and exothermally [67]. Phase stability has been shown to be dependent on crystal size: anatase is more stable than rutile at crystallite diameters less than 14nm, and rutile more stable at crystal diameters greater than 35nm [61, 67, 68].

All three phases are composed of $[TiO_6]$ octahedra. Anatase and rutile are arranged in tetragonal unit cells; anatase composed of 50% edge and corner sharing bonds between octahedra, whereas rutile is composed of 80% corner sharing bonds between its octahedra [67]. The distinct structural transformation from anatase and rutile requires the breaking 7 out of 24 Ti–O bonds per unit cell [69].

1.2.3.2 TiO_2 Photocatalytic Limitations.

Multiple events can occur upon electron excitation in a semiconducting material. With sufficient time, electrons and holes can undergo charge transfer from the surface of the particle to an adsorbed species. However, over time, these electrons and holes will recombine and not be able to participate in the formation of radicals and thus, be detrimental towards the photooxidation of the pollutants. There are four pathways for de-excitation illustrated in Figure 3; two of the pathways result in electron and hole recombination. Recombination can be accelerated by both surface and bulk defects, or by unavailability of electron donors or acceptors. Therefore, having pre-adsorbed species (pollutants) on the surface of the catalyst will increase the efficiency of the electron or hole transfer [45]. One factor affecting heterogeneous photocatalysis is the specific surface area. The degradation rate of organics is dependent on the charge transfer to an adsorbed species; therefore, the greater the surface area of catalyst, the higher the rate of oxidation.

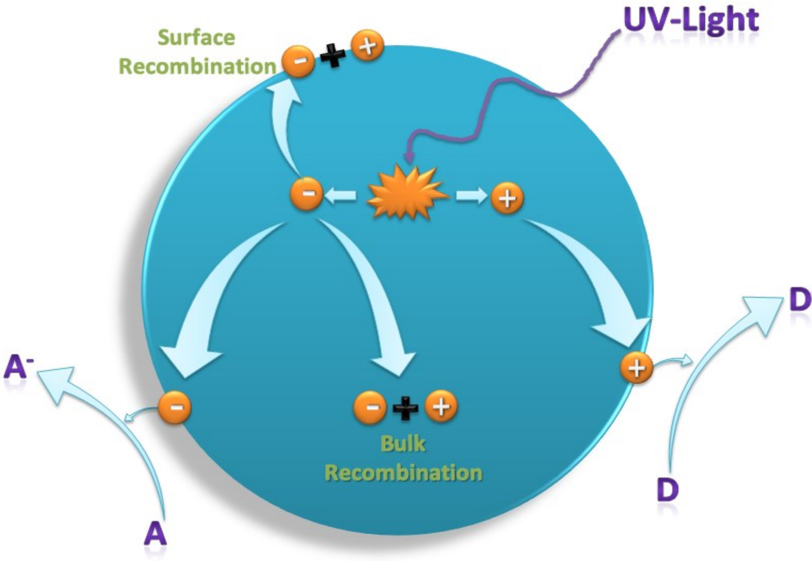

Figure 3: Schematic of photoexcitation in TiO_2 with the potential de-excitation events. D represents the electron donor species; A represents the electron acceptor species; (-) represents the excited electron; (+) represents the hole [45].

1.2.3.3 Benefits of mixed phase TiO_2 photocatalyst.

Anatase, a metastable phase of TiO_2, has been shown to be more photocatalytically active than the thermodynamically stable rutile phase (which is the stronger photoabsorber due to the reduced bandgap). The two relevant phases of TiO_2 utilized in this research are anatase and rutile. These phases exhibit different bandgaps (3.0eV for rutile and 3.2eV for anatase). Mixed phase TiO_2 (anatase and rutile), such as the commercially available powder Degussa P25, has been shown to perform more efficiently than pure anatase or rutile phase TiO_2 particles as photocatalysts [70, 71]. The improved performance of the anatase and rutile mixed phase photocatalysts is attributed to a synergistic effect that is greater than the sum of the individual performance of anatase and rutile. One proposed mechanism suggests that since rutile (3.0eV) has a slightly lower band gap energy than the anatase (3.2eV) and increases the probability to promote electrons to the conduction band in the rutile particle. In the presence of anatase, the excited electron in the rutile particle can be transferred to the anatase particle. This inhibits the electron and hole recombination and thereby overcomes the main limitation of TiO_2 photocatalysts [70, 71]. The mechanism of the electron transfer between the different particles (anatase and rutile) is not clearly understood, but it is clear that the presence of both phases greatly improves the photocatalytic activity [71]. The ratio of anatase to rutile for optimum photocatalytic activity is debatable due to the differences in the synthesis processes and particles sizes. Figure 4a shows the difference in the band gap energies of rutile and anatase particles resulting in a greater number of electron and hole pairs created in the rutile particle than the anatase. Figure 4b demonstrates one suggested theory as to how the electrons transfer from the rutile to the anatase particle due to the conduction band bending. Since an electron is transferred from the rutile to the anatase particle, there are fewer electrons than holes which reduces the probability of electron-hole recombination improving the photocatalytic activity [70].

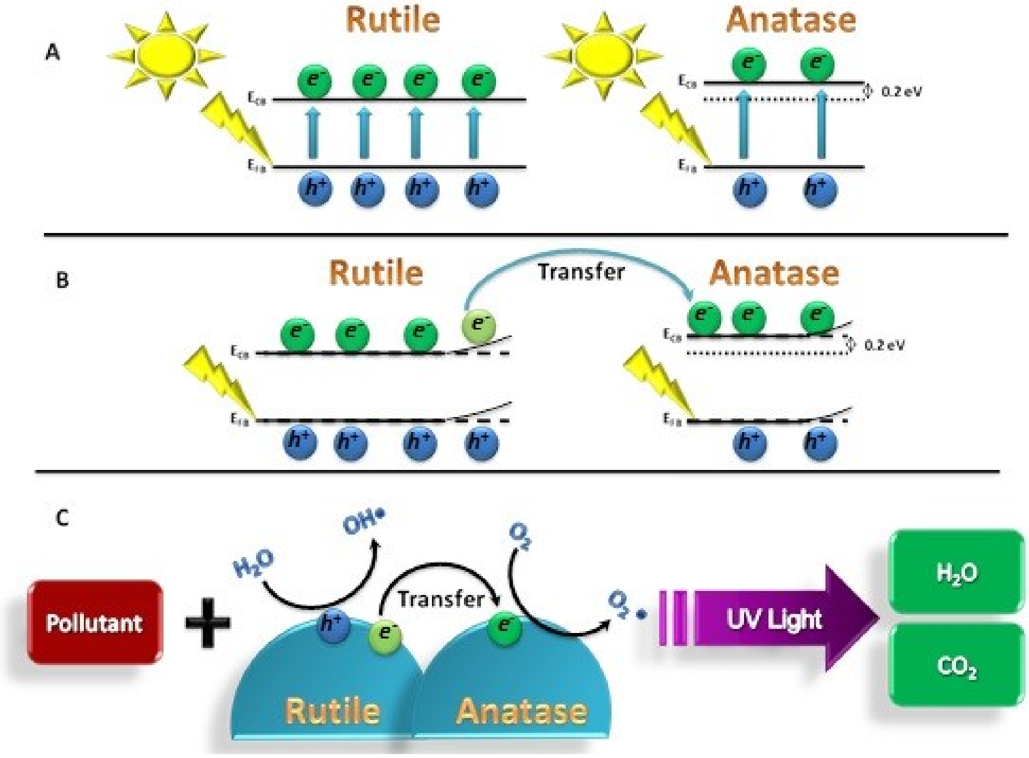

Figure 4: Schematic of electron transfer between rutile and anatase TiO_2 particles resulting in a photocatalytic reaction [70].

1.2.4 Current Heterogeneous Photocatalytic Reactor Designs.

One viable method for large scale photocatalytic applications involves immobilizing the TiO_2 on a substrate and designing a flow-through reactor to accommodate the contaminant loading [72]. The catalyst is therefore easily separated from the effluent liquid stream. However, immobilization greatly diminishes the surface area to volume ratio, which reduces the activity since photocatalysis is a surface phenomenon. The degree to which the activity is reduced depends on the design of immobilization [73]. If the TiO_2 is immobilized on Raschig rings, or a porous support, the penetration of the

UV light to the center of the reactor will be limited, however the available surface area is increased. Sunlight or artificial light can be used as the excitation source. Since UV light only constitutes 5% of the solar spectrum, employing artificial UV light will enhance the photocatalytic activity. To improve the performance of the solar photocatalysts (using the solar UV), aluminum sheeting can be placed behind the reactor [26, 64]. The pipe diameters are small to ensure adequate penetration of the high energy light from the sun into the reactor. The addition of a reflecting material behind the reactors ensures maximum irradiation of the photocatalyst [42].

1.2.5 Application of Titania nanoparticles.

By increasing the available active sites on the titania, the photocatalytic properties of the catalyst will improve. It has been shown that nanopowders improve the efficiencies by increasing the surface area to volume ratio, which minimizes the amount of material not exposed to the excitation source and reaction environment [42, 43]. The next step beyond using powders is using nanoparticles, which can increase the surface area by a factor of six.

1.2.5.1 Lab Scale Application.

Typically photocatalytic activity of a material is studied in the lab by monitoring the reaction in a batch reactor setup. The one design cycles a suspension of the catalyst and the organic compounds past a UV light source, through the annular reactor. Another design cycles a suspension upward through the reactor [44, 46]. Such batch reactor setups are very effective for determining reaction rates and comparing different photocatalysts, but are not practical for a full scale water treatment plant.

1.2.5.2 Large Scale Application.

For large scale applications, the degradation of the organic compounds can not operate as a batch reactor as the lab scale systems were designed for testing. Additionally, the nanoparticles can not be simply discharged into either a natural environment or the water distribution system. The particles need to be easily removed from the liquid stream after the photocatalytic reactor, then the particles can be recycled back into the reactor system. Figure 5 is an illustration of the integration of nanoparticles for the treatment of water. First, the liquid stream from the treatment plant is mixed with the TiO_2 nanoparticles. The suspension then flows though the photocatalytic reactor where it is irradiated with an artificial or natural UV light source. The suspension is transferred into a sedimentation basin to remove the nanoparticles from the suspension, similar to processes used in traditional water treatment.

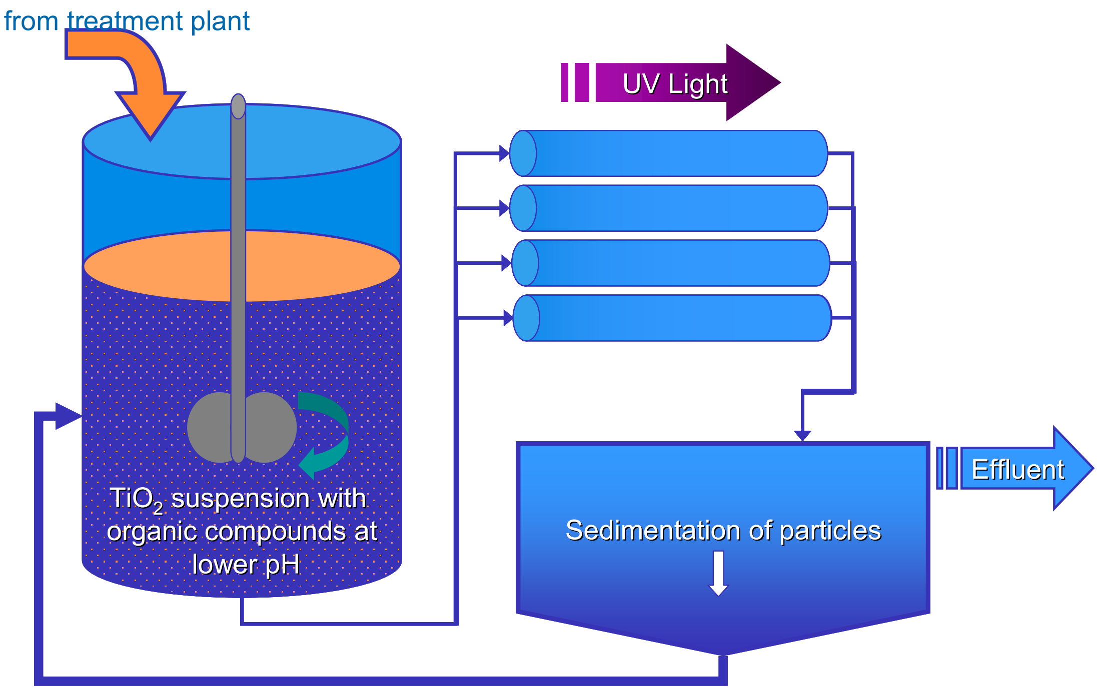

Figure 5: Schematic of nanoparticle implementation for a water or wastewater treatment plant.

When using nanoparticles, the stability of the particles in solution must be taken into account. To ensure that the maximum surface area is utilized, the water must be maintained at a pH lower or higher than the isoelectric point of the photocatalyst material [74]. By lowering or raising the pH, the particles will acquire a net positive or negative charge, thereby repelling each other due to the electrostatic repulsion [30]. According to DVLO (Derjaguin and Landau, Verwey and Overbeek) theory, the primary energy barrier must be greater than $15k_BT$ to greatly decrease the occurrence of aggregation (where k_B is the Boltzmann constant and T is temperature). This energy barrier corresponds to approximately ± 0.5 pH units of the isoelectric point [75].

The disadvantage of using nanoparticles is the difficulty in separating the catalyst from the "clean" effluent so it remains in the reactor (i.e., packed bed reactor with the catalyst on a support) or to recycle it back into the system (slurry reactor where the catalyst is not on a support). Removal of the catalyst by filtration would require a filter on the order of 10 nm, which would require the capital cost similar to reverse osmosis and nanofiltration. To overcome this issue, the energy barrier of the DVLO theory can be utilized. Reducing the energy below the $15k_BT$ energy barrier (versus remaining above $15k_BT$, which will maintain particle stability) induces rapid flocculation of the particles. Raising the pH of the solution to within the ± 0.5 pH range of the isoelectric point will reduce the energy barrier [75]. Coincidentally, the isoelectric point of TiO_2 is near neutral pH of water [74]. Once the nanoparticles are aggregated, they can then be settled out of the suspension and mechanically removed. However, smaller aggregates of titania nanoparticles have been observed in wastewater effluent despite the aggregation and sedimentation processes [76].

Since the TiO_2 nanoparticles are catalysts, they are not consumed during the reaction and can be reused. As previously discussed, particles can be separated as large aggregates, but will greatly diminish the degradation efficiency. The DLVO theory does not predict the redispersion of the particles that is caused by the continued increase of pH [75]. However, the particles will begin to redisperse due to the increasing electrostatic repulsion (assuming a moderate ionic strength that remains constant). By rapidly mixing the large aggregates into a low pH solution, the aggregates will break up due to the electrostatic repulsion and the shear force of mixing. To ensure that the particles are thoroughly dispersed before entering the photocatalytic reactor, rapid mixing or sonication can be used in addition to mixing the TiO_2 nanoparticles in a lowered pH media.

1.3 Synthesis of Titanium Dioxide.

1.3.1 Vapor Phase Synthesis.

Physical and Chemical Vapor Deposition (PVD, CVD) are techniques typically used to form coatings on substrates to improve electrical, thermal, optical, and corrosion resistance properties, however they can also be used to synthesis a variety of nanomaterials [77]. Typical synthesis via CVD consists of injection of a gaseous precursor into the vacuum chamber at temperatures ranging from 200°C to 1600°C [78], which will react or decompose on a substrate within the chamber. Crystal size, phase, and morphology can be controlled by the reactor temperature, substrate material, gas flow rate, precursor concentration, and total amount of precursor supplied [77]. PVD is similar to CVD except there is no precursor reaction. Materials, such as a titanium metal, are evaporated in an oxygen environment and then deposited onto a cool substrate [77].

Flame spray pyrolysis (FSP) is another vapor phase technique used to prepare ultrafine titanium dioxide [79]. Metal salts and metallo-organics can be used as precursors; however chelated alkoxides are often used to reduce specialized handling since they are less reactive with water [79, 80]. The precursor solution, in an alcohol solvent, is the fuel aerosol that is injected into a combustion zone. Oxygen is used as the atomizing gas and as the co-reactant during the combustion, which both vaporizes the aerosol and decomposes the precursor ligands, which then generates particles after condensation reactions occur between metal-oxygen species. Once particles are formed, they will continue to grow by either vapor deposition or cluster-collision [79]. This is an attractive technique because the particles are of high purity and crystallinity typically not requiring secondary thermal treatments. However this technique requires high temperatures which makes it costly [81].

1.3.2 Solution-based Synthesis.

Hydrothermal synthesis utilizes aqueous phases at elevated temperatures (>100°C) and pressures (dictated by solvent vapor pressure at reaction temperature) to crystallize TiO_2 directly from solution in steel autoclave reactors [77, 82]. A variety of precursor can be used such as metals salts and metallo-organics similar to FSP [83]. Hydrothermal routes to TiO_2 are advantageous since it has been shown to produce crystalline products at relatively low temperatures (<300°C) [53, 77, 84-89]. Modifications of hydrothermal conditions such as temperature, pH, reagent, time, etc., enable precise control of phase, morphology, and composition [53, 77, 85, 90]. This is particularly important where TiO_2 is used as a photocatalyst. TiO_2 is synthesized by various methods such as chemical and physical vapor deposition, which require high temperatures or extreme atmospheric conditions (e.g., high vacuum) to achieve the desired phase, shape, and size of the material [54, 77]. Solution processes such as hydrothermal routes offer more environmentally friendly and lower cost processing, while achieving atomic mixing of constituent elements.

1.3.3 Sintering.

Sintering is an annealing process of joining particles together and therefore, transforming powders into bulk materials using heat [58, 91]. Sintering is a traditional ceramic processing technique that is also used to remove the organic binder used during the gelation process and yielding nearly 100% dense parts [58, 91]. During annealing, larger grains will grow at the expense of other smaller grains to reduce surface area and thus, Gibbs free energy. After a ceramic part has been shaped as a green body, it must be fired (typically at temperatures from 500°C – 1800°C) to remove the binder and pores, develop interparticle connectivity throughout the material via sintering, and densify.

Similar to sintering, secondary thermal treatments are also frequently used following low temperature syntheses (such as hydrothermal) to remove organic impurities, increase crystallinity, and induce phase transformations to the thermally stable phases [77, 92]. During this thermal processing of TiO_2, there are three modes of phase transformation from anatase to rutile: (i) interfacial, (ii) surface, and (iii) bulk. They are dictated by temperature, crystal size, number of contacts, and surface defects [69, 93]. At lower firing temperatures (~400°C-800°C), thermal fluctuations on the surface and within the bulk of anatase are not enough to induce transformation of anatase to rutile. However anatase-anatase interactions can form rutile-like elements and serve as a rutile nucleation site, reducing the activation energy for rutile nucleation versus that of bulk or surface nucleation[69, 93]. Similarly, thermal fluctuations on the surface and within the bulk form rutile-like elements that serve as rutile nucleation sites at higher temperatures. Sintering and phase transformation of nanocrystalline materials occurs at lower temperatures than coarse crystals, which greatly affects processing conditions, time, and cost [58, 62, 69, 79]. Coarse anatase materials lack large numbers of interfaces for interfacial nucleation and reduced surface area for surface nucleation of rutile. Therefore, increased sintering temperature and time of nanocrystalline material will favor surface and bulk nucleation of rutile [69, 93].

1.4 Biologically Inspired Synthesis of TiO_2.

There are a wide variety of synthesis techniques used to prepare TiO_2, however many require high temperatures or extreme pH conditions [54, 77, 94]. However, solution-based technologies lack the necessary control of crystal size, phase, and morphology that afford semiconductor materials an optimized performance. Nature has evolved efficient strategies, exemplified in biomineralizing systems, to synthesize materials that demonstrate nanostructural control and desirable properties [95]. It is generally thought that the combination of soluble molecules in conjunction with the underlying structural organics provides the requisite binding sites and molecular arrangement for inducing nucleation of oriented crystals with a stabilized phase (e.g., the stabilized aragonite phase of $CaCO_3$ found in nacre) [95]. Many of these soluble molecules consist of acidic residues that have a high affinity for cations, thereby facilitating their attraction and thus increasing local supersaturation levels [96-98].

In addition, the interfacial energy between the organic template and the mineral precursor should have a significant influence towards heterogeneous nucleation by reduction of the surface free energy. After the initial nucleation has occurred, crystals may grow by a number of mechanisms including, but not limited to, the attachment of additional ions or by mesophasic self-assembly. These kinetically controlled crystallization processes are achieved by modifying the interactions of nuclei and developing crystals with soluble molecules and organic scaffolds. These interactions play a critical role in determining the particle size, habit, morphology and phase of the resulting mineral [99].

1.5 Objective and Scope.

Based on inspiration from biology, which often uses these organic structures to guide nucleation and growth of minerals, we demonstrate controlled synthesis of TiO_2 using a hydrophilic synthetic polymer. Through the addition of the synthetic polymer, a TiO_2-organic composite is formed that can be annealed to form a bulk, porous semiconducting structure that can be used as a porous flow-through membrane. The bulk composite TiO_2-organic structures can be fabricated and tailored to act as stand-alone photocatalysts, eliminating the need for nanoparticle recovery systems that are necessary for slurry styled reactors. The elimination of necessary recovery systems opens the application of this technology for large and small applications such as point-of-use (POU) in residential and commercial application to large municipal applications.

In California approximately 7000 million gallons per day (MGD) are withdrawn for public supply of which approximately 82% is withdrawn was from surface waters which serves 93% of the population [100]. More and more of our drinking water sources are being threatened due to the increasing presence of organics found in our surface waters do to effluent discharge [5, 101, 102]. Four out of ten Americans use point of use treatment to units (which range in cost from $20 to several hundred dollars) as drinking water can reasonably be expected to contain trace contaminants due to incomplete treatment or leaks in the distribution system [32]. Therefore there is a need and a large market for a technology that not only removes, but also treats such compounds at the POU.

China and India have alarming increases in water-borne contaminants and will need to utilize POU systems. China, for example, makes up 21% of the world's population, yet they only have access to 7% of the world's watersheds [31]. The likelihood that emerging pollutants will be present in drinking water will continue to increase as population continues to increase [5, 100]. This technology will reduce the public exposure to organic pollutants that are persistent even after current municipal wastewater treatments, environmental degradation, and/or existing drinking water treatments. The end-user application will also reduce concerns about deterioration of water quality (i.e., existence of industrial and pharmaceutical compounds) due to aquifer recharge, discharge into waterways, and water recycling in regions with limited fresh water resources [103].

The current scope of the photocatalytically active TiO_2 membrane is for residential or small business point-of-use applications (POU, such as under-cabinet or refrigerator water filters for residential), which supplement municipal water treatment processes. Current point-of-use devices in the United States and other developed countries include filter pitchers, filters attached to faucets, distillers, and reverse osmosis units. The development and implementation of this technology will reduce the public exposure to organic pollutants that are persistent even after tradition wastewater treatments, environmental degradation mechanisms, and/or drinking water treatments. The end-user application will also reduce concerns about deterioration of drinking water sources (i.e. existence of industrial and pharmaceutical compounds) due to aquifer recharge, discharge into waterways, and water recycling in regions with limited fresh water resources [103].

The progress towards the development of the photocatalytic membrane technology is outlined in this thesis. The overall objectives towards were (i) understand crystal growth and phase development of a metal oxide semiconductor from a water soluble precursor; (ii) understand structure-function relationships between TiO_2 phase and photocatalytic activity; (iii) develop a bulk, porous semiconducting (TiO_2) structure used for photocatalytic treatment of water; (iv) understand effect of processing parameters on crystal growth and phase transformation within the metal oxide membrane.

1.5.1 Specific Objectives.

Objective 1: Study the effect of pH and synthesis time on the crystal growth and phase development using a water soluble precursor, specifically Titanium bis(ammonium lactato) dihydroxide (TiBALDH), to control the anatase-rutile ratio for improved photocatalytic performance.

This investigation revealed that using the water stable precursor specific phase and mixed phase is controlled by reaction pH and time. At pH = 7.8, solely rutile is formed independent of reaction time; at a reaction pH greater than 10, solely anatase is formed independent of reaction time. At pH = 9, the initial phase was anatase with subsequent formation and transformation to rutile with increasing reaction time. This investigation revealed that at the lower pH conditions (i.e., pH = 7.8 and 9), the primary growth mechanism was oriented attachment due to lower solubility product of TiO_2 while oriented attachment-based growth results in the phase transformation to rutile at pH = 9. At higher pH conditions (i.e., pH = 10 and 11), where the solubility product is greatly increased (two orders of magnitude greater at pH = 11 versus pH = 9), dissolution and recrystallization (Ostwald Ripening) is the primary growth mechanism resulting in a broad crystal size distribution.

Objective 2: Investigation of the effect of anatase-rutile ratios on the photocatalytic degradation of an analyte dye under different solution pH (i.e. 4, 7, 10).

This study investigated the effect of anatase-rutile mixtures and pH on the photocatalytic degradation of Methylene blue dye as the target analyte using the mixed phase TiO_2 materials prepared in the first objective. The photocatalytic characterization was conducted at pH = 4, 7, and 10, which showed that reactivity and efficiency of the photocatalysts were significantly affected by the particle-particle and sorbate-surface interactions. pH = 7 was ideal to observe the effect of percent rutile on the degradation rate, where 91% was removed within 120 minutes by the material composed of 20% rutile, and is attributed to the synergistic charge transfer of holes from rutile to anatase.

Objective 3: The development of a bulk porous photocatalytically active membrane, using the water soluble precursor TiBALDH and a synthetic polymer, which can be used for water treatment POU applications and does not require downstream recovery systems.

The introduction of the synthetic polymer during the synthesis of TiO_2 from TiBALDH yielded a viscoelastic composition that formed via crosslinking between the polymer and the precursor and/or the hydrolyzed TiO_2 nanoparticles. X-ray Diffraction and Transmission Electron Microscopy analysis revealed 2nm anatase crystals within the organic matrix. Subsequent firing to remove the polymer resulted in grain growth of the anatase crystals and after sufficient temperature (800°C), transformation to rutile.

Objective 4: The investigation of the effects of processing parameters (such as firing time, air flow rate during firing, and initial synthesis temperature of the composite) on the development of porous photocatalytically active membranes using the water soluble precursor TiBALDH and a synthetic polymer.

Air flow rate was observed to have a significant effect on the resulting porous TiO_2 material since the synthetic polymer (binder) is removed by combustion. Increasing the air flow rate showed higher removal of the organic at lower temperatures, this resulted in more rapid formation of rutile. Kinetic experiments were performed to identify the phase transformation mechanism: interfacial, surface, or bulk nucleation. We observed that these mechanisms are not only temperature dependent, but because of the low inorganic densities in our membranes, they are also density dependent. This is related to reduced anatase-anatase interactions. Reduction in processing temperature (composite synthesis temperature) was observed to reduce the subsequent firing temperatures required to achieve the initial phase transformation to rutile due to increased presence of amorphous TiO_2 within the material.

Chapter 2.

Nucleation and crystal growth of nanocrystalline anatase rutile phase TiO_2 from a water soluble precursor

Reprinted with permission from *Crystal Growth and Design*. Copyright (2010) American Chemical Society.

Kinsinger, N. M.; Wong, A.; Li, D.; Villalobos, F.; Kisailus, D., Nucleation and Crystal Growth of Nanocrystalline Anatase and Rutile Phase TiO2 from a Water-Soluble Precursor. *Crystal Growth & Design* **2010,** *10* (12), 5254-5261.

Abstract

Titanium dioxide (TiO_2) has been widely used as an advanced semiconductor and as a white pigment for many years. In recent years, TiO_2 has gained much more interest for its semiconducting properties for use as photocatalytic and photovoltaic materials. Understanding the fundamental nucleation and growth mechanisms is crucial to controlling microstructure and properties for these applications. Nanosized rutile and anatase particles were synthesized from a water-soluble titanium (IV) precursor using a hydrothermal method. The impact of various hydrothermal conditions on the formation, phase, morphology, and grain size of the TiO_2 products were investigated using XRD, TEM, and FTIR. At near neutral pH, aggregated rutile rods are formed. By increasing the alkalinity of the reaction medium, the anatase phase was favored and, as expected, larger particle sizes resulted from longer duration reactions. The effects of reaction conditions are discussed with respect to coordination chemistry and coarsening mechanisms.

2.1 Introduction

Titanium dioxide (TiO_2) has been widely used as an advanced semiconductor and as a white pigment for many years [52-54]. There are a wide variety of synthesis techniques used to prepare TiO_2, however many require high temperatures or extreme pH conditions [54, 77, 94]. Hydrothermal routes to TiO_2 are advantageous since it has been shown to produce crystalline products at relatively low temperatures (<300°C) [53, 77, 86-89]. Modifications of hydrothermal conditions such as temperature, pH, reagent, time, etc., enable precise control of phase, morphology, and composition [53, 77]. This is particularly important where TiO_2 is used as a photocatalyst. TiO_2 shows great potential for being able to completely mineralize a wide variety of toxic compounds (both air and water-based pollutants) via photooxidative reactions [42, 54, 59]. Anatase, a metastable phase, has been shown to be the more photocatalytically active than the thermodynamically stable rutile phase. However, Degussa P25 (75% anatase and 25% rutile), has been shown to out perform both pure anatase and rutile TiO_2 [70, 71]. Since the phase stability of anatase and rutile are dependent on crystallite size and surface chemistry, the Ti precursor chosen for synthesis directly affects phase development and ultimately, catalyst performance [52, 59, 104-106]. By understanding the hydrolysis and condensation reactions of these precursors as well as their subsequent nucleation and growth mechanisms, we can control TiO_2 phase transformations and resulting microstructures that effect specific material properties. Hoebbel et al. investigated the effect of different multidentate ligands on the hydrolysis of Al, Zr, and Ti-metal complexes. In their work, they demonstrated that the hydrolytic stability was strongly dependent on the structure of the ligand, with saturated beta-diketones having the strongest hydrolytic stability followed by unsaturated beta-diketones and beta-ketoesters [107]. Measurements of hydrolysis and condensation rate constants [108-112] have shown that hydrolysis reactions can be inhibited by complexing transition metals such as iron with EDTA. This complexation will force condensation reactions due to charge modifications induced from these complexes [113]. Thus, the nucleofugacity of the leaving group will directly affect the rate of hydrolysis, as the nucleophilic OH- (strong Lewis base) will donate an electron, weakening the bond to another ligand, enabling separation of a nucleofugal group from the metal center [113, 114]. Thus, the ligand-metal interaction is critical in controlling the hydrolytic stability of the complex.

Titanium (IV) bis(ammonium lactato) dihydroxide (TiBALDH) is a water soluble, non-hazardous titanium complex that is stable at near neutral pH and ambient conditions. TiBALDH has been shown to produce uniform anatase nanoparticles via thermohydrolysis [115]. In our study, we know that a bidentate lactato ligand, with a strong affinity for the Ti atom, will indeed resist hydrolysis relative to monodentate ligands such as alkoxides [114]. In this specific study, our aim is to discuss the relative hydrolytic stability of the lactato ligand with respect to hydroxyl ions that compete as nucleophiles. We demonstrate control over the phase development of TiO_2 via a hydrothermal synthesis method using careful control of synthesis parameters. We also provide an understanding of the phase development and growth of TiO_2 from TiBALDH.

2.2 Preparation of materials.

TiO_2 nanocrystals were chemically synthesized under hydrothermal conditions. Titanium bis(ammonium lactato) dihydroxide (TiBALDH) solution, 50 wt % in water, was purchased from Sigma Aldrich. 1M TiBALDH solutions were prepared by diluting with de-ionized (DI) water. The pHs of these solutions were modified with Ammonium Hydroxide (30 wt % purchased from Acros Organics). Immediately following pH modification, solutions were placed in 23 mL, Teflon-lined hydrothermal reactors (Parr Instruments, Moline, IL) and heated at 150°C for different durations (1 - 72 hours) in convection ovens. Reactors were removed and subsequently cooled under ambient conditions. The resulting products were washed with DI water, sonicated (Branson 2510) for 30 minutes between washes to remove any unreacted precursor and reaction by-products, and then were dried in air at 100°C for 24 hours.

2.3 Material Characterizations.

TiO_2 specimens were characterized using X-Ray Diffraction (XRD), Transmission Electron Microscopy (TEM), and Fourier Transform Infrared Spectroscopy (FTIR). Phase identification was determined by XRD analysis (Philips X'Pert) using Cu $K\alpha$ radiation. Using the XRD diffraction patterns, crystallite diameters of anatase and rutile crystals were calculated based on the (2 0 0) and (2 1 0) reflections, respectively, from the Scherer formula (equation 1):

$$D_{(hkl)} = \frac{\kappa\lambda}{\beta\cos\theta} \tag{1}$$

where κ is the shape factor, λ the wavelength of the Cu Kα radiation, β the full width at half maximum (FWHM) of the (h k l) peak, and θ is the diffraction angle. In order to corroborate these results, specimens were observed using TEM (T-20 and Titan, FEI) bright field imaging and electron diffraction analyses. TiO_2 nanocrystals were dispersed in ethanol, sonicated (Branson 2510) for 30 minutes, and subsequently deposited onto ultrathin carbon films on holey carbon supports with a 400 mesh copper grid (Ted Pella).

FTIR was used to determine the extent of the hydrolysis reaction (by identifying the presence / absence of the lactato ligands) and presence of residual polymer. Samples with no visible product were prepared by placing a droplet onto salt plates. Powder samples were prepared by grinding Potassium Bromide (KBr) with 1% of the TiO_2 sample in a mortar and pestle, and drying for 4 hours at 100°C. 100 mg pellets were pressed using an KBr Pellet 13 mm die (International Crystal Laboratories, #0012-2477) at 6000 psig and analyzed (50 scans) using a Bruker Equinox 55 FTIR instrument from 4000 cm^{-1} to 400 cm^{-1} at increments of 2 cm^{-1}.

2.4 Results and Discussion.

Titanium (IV) bis(ammonium lactato) dihydroxide (TiBALDH) is a water soluble, non-hazardous titanium complex that is stable at near neutral pH and ambient conditions. TiBALDH has been shown to produce uniform anatase nanoparticles via thermohydrolysis [115]. In our study, we know that a bidentate lactato ligand, with a strong affinity for the Ti atom, will indeed resist hydrolysis relative to monodentate ligands such as alkoxides [114]. In this specific study, our aim is to discuss the relative hydrolytic stability of the lactato ligand with respect to hydroxyl ions that compete as nucleophiles. We demonstrate control over the phase development of TiO_2 via a hydrothermal synthesis method using careful control of synthesis parameters. We also provide an understanding of the phase development and growth of TiO_2 from TiBALDH.

2.4.1 Hydrothermal Conditions: pH, organometallic precursor, time.

Titanium dioxide (TiO_2) has three crystalline forms: rutile, anatase, and brookite. Anatase and brookite are metastable phases and will eventually transform to rutile. Traditional synthesis methods drive this transformation via an annealing step (~ 750°C) [53]. However, hydrothermal processing of TiO_2 has been used to produce anatase and/or rutile under milder temperatures by adjusting the reaction medium conditions [59, 105, 116].

The effects of pH and time on the resulting phase of TiO_2 produced from TiBALDH were investigated. Figure 6a depicts x-ray diffraction patterns of TiO_2 synthesized at near neutral pH (~ pH 7.8, no exogenous base added) with increasing durations. At short reaction times (ca. 12 hours), crystalline rutile (JCPDS #01-073-1765) is the only phase observed. With increasing time, the crystal size of rutile increases from 12.1 ± 3.1 nm after 12 hours to 17 ± 0.7 nm after 72 hours reaction time. By increasing the pH of the reaction media, the formation of anatase was observed. The resulting phase of the TiO_2 synthesized at pH 9 is primarily crystalline anatase (JCPDS # 01-084-1286) initially (ca. 12 hours) with a minority product of crystalline rutile (JCPDS # 01-073-1765). With increasing time, the anatase crystal size slightly increases from 4.3 ± 0.1 nm after 12 hours to 4.9 ± 0.15 nm after 48 hours reaction time. Rutile is present at short reaction times (via XRD, Figure 6b) and continues to grow at the expense of anatase with complete conversion occurring by 72 hours (via XRD, Figure 6b). Figure 6c and Figure 6d represent XRD patterns of TiO_2 synthesized at pH 10 and 11, respectively where the only observed phase was crystalline anatase, irrespective of reaction times (ca. 1 – 168 hours). Crystallites for both reaction conditions (pH 10 and 11) increase in size with increasing time. The anatase crystallites increase in size with increasing time from 3.06 ± 0.26 nm after 1 hour to 8.22 ± 0.23 nm after 168 hours (pH 10, 150°C). The resulting anatase crystallites at pH 11 are smaller than those at pH 10 (ca. 2.81 ± 0.02 nm after 1 hour to 6.20 ± 0.05 nm after 168 hours).

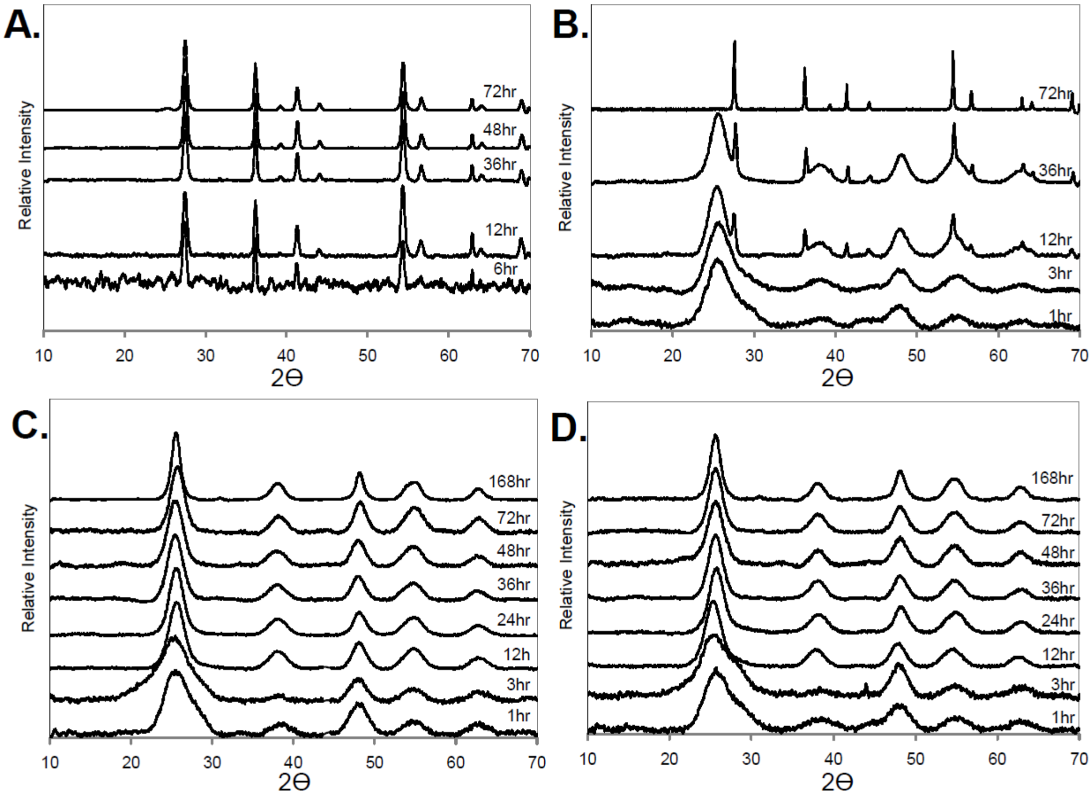

Figure 6. X-ray diffraction of TiO_2 nanocrystals formed at 150°C and A) pH 7.8, B) pH 9, C) pH 10, D) pH 11 versus time.

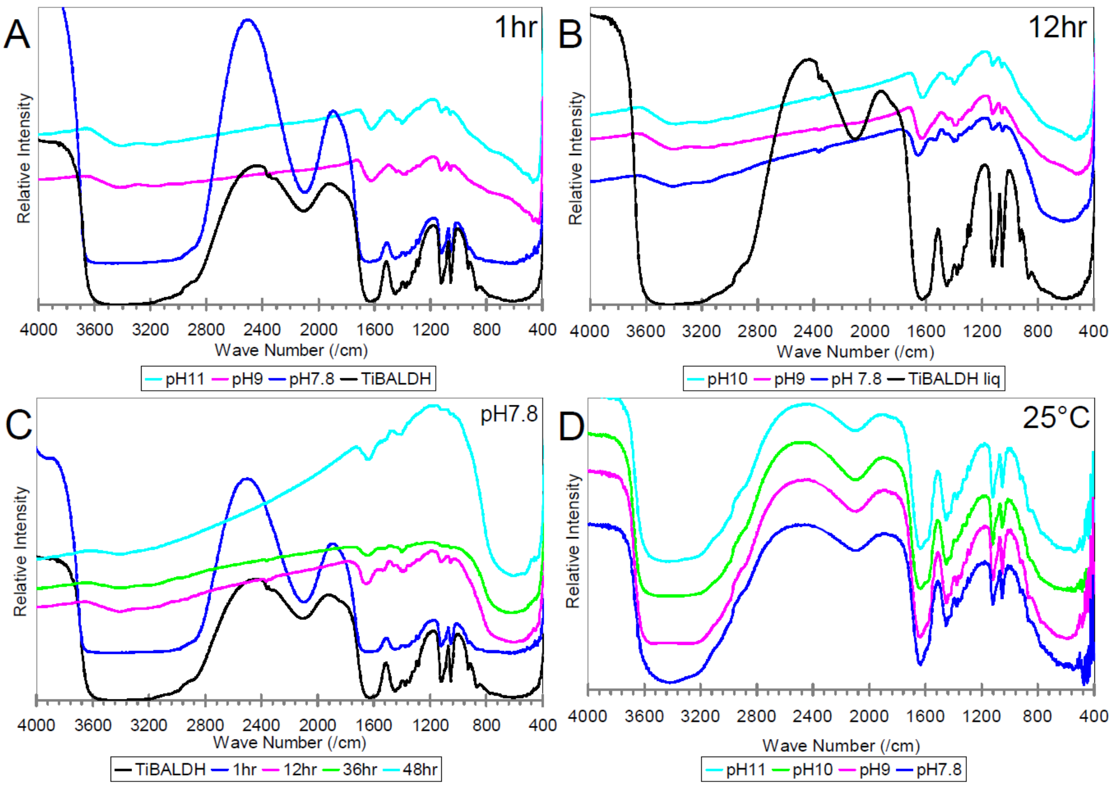

Figure 7. FTIR spectra of TiO_2 nanocrystals formed at 150°C for A) 1 hour at different pH conditions and B) 12 hours at different pH conditions; C) at pH 7.8 as a function of increasing time, and D) pH adjusted precursor prior to heat treatment (liquid FTIR samples).

FTIR was used to investigate the hydrolytic stability of TiBALDH and its subsequent reaction products. Figure 7 illustrates the resulting FTIR spectra of TiO_2 synthesized at different pHs for 1 hour, and 12 hours. Spectral peaks were identified based on appropriate references [80, 117-123]. The broad adsorption peak observed near 3500 cm^{-1} is due to the presence of hydroxyl groups, while peaks at 2980, 2925, and 2870 cm^{-1} are associated with the C–H stretching vibration from the lactato ligands of TiBALDH.

The two peaks at 1615 and 1572 cm^{-1} are the asymmetric and the symmetric stretching adsorptions from the carboxylic functional group on the lactato ligand. A peak at 1600 cm^{-1}, not attributed to TiBALDH, appears in products synthesized after 1 hour at both pH 9 and 11, and is associated with the bending of water adsorbed on the surface of TiO_2 crystallites [120]. Several peaks between 1280 – 1440 cm^{-1} are due to C–H symmetric and asymmetric stretching with the exception of a sharp band observed at 1392 cm^{-1} (N–H stretching from residual ammonia). The two peaks at 1117 and 1053 cm^{-1} are from the C–CH_3 and C–O stretching, respectfully. After 1 hour at pH 7.8, (Figure 7a), the product has a similar FTIR spectrum as the precursor, demonstrating the hydrolytic stability of the lactato ligands on the TiBALDH precursor.

2.4.2 **Phase Development.**

The fundamental structure of all three crystal phases of TiO_2 consist of TiO_6 octahedra with different spatial arrangements [53, 77]. Figure 8 depicts the octahedral arrangements of rutile and anatase. Rutile is composed of primarily corner-sharing octahedra with each octahedron surrounded by ten octahedra, two that are edge-shared, and eight that are corner shared[53, 124]. The TiO_6 octahedra in anatase are surrounded by eight octahedra (four edge shared and four corner shared) [124-126]. Thus, the fraction of edge-sharing octahedra needed to form anatase is much greater than that of rutile (50% vs. 20%, respectively). In order for an edge-sharing bond to form between two octahedra, two juxtaposed hydrolysis, and condensation reactions must occur. Corner-sharing octahedra require just one hydrolysis and condensation reaction in the coordination sphere. The Ti cation in the TiBALDH complex is octahedrally coordinated, containing two, bi-dentate lactato ligands in the x-y plane and two hydroxyls along the z-axis (Figure 9a).

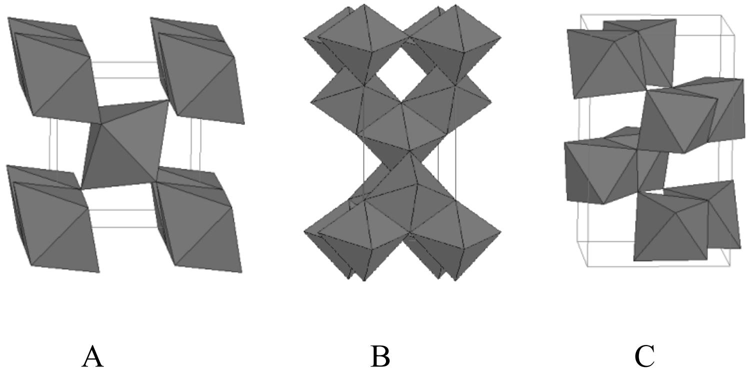

Figure 8. Illustrations of the TiO_6 octahedral arrangements in a) rutile, b), anatase, and c) brookite.

In the hydrothermal synthesis reactions using the TiBALDH precursor, differing phase behavior was observed as a function of pH (Figure 6). Understanding the similarities between the fundamental structural unit (i.e., octahedral arrangement) and the molecular structure of the precursor provides insight into the nucleation and growth behavior observed with respect to pH (illustrated in Figure 9). At near neutral pH conditions, the bidentate organic ligands bound to Ti are relatively hydrolytically stable (as demonstrated in FTIR spectra shown in Figure 7) due to the low concentration of hydroxide ions [107]. In addition, the chelation effect of these bidentate ligands affords more hydrolytically stable complexes compared to monodenate ligands [114]. The carboxylic functional group allows for a conjugate system, which reduces the Lewis basicity of the bonding oxygens reducing the charge donation to the metal center [114].

Another reason for the stability of the lactato ligand on TiBALDH at near neutral pH (stored in water) is likely due to its 5-member ring, which reduces strain within the ring, while not being sterically crowding around the metal center [114]. Rutile is thus the predominant phase observed at pH 7.8 (as illustrated in Figure 6) due to the hydrolytic stability of the stable lactato ligands and condensation occurring primarily through the two existing hydroxyls along the z-axis, allowing corner-shared bonds.

Under more basic conditions, anatase is the sole product observed even after extended durations (as shown in Figure 6d). The hydroxide ion must cleave the organic from the Ti complex by nucleophilic addition to either the Ti cation or to the lactato group (Figure 9c), forming an ammonium lactate byproduct [115]. Raising the pH increases the rate at which the sterically hindering organic ligands are cleaved from the Ti complex, thereby enabling hydrolysis and condensation through edge sharing bonds, dominant in anatase [69, 77]. Other hydrolytically stable ligands with conjugate systems have been observed such as Ti-ACAC [107]. Bidentate ligands have been shown previously to preferentially form anatase or rutile at different pH conditions and reaction temperatures [127, 128]. Kobayashi et al. demonstrated that two ligands with very similar structures resulted in either anatase or rutile at slightly different pH conditions based on varied degrees of hydrolysis [127]. Based on the hydrolytic stability of the TiBALDH complex in aqueous solutions discussed above, it is clear that the lactato ligand affords stability to the complex within the X-Y plane long enough for condensation to initiate condensation along the z-axes.

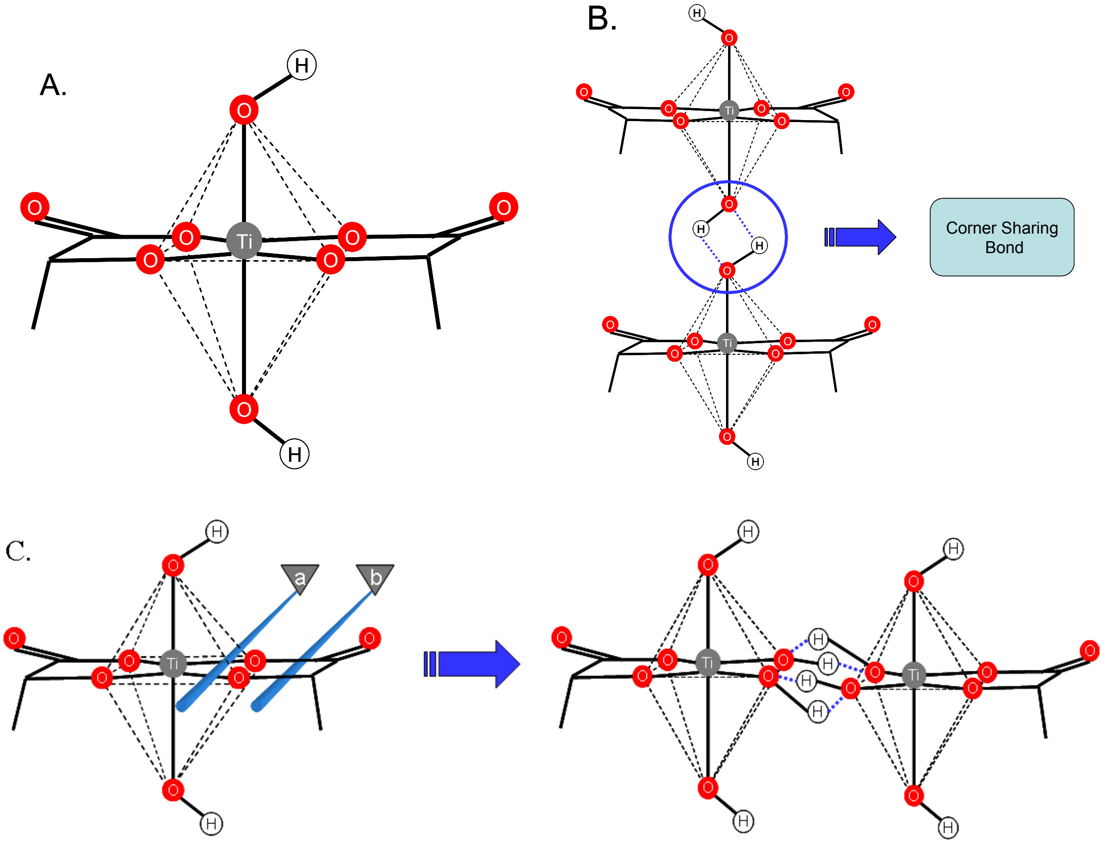

Figure 9. A) Structure of TiBALDH with dashed lines demonstrating its octahedral structure. B) Illustration of TiBALDH precursor with hydrolytically stable lactato ligands, forcing condensation along the z-axis. C) Illustration of TiBALDH cleavage by nucleophilic attack by the OH- at the a) Ti metal center and at b) bi-dentate ligands (shown by blue dotted lines) which allows for two condensation reactions in the x-y plane of the coordination sphere to occur simultaneously, yielding edge-sharing bonds.

At an intermediate pH relative to the previous conditions described (ca. pH 9), mixed phases of rutile and anatase were observed. This illustrates that nucleophilic cleavage of the organic ligands and condensation reactions of the two hydroxyls along the z-axis of the precursor are competing reactions. At pH 9, the rate of cleavage of the lactato group is slower than that at pH 10 or 11, enabling formation of corner sharing bonds and yielding minor quantities of rutile. By increasing the OH^- concentration at pH 10, the rate of hydrolysis of TiBALDH should be greater than that at pH 9, leading to condensation along x-y planes, and to the formation of anatase as seen. Additional increases in pH also greatly increases the rate of nucleation as observed by rapid formation of product and the decreased crystallite size (ca. 2.81 ± 0.02 nm after 1 hour at pH = 11 vs. 3.06± 0.26 nm after 1 hour at pH = 10). The decreased crystallite size is most likely due to the large number of nuclei formed at higher pH, thus reducing the concentration of titanium species available for the growth of the resulting crystallites.

The FTIR spectra show a slight decrease in the asymmetric stretching (ca. 1600 cm^{-1}) of the carboxylic group with an increase in pH, indicating a weakening of the bidentate bond (Figure 7d). After 1 hour at pH = 10, the doublet peak (1615 and 1572 cm^{-1}) associated with the complexed lactato ligand of the TiBALDH precursor disappears, indicating cleavage of the lactato ligand. This cleavage enables the formation of edge-sharing bonds between TiO_6 octahedra via condensation between juxtaposed hydroxyl ligands. At pH 7.8, this reaction is kinetically limited due to the hydrolytic stability of the lactato ligands and therefore limiting the formation of anatase. Table 2 and Table 3 demonstrate the changing frequencies of the asymmetric and symmetric stretching of the carboxylic groups, which can be used to indicate the bond strength and complexation state of the bonds (e.g., mono- or bi-dentate) [118, 122]. Although there is no evidence of rutile nucleation for reaction times less than 1 hour, FTIR (Table 2) suggests that the hydrolytic stability of the ligands on the precursor may restrict the formation of anatase subcritical nuclei and allow the formation of the rutile subcritical nuclei. After 12 hours, the change in frequency between the asymmetric and symmetric stretches is greater than 100 cm^{-1}, indicating a substantial change in the complexation of the lactato ligand with the Ti cation. This is an indicator of the modification from a bidentate to a monodentate complexation [118, 122].

Table 2. Frequencies of the $\nu(OCO)_{asym}$ and $\nu(OCO)_{sym}$ for 25°C reaction with increasing pH (liquid FTIR samples).

Reaction pH	$\nu(OCO)_{asym}$	$\nu(OCO)_{sym}$	$\Delta\nu$
8	1620	1587	33
9	1634	1575	59
10	1636	1575	61
11	1636	1575	61

Table 3. Frequencies of the $\nu(OCO)_{asym}$ and $\nu(OCO)_{sym}$ for pH 7.8 reaction with increasing time.

Reaction Time (hr)	$\nu(OCO)_{asym}$	$\nu(OCO)_{sym}$	$\Delta\nu$
0	1620	1587	33
1	1630	1564	66
12	1641	1519	122
36	1633	1512	121
48	1626	1506	120

Small rutile nuclei (< 14 nm) are not thermodynamically stable compared to the anatase nuclei[77, 129]. The presence of small (< 14 nm) anatase crystallites at pH 9 with rutile crystallites at short reaction times (ca. ~1 hour) suggest that the rutile nucleates directly from the precursor (independently from anatase) resulting in a mixed phase product (Figure 6b). If single anatase crystallites were transforming to rutile, the particles would be significantly larger than the 4 – 5 nm crystals observed by TEM. As the pH is raised above 9, average the anatase crystallite size increases, but does not transform to rutile. The resulting phase of the TiO_2 product is ultimately dependent on the hydrolysis rate of the precursor, which is controlled by the reaction pH.

2.4.3 Growth Mechanism.

The driving force for crystal growth is the reduction in surface energy with specific morphological features resulting from the reduction in high energy surfaces [130, 131]. Classical crystal growth has been described by Ostwald ripening (OR), where large crystals grow via ion by ion addition at the expense of small crystals that dissolve into solution[130-132]. Oriented Attachment (OA) is a non-classical mechanism of crystal growth [130, 131], where the joining of solid crystals occurs at crystallographically specific locations and is typically observed in materials with low solubility. OR characteristically results in the characteristic equilibrium morphology of the crystal [105, 131, 133] where OA may result in irregular morphologies due to twists, tilts, and shifts at attachment planes [130, 131]. Another growth mechanism that results in dislocations and tilts is Repeated Nucleation where heterogeneous nucleation occurs on pre-existing crystallites in the system [134, 135]. Repeated Nucleation appears similar to OA due to the irregular morphologies, but is not observed here.

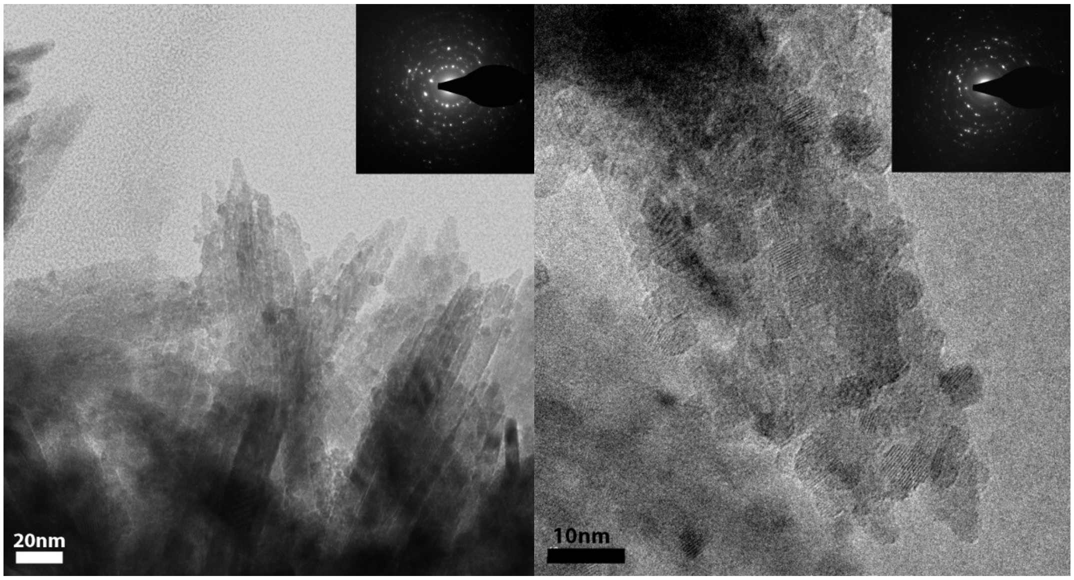

Figure 10. Bright field TEM images of TiO_2 synthesized at pH 7.8 / 150°C. Selected area diffraction patterns inserted for phase identification.

Under the near-neutral synthesis condition, OA appears to be the main mechanism of growth for the rutile rods as observed via bright field TEM due to the observed alignment of aggregated crystallites (Figure 10) [130, 131, 134]. The solubility of TiO_2 under this reaction condition (ca. pH $\approx$ 7.8, 150°C) is relatively low ($K_{sp} \approx 1.6 \times 10^{-23}$) compared to significantly greater solubility levels at higher pH conditions (e.g., pH 10, 150°C, $K_{sp} \approx 4.0 \times 10^{-18}$) [136]. The lower solubility of TiO_2 at this condition reduces the dissolution of crystallites, thereby minimizing the amount of titanium ions available for growth by ion-by-ion addition (OR) thus, favoring growth by OA [130-132]. Figure 10 shows TEM images of the samples prepared at pH 7.8 and 150°C that have aggregated rod-like rutile crystallites. The individual rod-like crystals appear to be composed of smaller, primary particles that have subsequently been reoriented and fused into the rods. Consistent with OA, the rod-like crystals show (Figure 10) discontinuous segments and twists within one crystal from misalignment of the attaching crystals [131, 137]. Concurrently, the crystallite size determined from the Sherrer equation is much smaller than the rod-like crystals observed in TEM, indicating the rod-like crystals are secondary crystals that have slight discontinuities between the primary crystals measured via XRD. With increasing reaction time, the small primary particles eventually coarsen to form larger, more cohesive crystals with fewer visible defects, which is in agreement with the XRD peak narrowing (Figure 6c).

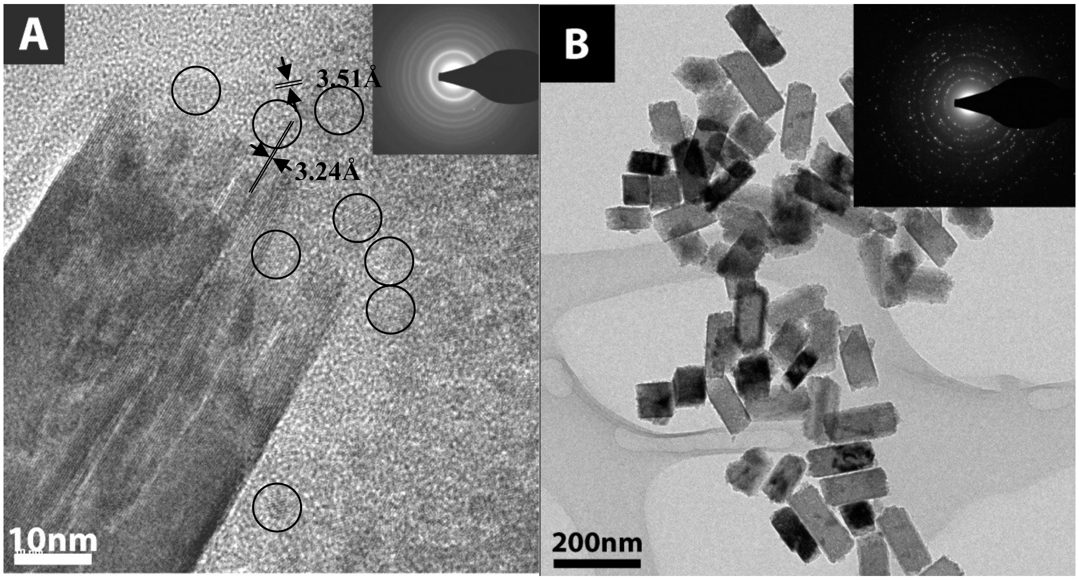

Figure 11. Bright field TEM images of rutile and anatase (circled) TiO2 crystals synthesized at pH 9 at 150°C for a) 12 hours and b) 72 hours. Selected area diffraction patterns and d-spacing

measurements (3.51Å: (101) planes of anatase; 3.24Å: (110) places of rutile) inserted for phase identification.

Growth of TiO_2 at pH 9 appears to occur via OA of anatase crystallites (demonstrated in Figure 11) that upon attachment, will eventually undergo a phase transformation to rutile. The TEM images reveal large rod-like rutile crystals which appear to be less aggregated, suggesting a slightly higher solubility at this condition, agreeing with theoretical calculations performed by K. G. Knauss et al. [136]. Crystallite sizes calculated via the Sherrer equation from XRD patterns confirmed the coarsening among the secondary crystals (rod-like rutile crystals). However, OA seems to be the predominant mechanism since the anatase crystallites do not increase in size while the rutile crystallites increase in size (as observed by XRD and TEM). Consequently, the concentration of the anatase phase decreases while the rutile concentration increases. The irregular shape of the rutile crystals, specifically at the ends of the rods (seen in Figure 11a), demonstrates growth via OA. Anatase crystallites aggregate with each other and rutile (with preferred orientation) and are subsequently transformed to rutile, driven by the reduction of free energy of the system [130, 132].

At the reaction conditions of pH > 10, our observations indicate Ostwald ripening is the predominant growth mechanism. The theoretical solubility of TiO_2 at pH 10 is approximately an order of magnitude larger than at pH 8 and 2 orders of magnitude larger at pH 11 [136]. These highly soluble conditions favor the OR mechanism [130, 131]. TEM images shown in Figure 12 demonstrate the presence of larger anatase crystals of equilibrium morphology surrounded by smaller crystals. Figure 12 also illustrates the broad size distribution with increasing reaction time, consistent with OR [133]. There is no evidence of OA under these synthesis conditions.

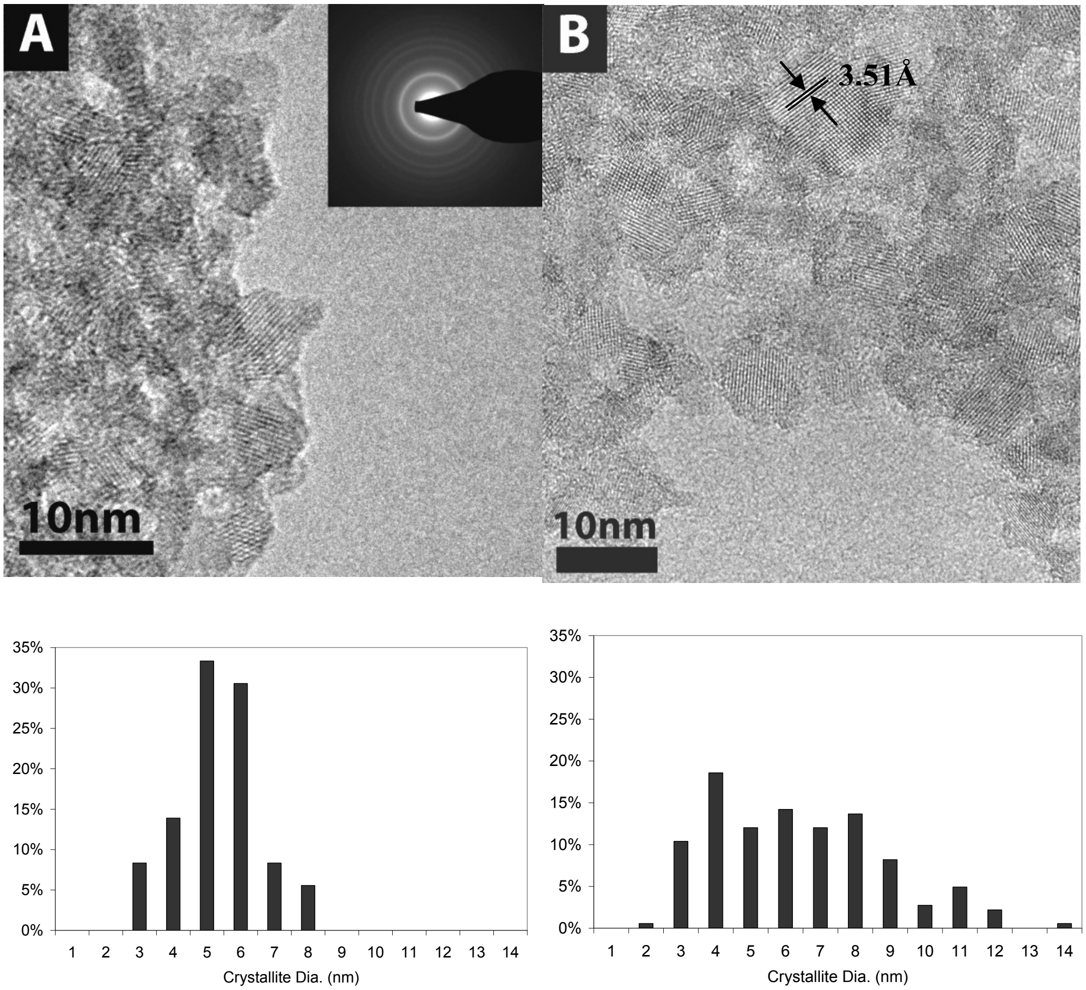

Figure 12. Bright field TEM images of Anatase TiO_2 crystals synthesized at pH 11 / 150°C for a) 12 hours and B) 72 hours with subsequent crystallite size distributions.

2.5 Conclusions

In this work, we studied the phase development and growth mechanisms of TiO_2 from the organometallic precursor TiBALDH as a function of pH and reaction time. The molecular structure of the precursor and the pH of the reaction solution greatly influences the nucleating phase of TiO_2. At near-neutral pH, the lactato ligands bound to the titanium cation in the x-y plane of the coordination sphere of the precursor, TiBALDH, are stable. Thus, condensation primarily occurs via existing hydroxyls in the z-direction, thus yielding corner-shared octahedra, the primary structural motif in rutile. At higher pH conditions, the greater hydroxide ion concentration promotes hydrolysis of the TiBALDH, enabling condensation between the edges of TiO_6 octahedra, yielding anatase. The pH of the reaction solution also influences the growth mechanisms. Oriented attachment was observed to be the dominant growth mechanism for TiO_2 (rutile-phase) during reactions at near neutral pH conditions (due to the low solubility of crystallites at ca. pH 8 and 9). The rutile crystals appear to be composed of primary particles that reoriented and fused together forming larger secondary particles. Ostwald Ripening was observed to be the dominant growth mechanism of the anatase-phase TiO_2 crystallites for reactions at higher pH conditions (due to higher TiO_2 solubility at ca. pH > 10). The anatase crystallites gradually increase in diameter with increasing reaction time, however the crystallite diameter distribution also broadens with time, indicative of Ostwald Ripening. Thus, control of the phase development in TiO2 has been demonstrated, which is critical for improving performance in photocatalytic and photovoltaic applications.

Chapter 3.

Synergistic Effect of pH and Phase in a Nanocrystalline Titania Photocatalyst

To be submitted to *Applied Materials & Interfaces*. Unpublished Work Copyright (2013) ACS.

Kinsinger, N. M.; Dudchenko, A.; Wong, A.; Kisailus, D., Synergistic Effect of pH and Phase in a Nanocrystalline Titania Photocatalyst. Applied Materials & Interfaces 2013, *in review*

Abstract

Titanium dioxide is a semiconducting material that has been studied for many years a as a photocatalytic material to degrade organics in water. This study investigated the effect of anatase-rutile mixtures and pH on the photocatalytic degradation of the dye Methylene blue as the target analyte. Anatase-rutile mixtures between 0 and 90% rutile that were synthesized from a water soluble precursor were suspended at pH4, 7, and 10. Suspension pH significantly affected the reactivity and efficiency of the photocatalysts due to the particle-particle and sorbate-surface interactions. The highest removal percentage of MB by 240 minutes at pH = 4, 7, and 10 was 35%, 99%, and 93%, respectively. pH7 was ideal to observe the affect of percent rutile on the degradation rate where 91% was removed within 120 minutes by the material composed of 20% rutile, which is attributed to the synergistic charge transfer of holes from rutile to anatase.

3.1 Introduction.

The rapid increase of production of industrial chemicals and pharmaceuticals and their discharge into the wastewater system presents multiple issues such as interference with hormone regulatory systems and reproductive damage to humans and wildlife [103, 138]. The occurrences of emerging contaminants now being detected, along with the advancement in measurement technologies, are causing increased concern for public health and safety [1]. Pharmaceuticals and personal care products (PPCPs), surfactants, and various industrial chemicals are known to be endocrine disrupting compounds (EDCs). Wastewater treatment facilities designed to remove suspended solids and oxygen demanding compounds are not properly suited to degrade such organics [1, 5, 19, 23, 24]. Many of these of compounds are persistent following wastewater, environmental, and drinking water treatment processes and thus have been observed in potable-water supplies [19]. Several hydrophobic compounds have been observed to be persistent after activated carbon filtration[19].

The use of wastewater effluents to augment water supplies in areas of water scarcity increases the likelihood of such contaminants (pharmaceuticals) occurring in drinking water [5, 19]. One of the most challenging aspects of such water reuse is the inability to detect the presence of the large number of compounds that may be present from consumer and household, industrial, and agricultural sources [5, 19]. These compounds are typically low in concentration (<1μg/L), below the minimum testing concentration currently set by the Food and Drug Administration (FDA) [1, 5, 19]. Even though this concentration is far below therapeutic doses, little is known about the long-term chronic exposure to a cocktail of organic compounds, which may include PPCPs and compounds not designed for human consumption such as flame retardants, solvents, dyes, and fuels [5, 19]. Alarmingly, one study detected a combination of 11-17 different organics in finished water from a drinking water treatment facility [19].

To accommodate the ever-increasing demand for clean drinkable water and the rapid increase in the use of personal care products and pharmaceuticals (PCPPs), new treatment methods other than the traditional processes must be implemented to remove these hazardous compounds and degrade them to non-harmful constituents. Degradation of organic compounds via oxidation by photocatalytically induced hydroxyl radicals (OH•) is a potential treatment technology that can degrade a wide range of organic compounds to complete mineralization with no selectivity [6, 28, 42-44, 47, 54, 59]. Over 800 compounds have been catalogued by the Environmental Protection Agency that are completely mineralized by this mechanism which eliminates the concern of secondary byproducts when using other oxidation agents such as chlorine.[42].

Titanium dioxide (TiO_2) is of significant interest due to its semiconducting properties that enable its use as a heterogeneous photocatalytic material, rapidly and completely mineralizing organic compounds in water when exposed to UV irradiation without harmful byproducts [43, 47]. If light with energy greater than the band gap of TiO_2 is absorbed, electron-hole pairs are generated. The charge vacancy (hole, h^+) left in the valence band by the excited electron oxidizes adsorbed water producing hydroxyl radicals [43, 52-55]. Operating parameters such as pH have been reported to greatly affect heterogeneous photocatalytic performance due to particle aggregation, which will reduce accessible surface active sites and block excitation events within the catalyst [139]. The pH also affects the ionization state of catalyst surface and the organic compounds, which has been shown to affect the sorbate-surface interactions that impact performance due to scavenging of OH• radicals [21, 140-145].

TiO_2 has three crystalline phases: anatase, rutile, and brookite. Anatase and rutile are the two photocatalytically relevant phases with bandgaps of 3.2 and 3.0 eV, respectively [46, 70, 71]. Anatase, a metastable phase, has been shown to be more photocatalytically active than the thermodynamically stable rutile phase, which is the stronger photoabsorber. Mixed phase TiO_2 (i.e., anatase and rutile), such as Degussa P25 (an industrially produced photocatalyst), has been shown to be more effective than either pure anatase or rutile phase TiO_2 [45, 70, 71]. The improved performance of this mixed phase photocatalyst is attributed to a synergistic charge transfer across the anatase-rutile interface [70, 71, 146]. Although the mechanism of electron transfer between the different phases (anatase and rutile) is not clearly understood, it is evident that the presence of both phases greatly improves the photocatalytic activity [71]. However, the proportions of these phases required for optimum photocatalytic activity is debatable due to the differences in synthesis processes, crystallite sizes, and interactions between phases. These studies typically do not include address the impact of particle-particle and sorbate-surface interactions that depend on the pH at which photocatalytic reactions are performed.

Recently, we have reported the synthesis of TiO_2 using a water soluble and stable precursor that yields high surface area and phase controlled nanoparticles [84]. Here, we investigate the effect of TiO_2 phase as well as suspension conditions that enhance the photocatalytic degradation of methylene blue (MB), a common analyte used in determining photocatalytic reaction rates.

3.2 Experimental.

3.2.1 Preparation of materials.

TiO_2 photocatalytic materials were synthesized under hydrothermal conditions. Briefly, 1M Titanium bis(ammonium lactato) dihydroxide (TiBALDH, Sigma Aldrich) solutions were prepared by diluting with de-ionized (DI) water. After dilution, ammonium hydroxide (30 wt %, Acros Organics) was used to adjust the solution pH to ~ 9. The solutions were placed in Teflon-lined steel reactors (Parr Instruments, Moline, IL) at 150°C for different durations (1 - 72 hours). The resulting products were centrifuged, washed with DI water, sonicated (Branson 2510) for 30 minutes between washes (to remove any unreacted precursor and reaction by-products) and subsequently dried in air at 100°C for 24 hours [84].

3.2.2 Material Characterization.

TiO_2 powders were characterized using X-ray diffraction (XRD), Transmission Electron Microscopy (TEM), Surface area analysis via the Brunauer, Emmett, and Teller (BET) method, and Zeta Potential measurements. The resulting phases were determined by X-ray Diffraction (XRD) analysis (Philips X'Pert) using Cu Kα radiation. Crystallite diameters of anatase and rutile crystals were calculated based on the (200) and (210) reflections, respectively, using the Scherer formula (equation 2):

$$D_{(hkl)} = \frac{\kappa\lambda}{\beta\cos\theta} \tag{2}$$

where κ is the shape factor, λ the wavelength of the Cu Kα radiation, β the full width at half maximum (FWHM) of the (h k l) peak, and θ is the diffraction angle. The relative composition of crystalline rutile was determined via the following equation (equation 3):

$$x_r = \frac{I_R}{I_R + 0.884 I_A} \tag{3}$$

where, I_A and I_R are the integrated intensities of anatase (101) and rutile (110) peaks, respectively [69]. In order to corroborate these results, specimens were observed using both bright field imaging and electron diffraction analyses in TEM (T-12, T-20, and Titan, FEI). TiO_2 nanocrystals were dispersed in ethanol, sonicated (Branson 2510) for 30 minutes, and subsequently deposited onto ultrathin carbon films on holey carbon supports with a 400 mesh copper grid (Ted Pella).

The surface areas of powders were determined via BET nitrogen adsorption at 77K using a Micromeritics Tristar 3000. Prior to analysis, samples (~ 100mg) were degassed at 90°C for 6 hours under vacuum. The adsorption isotherms of nitrogen at 77K were obtained using fifteen relative pressure values ranging from 0.05 to 0.35.

Zeta potential analysis was used to characterize the surface charge and isoelectric point (IEP) of the as-synthesized materials. Suspensions (500mg/L) of TiO_2 nanomaterials (UV pretreated for 24 hours prior to characterization) were prepared incrementally from pH = 3 to pH = 10 by the addition of hydrochloric acid and ammonium hydroxide in a 0.01M sodium chloride solution. The zeta potential was measured using ZetaPALS analyzer (Brookhaven Instruments Corp. Holtsville, NY).

3.2.3 Photocatalytic Performance.

The effects of suspension pH and anatase-rutile ratios on photocatalytic activity were determined by measuring the degradation of Methylene Blue (MB) in the presence of TiO_2 nanoparticle suspensions under UV illumination. Prior to degradation testing, TiO_2 suspensions were prepared by dispersing the TiO_2 powders in filtered deionized water (0.22μm, Millipore), adjusting the pH to either 4, 7, or 10 with hydrochloric acid or ammonium hydroxide, respectively, and sonicating for 5 minutes using a tip-horn ultrasonic processor (Hielscher UP100H, Ringwood, NJ). Any residual organics remaining on the surface of the TiO_2 photocatalytic material (i.e., from the synthesis process) were removed by irradiating the material for 24 hours prior to testing with UV light (Phillips UV (A) 40 Watt bulb at $1mW/cm^2$). Fourier Transform Infrared Spectroscopy (FTIR) was used to confirm the absence of residual organic (data not shown).

In a typical degradation reaction, a glass reactor was filled with 100mL containing (i) a 500mg/L TiO_2 suspension and (ii) 13μM solution of Methylene Blue (MB) maintained at 25°C and magnetically stirred at 500 rpm. The photon source was a Phillips UV (A) 40 Watt bulb operated at $1mW/cm^2$. At the start of each degradation experiment, MB (under dark conditions) was allowed to absorb onto the suspended TiO_2 for one hour prior to irradiation, followed by direct irradiation with the photon source. The photocatalytic activity was monitored by measuring the absorbance of MB via UV-Visible Spectroscopy (Beckman Coulter DU 800 Spectrophotometer) between 200 – 800nm (λ_{max}=668nm).

Reaction rates were determined by fitting the MB degradation over time with pseudo-first order equation:

$$C_t = C_o e^{-kt} \tag{4}$$

where, C_t is the concentration of MB in solution at time t, C_o is the initial concentration of MB in solution, and k is the pseudo-first order rate constant.

3.3 Results and Discussion.

3.3.1 Material Characterization.

To investigate the effects of phase on the photocatalytic degradation, mixed phase TiO_2 samples were prepared by adjusting the hydrothermal reaction parameters (primarily time) [84]. The relative phase composition (i.e., rutile and anatase) for products at each duration were determined using equation 3 and are depicted in Figure 13. At short reaction times (i.e., 1 hour), nanosized (3.1 ± 0.1 nm) anatase (JCPDS # 01-084-1286) is the primary phase observed (Figure 13a). Larger rutile (JCPDS #01-073-1765) crystals (14.4 ± 4.1nm) are clearly present (via XRD measurements) after 12 hours and continue to grow at the expense of the anatase crystals via oriented attachment [84]. The anatase crystallite size increases slightly from 3.1 ± 0.1 nm (1 hour) to 5.1 ± 0.2 nm after 72 hours. Complete transformation to rutile occurs by 72 hours with significantly larger rutile crystallites formed (32.1 ± 6.9 nm). TEM analysis of the resulting nanoparticles (Figure 13b) confirms the presence of the mixture of phases at different times. In addition, the crystallite sizes of anatase observed in TEM are consistent with XRD measurements. However, TEM micrographs reveal much larger (72 ± 11 nm diameter x 141 ± 27 nm long) rod-like rutile crystals that are coated with anatase crystallites. Discontinuous segments and twists within one rod-like rutile particle are observed in the TEM micrographs due to the attachment of the smaller anatase crystallites. Consistent with an oriented attachment growth mode, the larger secondary rutile particle is composed of primary particles (i.e., crystallites) that are assembled to form the rod-like particles that have slight discontinuities between these primary crystals, as confirmed via XRD [84, 131, 137].

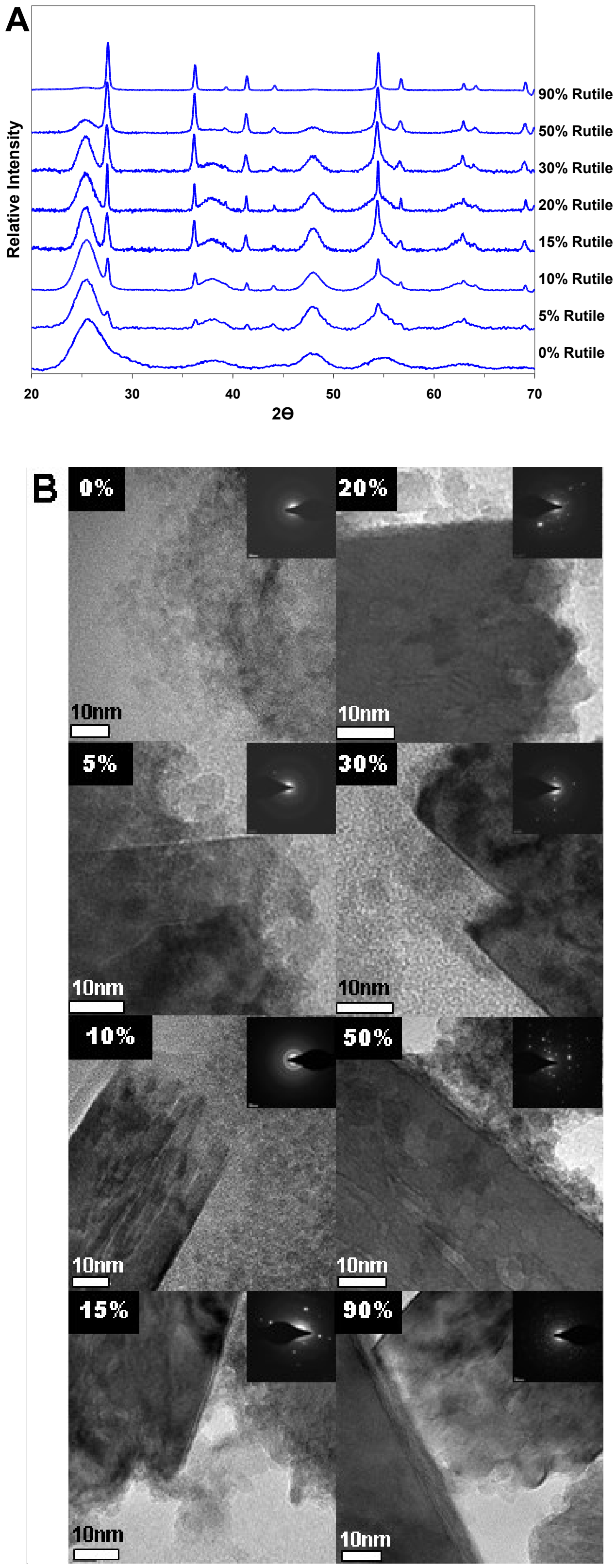
A
Relative Intensity
90% Rutile
50% Rutile
30% Rutile
20% Rutile
15% Rutile
10% Rutile
5% Rutile
0% Rutile
20
30
40
50
60
70
2Θ
B
0%
20%
5%
30%
10%
50%
15%
90%
10nm

Figure 13: A) X-Ray diffraction patterns and B) Bright field TEM micrographs (with selected area diffraction patterns inserted) of mixed phase TiO_2 (Anatase/Rutile) formed hydrothermally at pH = 9, 150ºC at different times.

BET surface area analyses (Table 4) of the mixed phase TiO_2 reveals a decrease in surface area with increasing rutile content, in agreement with the observation of the larger rutile crystals seen in Figure 13b.

Table 4: Surface area vs. Percentage of rutile.

Surface Area (m^2/g)	
0% Rutile	277.3 ± 2.8
5% Rutile	281.9 ± 9.84
10% Rutile	284.7 ± 4.60
15% Rutile	272.9 ± 1.36
20% Rutile	278.9 ± 1.60
30% Rutile	273.4 ± 7.83
50% Rutile	205.4 ± 1.7
90% Rutile	44.2 ± 1.1

The surface charge of colloids has a significant effect on their aggregation behavior [143]. In order to assess the effect of dispersion on the photocatalytic activity of TiO_2 suspensions, the pH was adjusted with subsequent investigation of colloidal behavior. TiO_2 suspensions prepared at different pHs were subjected to zeta potential measurements. The isoelectric points (IEPs) of our synthesized TiO_2 were observed (Figure 14) to be at lower pH values compared to other TiO_2 materials reported (~pH = 6) [143, 147-149]. The IEP of pure anatase TiO_2 was measured at pH = 4.5. However, with increasing concentration of rutile, the IEP shifts to higher pH values, with the IEP of a 90% rutile – 10% anatase TiO_2 measured at pH = 5.7. The shift in IEP is likely attributed to the increasing concentration of rutile crystals, which display (110) surfaces (as observed in TEM). These surfaces have been reported to have an IEP at pH = 5.5 [150]. In addition, the IEP shift may be related, in part, to the reduced acidity of the materials resulting from the reduced total surface area [143]. Anatase-rich samples suspended at pH = 4 are comprised of larger aggregates, a result of a relatively weak positive surface charge (i.e., ~ +10 mV for both 92% and 88% anatase-based samples). However, anatase-rich TiO_2 suspensions prepared at pH = 7 or 10 were significantly charged (i.e., > -20mV) and were thus well-dispersed due to strong interparticle electrostatic repulsion.

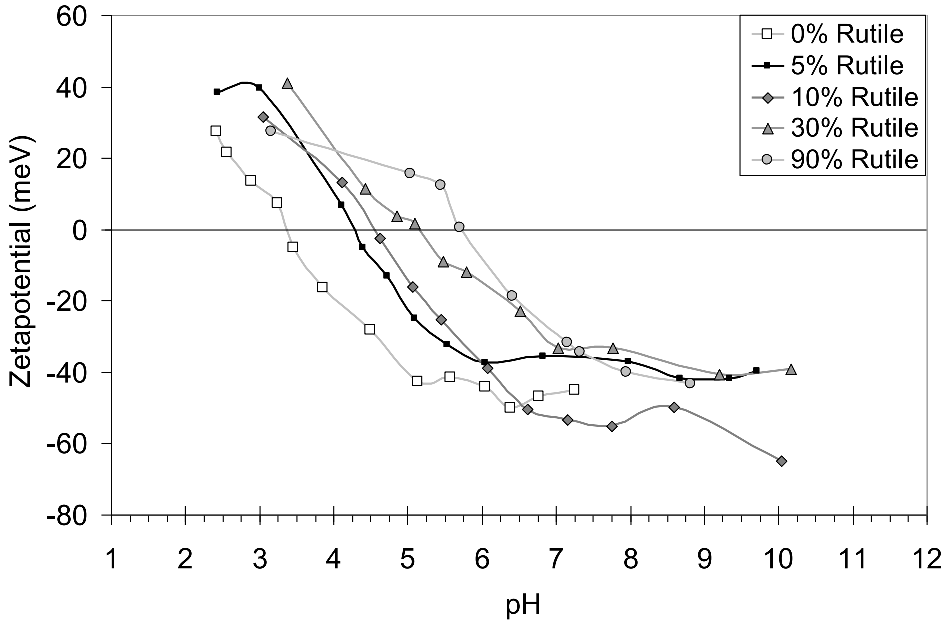

Figure 14: Zeta potential curves of the mixed phase TiO_2 nanoparticles with increasing relative rutile concentration, suspended in 0.01M NaCl solution.

TEM micrographs of particle suspensions prepared at pH = 4, 7 and 10 (Figure 15) were obtained to characterize their dispersivity. Large aggregates (ca. 300 nm) form at pH = 4 due to the weak interparticle forces. As expected, suspending these particles at pH = 7 leads to an increase in surface charge (> 20mV) with a subsequent reduction in aggregate size (ca. 130nm) and a further reduction (ca. 90nm) at pH = 10. This aggregation significantly reduces the accessible surface area while increasing the effective stokes radius, which leads to settling.

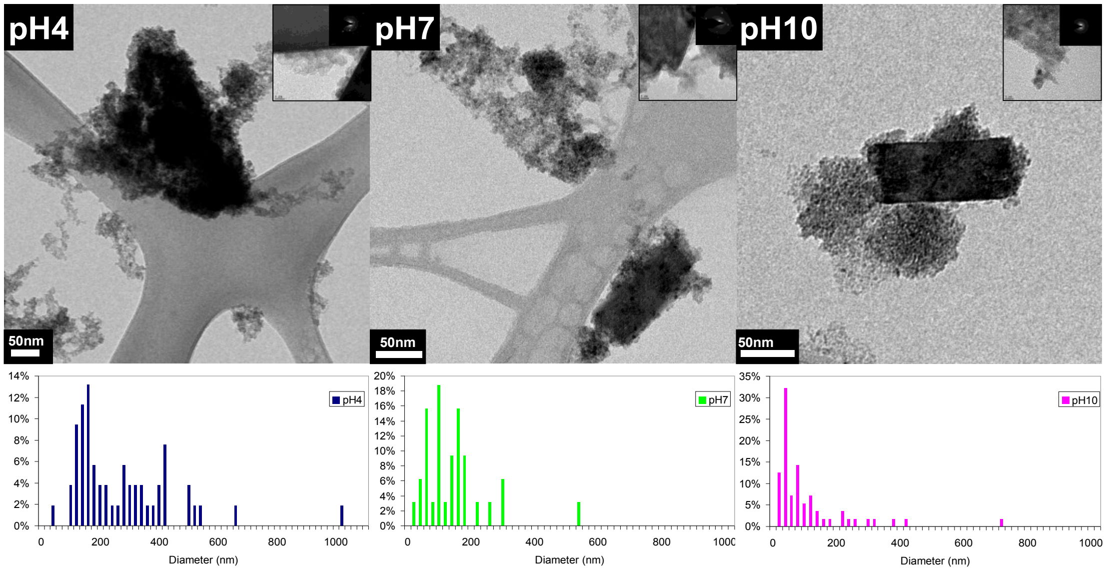

Average ~262nm **Average ~132nm** **Average ~90nm**

Figure 15: Bright field TEM micrographs of anatase TiO_2 particles synthesized at pH = 9, 150°C for 36 hours suspended at a) pH = 4, b) pH = 7, and c) pH = 10 with subsequent particle size distributions.

3.3.2 Kinetics of Photocatalytic Degradation: Effect of pH and Anatase-Rutile Ratio.

Methylene blue (MB), a compound used for therapeutic treatments of methemoglobinemia, ifosfamide-induced encephalopathy, and cyanide poisoning [151, 152] is also a commonly used analyte for photocatalytic degradation studies, and was subsequently chosen as the model pollutant to test the activity of synthesized photocatalytic materials [144, 153-155].

3.3.2.1 *Effect of suspension pH.*

Suspension pH had a dramatic effect on the reactivity and efficiency of the photocatalysts due to the particle-particle and sorbate-surface interactions. The highest removal percentage of MB by 240 minutes at pH = 4, 7, and 10 was 35%, 99%, and 93%, respectively, with 91% removed within 120 minutes by materials composed of 20% rutile suspended at pH = 7. When irradiated with UV (A) light in the absence of the TiO_2 catalyst, no obvious degradation of MB was observed; therefore direct photolysis was negligible at all experimental conditions considered.

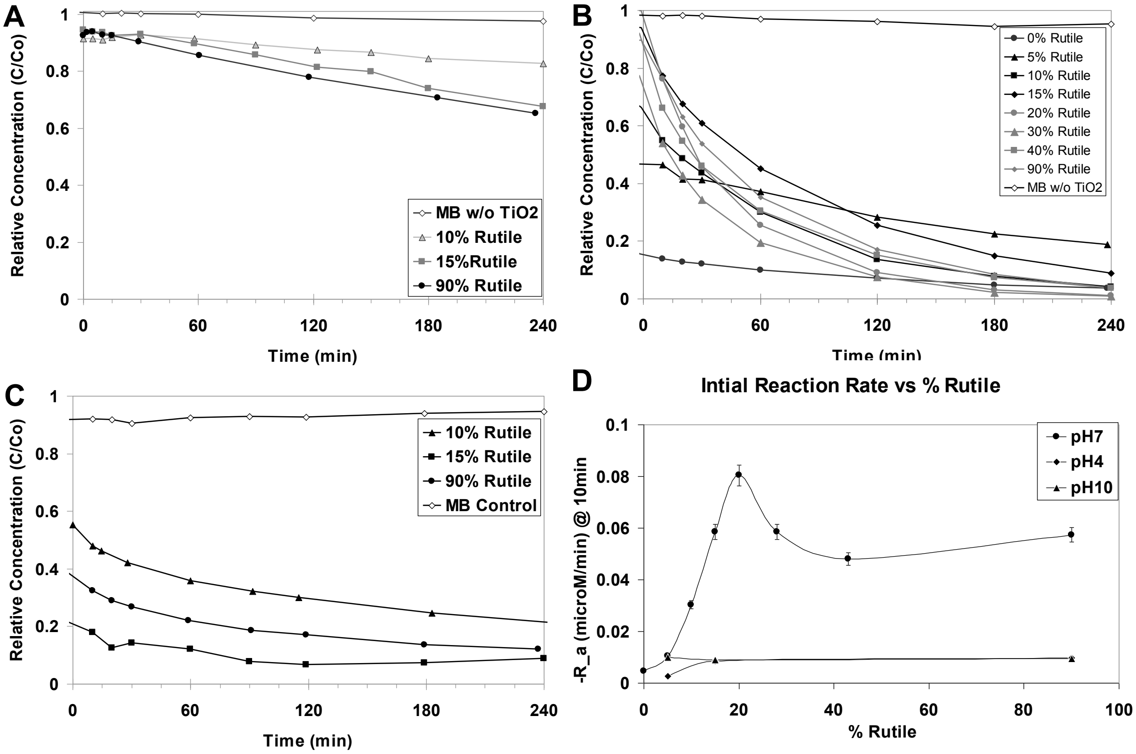

Figure 16: Photocatalytic degradation of MB versus time. Reactions were performed using TiO_2 suspensions (500mg/L TiO_2, $1mW/cm^2$ UV light intensity) at A) pH = 4, B) pH = 7, C) pH = 10. D) Initial degradation rate of MB versus % rutile in TiO_2 suspensions at pH = 4, 7, and 10 (lines drawn only as a guide).

pH is observed to be a major factor influencing both the rate and mode of degradation. The reduced efficiency observed at pH = 4 may, in part, be attributed to the increase in aggregation (vs. other pH conditions considered, Figure 15). Aggregation reduces the accessible surface available for analyte adsorption and photocatalytic reactions. In addition, large aggregates (diameter ~ 1 μm) lead to shadowing of internal crystals from incoming photons and will thus experience fewer excitation events, reducing photocatalytic activity [139]. Minimal dye adsorption on TiO_2 materials suspended at pH = 4 (Figure 16a) may also attribute to the reduced efficiency. MB is a cationic dye, which will be electrostatically repelled by the positive charge of the catalyst surface under acidic (i.e., TiO_2 at pH = 4) conditions [21, 142, 144, 145]. Thus, there is an increase in the diffusion time of the OH• from reduced sorbate-surface interactions and therefore increases the likelihood of the radical being scavenged.

Conversely, under more alkaline conditions, where the photocatalyst is negatively charged (Figure 14), adsorption of MB is favorable. However, absorption does not account for a signification proportion of removal at pH = 7 (Figure 16b), while at pH = 10 absorption is observed to be the major source of dye removal due to the increasing surface charge of the photocatalyst material [156]. Photocatalytic activity is enhanced due to proximity of dye to oxidation species, allowing for direct hole oxidation. Considerable absorption of MB on the catalyst surface obstructs the diffusion of electron scavengers such as dissolved oxygen to the surface. In fact, several layers of MB absorbed on the surface may block excitation of the photocatalytic reaction, thus hindering photocatalytic activity as seen in Figure 16 [140, 141].

3.3.2.2 *Effect of Anatase-Rutile Ratio.*

The degradation efficiency of the mixed phase TiO_2 suspensions was observed to be pH dependent. The observed reaction rate (at 10 minutes) versus percent rutile at all three pH conditions (i.e., pH = 4, 7, 10) are illustrated in Figure 16d. Degradation rates of materials suspended at pH = 4 improve with increasing rutile content. However, these reaction rates are still lower than those at pH 7, with 20% rutile achieving the highest removal rates. At pH = 4, increasing the rutile content produces a more stable suspension due to increased surface charge (>20meV). The result is a less aggregated suspension, which reduces the shadowing effect [139]. As discussed previously, the highest degradation rate was observed at pH = 7 with a 20% rutile / 80% anatase phase mixture of TiO_2, which is consistent with previous studies [157]. This is indicative of a synergistic effect between anatase and rutile interfaces, where contact is necessary, rather than a combination of the individual photocatalytic properties [146].

Several studies have reported enhanced photocatalytic performance with anatase-rutile mixtures due to a perceived synergistic mechanism between the anatase and rutile crystals [71, 157-159]. Once anatase and rutile crystals are in contact, electrons will transfer from anatase (higher Fermi level) to the rutile (lower Fermi level) until the Fermi levels in each crystal are equal [45, 160, 161]. Once equilibrium is reached, a space-charge region is formed due to the accumulation of electrons on the rutile crystals and a depletion region on the anatase crystals. This results in an upward band-bending in anatase and a downward band-bending in rutile (illustrated in Figure 17a). The presence of a space-charge layer at the surface of the particles will move the charge carriers in opposite directions and will favor the transfer of holes from anatase to rutile. The space-charge layer effectively reduces electron-hole recombination [45, 158, 160, 161]. Due to the relatively small energy difference, it is possible (although unlikely) that electrons may transfer to anatase via thermal activation. In addition, electrons may transfer to anatase due to electron trap sites, which have been reported to be more stable on anatase than rutile [71,

[146]. Excited electrons on anatase can be readily scavenged by O_2 (the primary electron acceptor) since anatase has been reported to have a higher affinity for O_2 than rutile [159]. This will consequently enhance the oxygen reduction half reaction rate, which is typically the rate determining step and thereby reduce the electron-hole recombination [34].

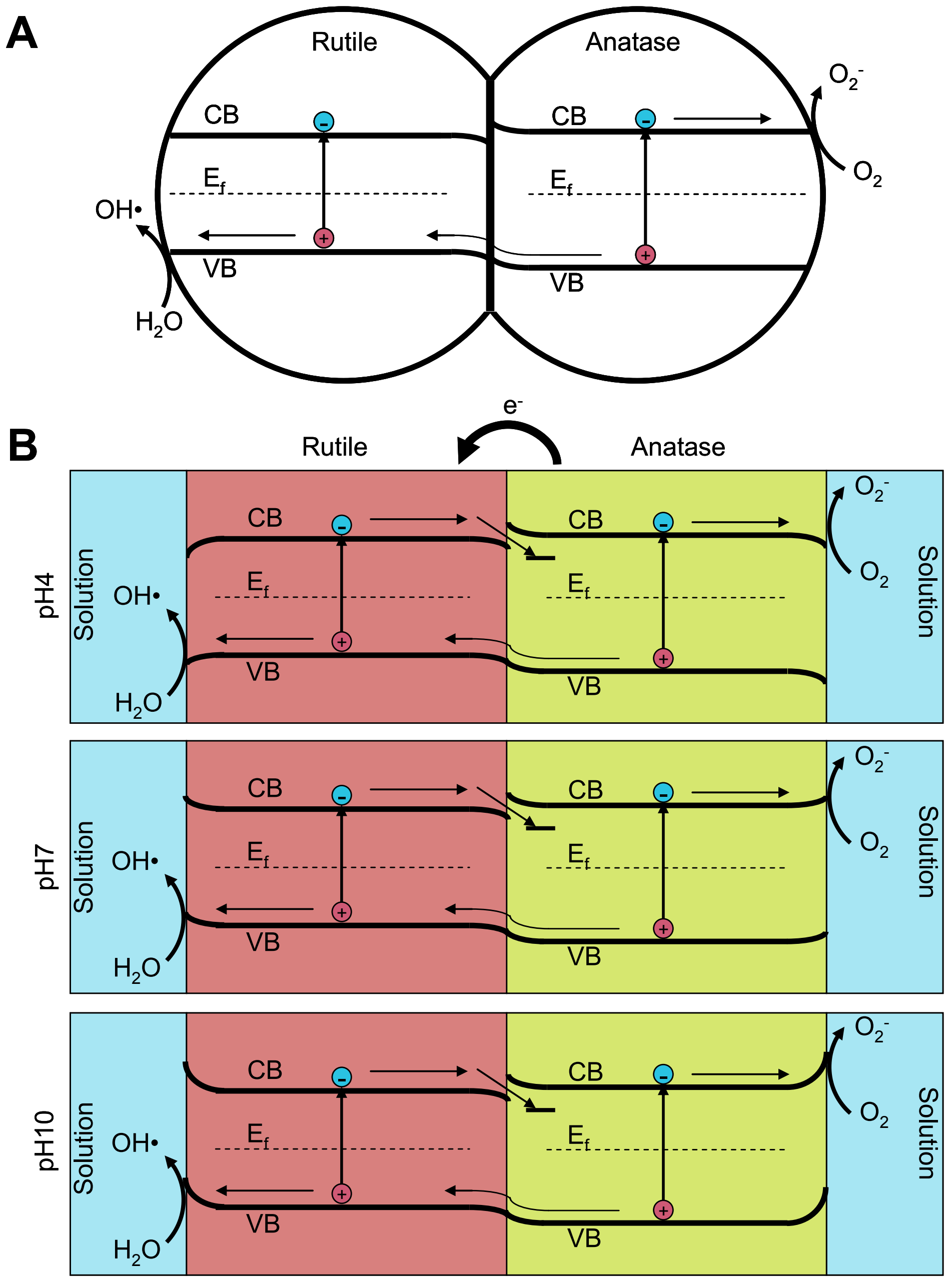

Figure 17: A) Proposed mechanism of charge separation between anatase and rutile during photocatalysis. B) Proposed mechanism of charge separation between anatase and rutile during photocatalysis at different suspension pHs on charge transfer to oxidation and reduction species.

The pH of the solution does not affect the potential difference between the band edges of anatase and rutile since they are in the same solution. However, it does effect the oxidation and reduction reactions that take place on the surface [45, 162]. The positive surface charge at pH = 4 creates an accumulation region at the solution-solid interface, which is unfavorable for hole transfer to the solution. However, it does facilitate electron transfer on anatase (as illustrated in Figure 17b). At pH = 7 and 10, the negative surface charge creates a depletion region, which facilitates hole transfer while hindering the electron transfer.

At pH 4, where MB is not readily adsorbed onto the catalyst surface, degradation is presumably achieved solely via OH• oxidation. Despite the possible enhancement of electron transport across the solution-solid interface at the lower pH, the substrate-surface interaction dominated the photocatalytic degradation of MB.

Platinum (Pt) deposition via photocatalytic reduction of ammonium hexachloroplatinate (NH_4PtCl_6) was used to characterize the location (i.e., anatase, rutile, or both phases) of the reduction half of the photocatalytic reaction that occurs on the mixed phase photocatalytic materials. UV pre-treated powders (12% rutile, which was observed to have the highest dye removal rate at pH = 7) as described above were dispersed in the prepared solutions.

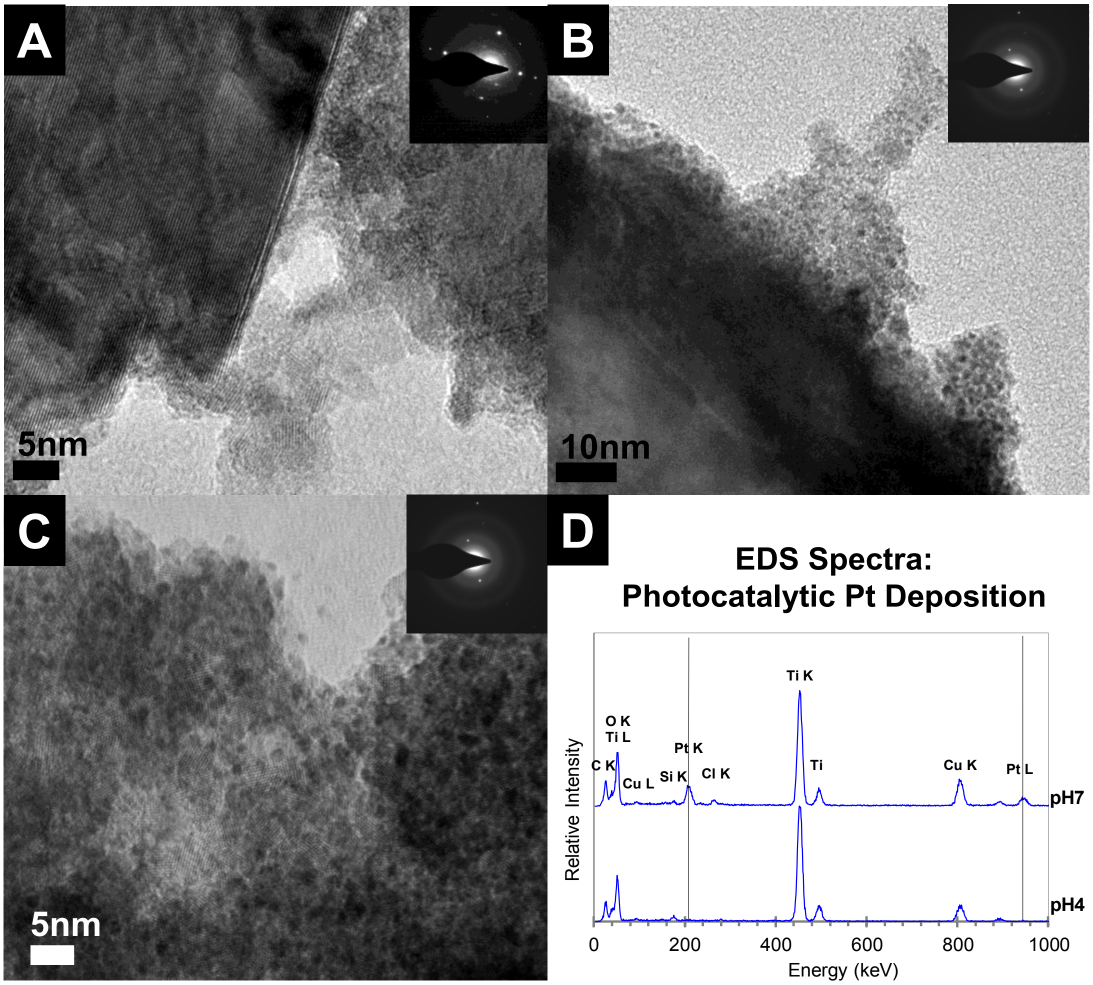

Figure 18: a) Bright field TEM micrographs of TiO_2 particles without Pt nanocrystal deposition, Pt deposition on 12% rutile material for 6 hr at pH = 7 b) Low magnification, c) high magnification, d) energy dispersive spectra of photocatalyst materials post Pt deposition at pH4 (TEM image not shown) and pH7. Selected area electron diffraction patterns are inserted for phase identification. EDS spectra are representative spectra from five regions samples.

The photocatalytic reduction of Pt (IV) to Pt (0) resulted in the subsequent deposition of Pt nanoparticles on the surface of the catalyst [163]. The presence of multiple small Pt nanocrystals (~ 2 nm) was observed on the small anatase crystals surrounding large rutile crystals shown in Figure 18. Conversely, no Pt nanoparticle deposition was observed under the same conditions at pH = 4. In addition, no Pt nanocrystals were observed on rutile crystals under any pH condition (i.e., pH = 4 or 7). The Pt deposition occurs via reduction by excited electrons from the conduction band. This indicates that the reduction reaction is occurring predominantly on the anatase crystals and not on the large rutile crystals. This supports a synergistic mechanism, where a hole generated in anatase transfers to rutile. The hole transfer results in excess electrons in anatase promoting the reduction half reaction and excess holes in rutile promoting the oxidation half reaction. The lack of Pt nanocrystals deposition on TiO_2 suspensions at pH = 4 is potentially due to the repulsion of the positively charged Pt ion by the positively charged TiO_2 surface similar to that observed with MB.

3.4 Conclusions.

The suspension pH proved to significantly affect the photocatalytic activity of the material due to reduced proximity of oxidative species to the analyte under acidic conditions and increased proximity under alkaline conditions. pH 7 was the optimal reaction condition used to characterize the effect of anatase-rutile ratios on the photocatalytic activity. We observed an optimal ratio of 20% rutile – 80% anatase at pH = 7, which is attributed to the charge transfer of holes from rutile to anatase. This hole transfer results in excess electrons in anatase promoting the reduction half reaction and excess holes in rutile promoting the oxidation half reaction.

3.5 Acknowledgements.

This work was conducted with Government support under and awarded by DoD, Office of Naval Research, National Defense Science and Engineering Graduate (NDSEG) Fellowship, 32 CFR 168a.

Chapter 4.
Photocatalytic Titanium Dioxide Composite

Nichola Kinsinger, Anthony Tantuccio, Minwei Sun, Yushan Yan, David Kisailus, Photocatalytic Titanium Dioxide Composite, Journal Nanoscience and Nanotechnology, volume 11, pp.7015-7021 (2011)

Abstract

In recent years, Titanium Dioxide (TiO_2) has gained much more interest for its semiconducting properties for use as photocatalytic material because it rapidly and completely mineralizes organic without harmful byproducts. Based on inspiration from biology, which uses organic structures to guide nucleation and growth of minerals, we demonstrate controlled synthesis of TiO_2 using a hydrophilic synthetic polymer. In the absence of the polymer, TiO_2 completely transforms to rutile by 72 hours, however with the addition of the polymer larger anatase crystallites are observed due to the reduced number of nuclei formed. Under these conditions, complete transformation to rutile was not observed due to diffusion-limited growth of TiO_2 as well as the presence of an organic coating on the crystallites. However nanoparticles are difficult to recover from effluent streams. We use the polymer to develop bulk composite TiO_2-organic structures which can be fabricated and tailored as a stand alone photocatalysts, eliminating the need for nanoparticle recovery systems, thereby reducing processing costs.

4.1 Introduction.

Rising amounts of a variety of new chemicals are now being discharged into the wastewater system due to the rapid emergence of technology and industry. The increasing sensitivity of current measurement techniques has led to the identification of new contaminants that were previously below the detection limit for drinking water and wastewater, which is causing increased concern for public health and safety [1]. Pharmaceuticals and personal care products (PPCPs), surfactants, and various industrial chemicals are known to be endocrine disrupting compounds (EDCs) and are currently not removed by typical wastewater treatment practices. A large issue to be addressed is the lack of regulations for these new emerging contaminants that are outpacing the measurement techniques to detect them. Currently the Food and Drug Administration (FDA) does not require testing when the concentration of such compound is below 1 μg/L. With the increase of industry, the spectrum of these compounds is continuing to expand along with their unknown potential health risks [1].

To accommodate the ever-increasing demand for clean drinkable water and the alarming increase in the use of personal care products and pharmaceuticals (PCPPs), new treatment methods other than the traditional processes discussed above must be implemented to remove these hazardous compounds and to degrade them to non-harmful constituents.

Degradation of organic compounds via oxidation by hydroxyl radicals (OH•) is a new potential treatment technology that does not require the significant capital investment that is needed for reverse osmosis [47]. Additionally, these radicals cause the degradation of a wide range of organic compounds to complete mineralization with no selectivity [42-44]. The Environmental Protection Agency has inventoried and classified more than 800 molecular compounds that are completely mineralized by OH• [42]. Complete mineralization of the pollutant eliminates the concern of secondary byproducts that can form when using other oxidation agents such as chlorine. Various methods are used to produce OH• from ultra-violet radiation (UV) including H_2O_2/UV, O_3/UV, H_2O_2/O_3/UV, TiO_2/UV, etc. [47]. While all of these processes produce OH• when coupled with UV, TiO_2 has the distinct advantage of being a heterogeneous catalyst that can be easily integrated into an existing treatment system and isolated from the effluent liquid stream [43].

TiO_2 is synthesized by various methods such as chemical and physical vapor deposition, which require high temperatures or extreme atmospheric conditions (e.g., high vacuum) to achieve the desired phase, shape, and size of the material [54, 77]. Solution routes such as chemical bath deposition, sol-gel and hydrothermal routes offer more environmentally friendly and lower cost processing. However, these solution-based technologies lack the necessary control of crystal size, phase, and morphology that afford semiconductor materials an optimized performance.

Nature has evolved efficient strategies, exemplified in biomineralizing systems, to synthesize materials that demonstrate nanostructural control and desirable properties [95]. It is generally thought that the combination of soluble molecules in conjunction with the underlying structural organics provides the requisite binding sites and molecular arrangement for inducing nucleation of oriented crystals with a stabilized phase (e.g., the stabilized aragonite phase of $CaCO_3$ found in nacre) [95]. Many of these soluble molecules consist of acidic residues that have a high affinity for cations, thereby facilitating their attraction and thus increasing local supersaturation levels [96, 97].

In addition, the interfacial energy between the organic template and the mineral precursor should have a significant influence towards heterogeneous nucleation by reduction of the surface free energy. After the initial nucleation has occurred, crystals may grow by a number of mechanisms including, but not limited to, the attachment of additional ions or by mesophasic self-assembly. These kinetically controlled crystallization processes are achieved by modifying the interactions of nuclei and developing crystals with soluble molecules and organic scaffolds. These interactions play a critical role in determining the particle size, habit, morphology and phase of the resulting mineral [99].

Based on inspiration from biology, which often uses these organic structures to guide nucleation and growth of minerals, we demonstrate controlled synthesis of TiO_2 using a hydrophilic synthetic polymer. Furthermore, we show that bulk composite TiO_2-organic structures can be fabricated and tailored to act as stand alone photocatalysts, eliminating the need for nanoparticle recovery systems, thereby reducing processing costs.

4.2 Preparation of materials.

TiO_2 nanocrystals were chemically synthesized under hydrothermal conditions. Titanium bis(ammonium lactato) dihydroxide (TiBALDH) solution, 50 wt % in water, was purchased from Sigma Aldrich. 1M TiBALDH solutions were prepared by diluting with de-ionized (DI) water. The pHs of these solutions were modified with ammonium hydroxide (30 wt% purchased from Acros Organics). Immediately following pH modification, solutions were placed in 23 mL, Teflon-lined hydrothermal reactors (Parr Instruments, Moline, IL) and heated to 150°C for different durations (1 - 72 hours) in convection ovens. Reactors were removed and subsequently cooled under ambient conditions. The resulting products were washed with DI water, sonicated (Branson 2510, Danbury, CT) for 30 minutes between washes to remove any unreacted precursor and reaction by-products, and then dried in air at 100°C for 24 hours.

TiO_2-organic composites were chemically synthesized under hydrothermal conditions by dissolving poly (vinyl alcohol), PVA (MW ~ 40,000, 98-99%, Sigma Aldrich) in water. Concentrated solutions of pH modified (ca. pH = 8, 9, 10, or 11) TiBALDH (1.57 M) were prepared and subsequently diluted with pH modified (i.e., the same pH as the corresponding TiBALDH solutions) concentrated aqueous solutions of PVA (1.13 g/L for a PVA:Ti molar ratio of 1:100,000; 113g/L for a PVA:Ti molar ratio of 1:100). The TiBALDH and PVA solutions were combined to make a 1M solutions of TiBALDH (molar ratio PVA:TiBALDH = 1:100,000 and molar ratio PVA:TiBALDH = 1:100). Following synthesis, the resulting rigid composites were cut into small cubes and subsequently critically-point dried to remove absorbed water while maintaining their structural integrity. The TiO_2-organic composites were then subsequently annealed at varying temperatures (i.e., 400°C, 600°C, and 800°C) for 1 hour at a rate of 10°C/minute to remove the organic within the composite and generate a higher surface area TiO_2 nanocrystallite network.

4.3 Material Characterization.

TiO_2 specimens were characterized using X-Ray Diffraction (XRD), Scanning Electron Microscopy (SEM), Transmission Electron Microscopy (TEM), Fourier Transform Infrared Spectroscopy (FTIR), energy dispersive spectroscopy (EDS), Thermal Gravimetric Analysis (TGA) and Nitrogen Adsorption Surface Area Measurements (BET). Phase identification was determined by XRD analysis (Philips X'Pert) using Cu $K\alpha$ radiation. Using the XRD diffraction patterns, crystallite diameters of anatase and rutile crystals were calculated based on the (2 0 0) and (2 1 0) reflections, respectively, from the Scherer formula (equation 5):

$$D_{(hkl)} = \frac{\kappa\lambda}{\beta\cos\theta} \tag{5}$$

where κ is the shape factor, λ the wavelength of the Cu $K\alpha$ radiation, β the full width at half maximum (FWHM) of the (h k l) peak, and θ is the diffraction angle. In order to corroborate these results, specimens were observed using TEM (T-20 and Titan, FEI) bright field imaging and electron diffraction analyses. TiO_2 nanocrystals were dispersed in ethanol, sonicated for 30 minutes, and subsequently deposited onto ultrathin carbon films on holey carbon supports with a 400 mesh copper grid (Ted Pella, Redding, CA). TiO_2-polymer composite samples were mounted with conductive adhesive on pin studs (Ted Pella, Redding, CA). The samples were then sputter coated with Au-Pd for 30 seconds. SEM imaging (FEI X-30, Netherlands) with EDS was used to characterize the morphology, particle sizing, and elemental mapping of the heat-treated composite sections.

FTIR was used to determine the extent of the hydrolysis reaction (by identifying the presence / absence of the lactato ligands). Powder samples were prepared by grinding Potassium Bromide (KBr) with 1wt% of the TiO_2 sample in a mortar and pestle, and drying for 4 hours at 100°C. 100 mg pellets were pressed using a 13 mm die (International Crystal Laboratories, #0012-2477) at 6000 psig. The pellet was placed in a Bruker Equinox 55 FTIR instrument and analyzed (50 scans) from 4000 cm-1 to 400 cm-1 at increments of 2 cm-1.

The degradation of the polymer and the TiO_2-polymer composite was observed using TGA (Mettler Toledo TGA/SDTA 851e). Samples (~100mg) were placed in the TGA and heated at 25°C to 1000°C in air.

The surface area of the powders and sectioned composites (following heat treatment) were determined via BET nitrogen adsorption at 77K using a Micromeritics ASAP 2010 apparatus. Prior to analysis samples (~100mg) were degassed at 150°C for 6 hours under vacuum. The adsorption isotherms of nitrogen at 77K were obtained using fifteen relative pressure values ranging from 0.05 to 0.35.

4.4 Results and Discussions.

4.4.1 Phase development.

The effects of polymer concentration and time on the resulting phase of TiO_2 produced from TiBALDH were investigated (Figure 19a - c). Figure 19a depicts x-ray diffraction patterns of TiO_2 synthesized in the absence of polymer at pH 9 with increasing durations. After 12 hours, the resulting phase of the TiO_2 synthesized at pH 9 is primarily crystalline anatase (JCPDS # 01-084-1286) with a small quantity of crystalline rutile (JCPDS # 01-073-1765). With increasing time, the anatase crystal size slightly increases from 4.3 ± 0.1 nm (t = 12 hours) to 4.9 ± 0.15 nm (t = 48 hours reaction time). The concentration of rutile continues to increase at the expense of anatase with complete conversion occurring by 72 hours (via XRD, Figure 19a).

Figure 19b depicts x-ray diffraction patterns of TiO_2 synthesized at pH 9 with increasing reaction durations at low polymer concentration (PVA:Ti 1:100,000 using 1M TiBALDH). Similar to the reaction without PVA, the resulting phase of the TiO_2 after 12 hours is primarily crystalline anatase with small quantities of rutile present. However, unlike the reaction without PVA, complete conversion to rutile does not occur after 72 hours (as seen in the reaction without PVA). Based on previous work that describe anatase to rutile transformation [69, 84], we believe that the presence of the polymer, which limits diffusion and reduces dissolution of TiO_2, may also inhibit the attachment of the anatase nanocrystals to the rutile crystallites [69] to enable this transformation. Likewise, the polymer effectively reduces the formation of stable anatase nuclei, as evident by the larger anatase crystallites formed in reactions with PVA versus those without PVA [53]. Figure 20a illustrates the increasingly larger anatase crystallites synthesized with PVA with increasing time, indicative of fewer nuclei [53]. Fourier Transmission Infrared (FTIR) spectroscopy was used to verify the presence of PVA on the surface of the crystallites that we believe reduces diffusion and inhibits attachment of crystallites to form rutile. Spectral peaks were identified based on appropriate references [80, 117-123]. Several peaks between 1280 – 1440 cm^{-1} are due to C–H symmetric and asymmetric stretching where with the exception of a sharp band observed at 1392 cm^{-1} (N–H stretching from residual ammonium ions) from both the precursor and PVA. The additional C–H peaks in the crystallite spectra at 1385, 2839, 2913, and 2954 are specifically associated with PVA as shown in Figure 20b. The two peaks at 1117 and 1053 cm^{-1} are from the $C–CH_3$ and C–O stretching from the precursor, respectively.

Figure 19c depicts x-ray diffraction patterns of TiO_2 synthesized at pH 9 with increasing reaction durations using high polymer concentrations (PVA:Ti 1:100 at 1M TiBALDH). Unlike the first reaction conditions (Figure 19a), only anatase is observed after 12 hours with additional peaks present from the crystallized polymer. However, in this reaction condition (i.e., significantly higher concentrations of PVA), the formation of rutile is not observed at all even after 72 hours reaction time. This is most likely due to limited diffusion of Ti-species in solution to form stable rutile nuclei as well as inhibition of particle attachment. This limited diffusion of Ti-species under high polymeric concentrations greatly reduces the crystal growth phase of the reaction due to reduced crystal surface contact as a result of the increased solution viscosity [53, 69].

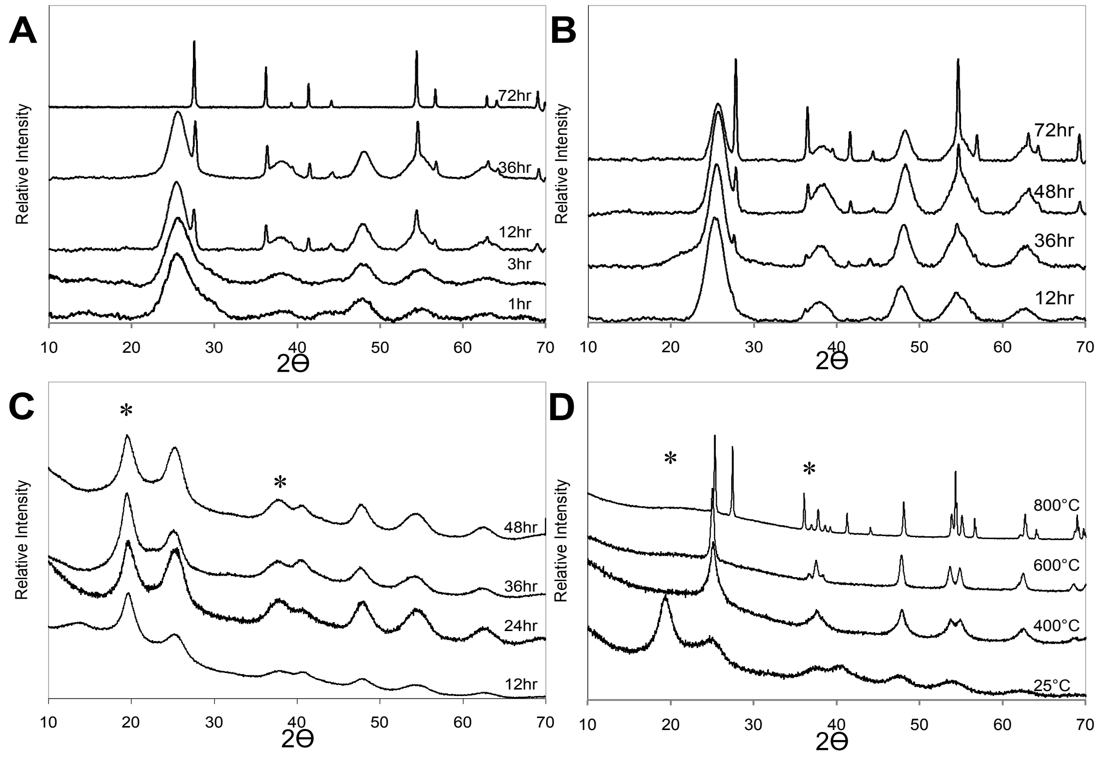

Figure 19. X-ray diffraction of TiO_2 nanocrystals formed at 150°C, pH 9 with A) No PVA added, B) PVA:Ti 1:100,000, C) PVA:Ti 1:100 with increasing reaction time, and D) PVA:Ti 1:100 with increasing annealing temperature in air. (* indicates crystalline PVA).

Figure 19d depicts x-ray diffraction patterns of TiO_2 synthesized at pH 9 150°C for 12 hours with high polymer concentration (PVA-Ti 1:100 using 1M TiBALDH) and subsequently annealed in air for 1 hour at increasing temperatures. The initial phase of the TiO_2 at 25°C, 400°C, and 600°C is nanocrystalline anatase (additional peaks in the

25°C sample are due to the crystallization of the polymer). By 800°C, a mixture of both anatase and rutile is observed. With increased annealing temperatures, the anatase crystallite size increases from 3.4 ± 0.27 nm at 25°C to 30 ± 6.2 nm at 600°C. By 800°C, 600 ± 70 nm rutile crystals are observed with 101 ± 28 nm anatase crystallites. TEM (Figure 21a – d) imaging was used to confirm crystallite size, and phase at different temperatures. At room temperature, small crystallites of anatase are seen distributed in an amorphous matrix. With increasing temperature, however, these crystallites continue to grow until they begin transformation to the rutile phase at 800°C. SEM (Figure 22a – d) observations were also used to confirm grain growth. The phase transformation to rutile is clear in Figure 22d, where 600 nm rutile grains are observed, growing within a matrix of 100 nm anatase crystals.

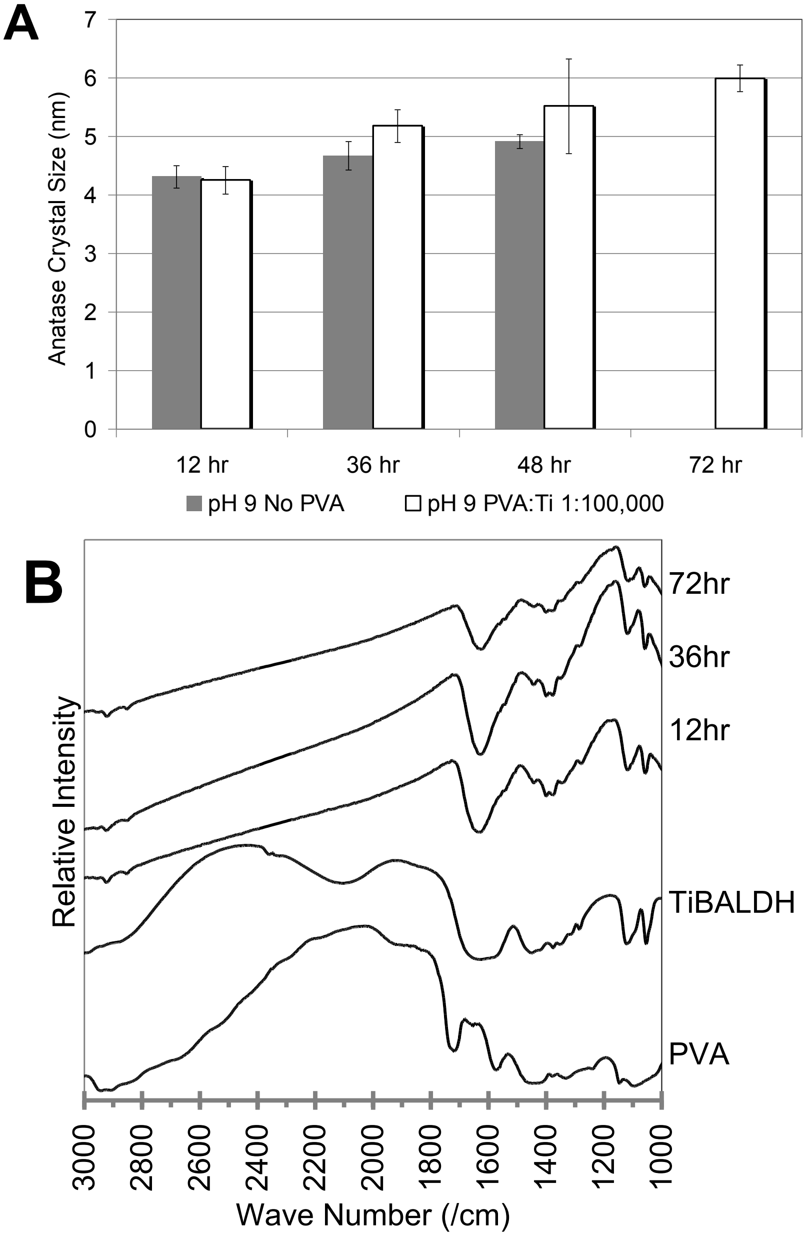

Figure 20. A) Anatase crystallite diameters (calculated using the Scherer equation using FWHM values obtained via XRD) with and without PVA with increasing reaction durations. B) FTIR spectra of TiO_2 nanocrystals formed at 150°C pH 9 with PVA (PVA:Ti ratio 1:100,000), with increasing reaction time.

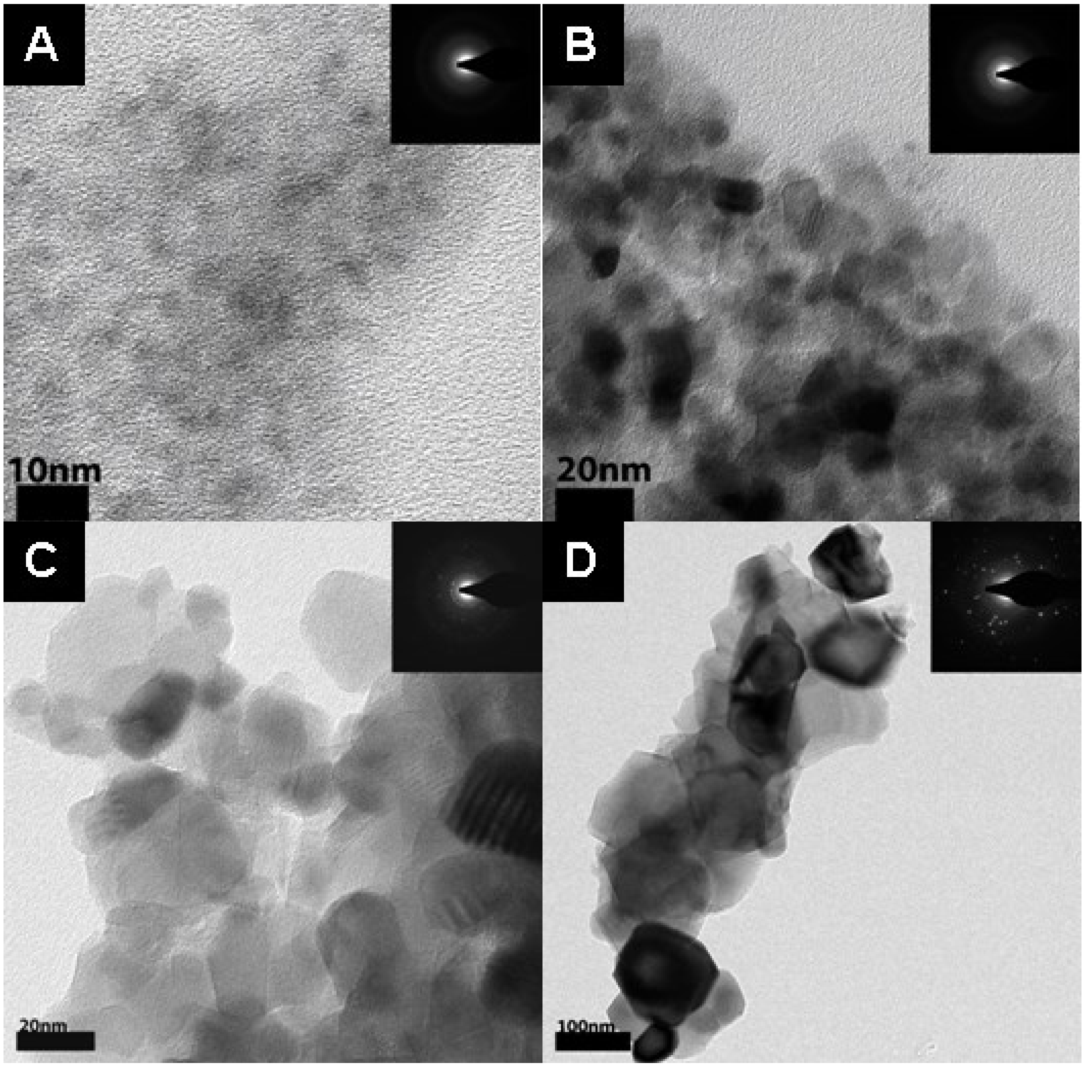

Figure 21. Bright-field TEM micrographs of TiO_2-polymer composites annealed in air for 1 hour at A) 25°C, B) 400°C, C) 600°C, and D) 800°C. Selected Area Diffraction Patterns (SADP, inserted in the top right of each micrograph) were used for phase identification.

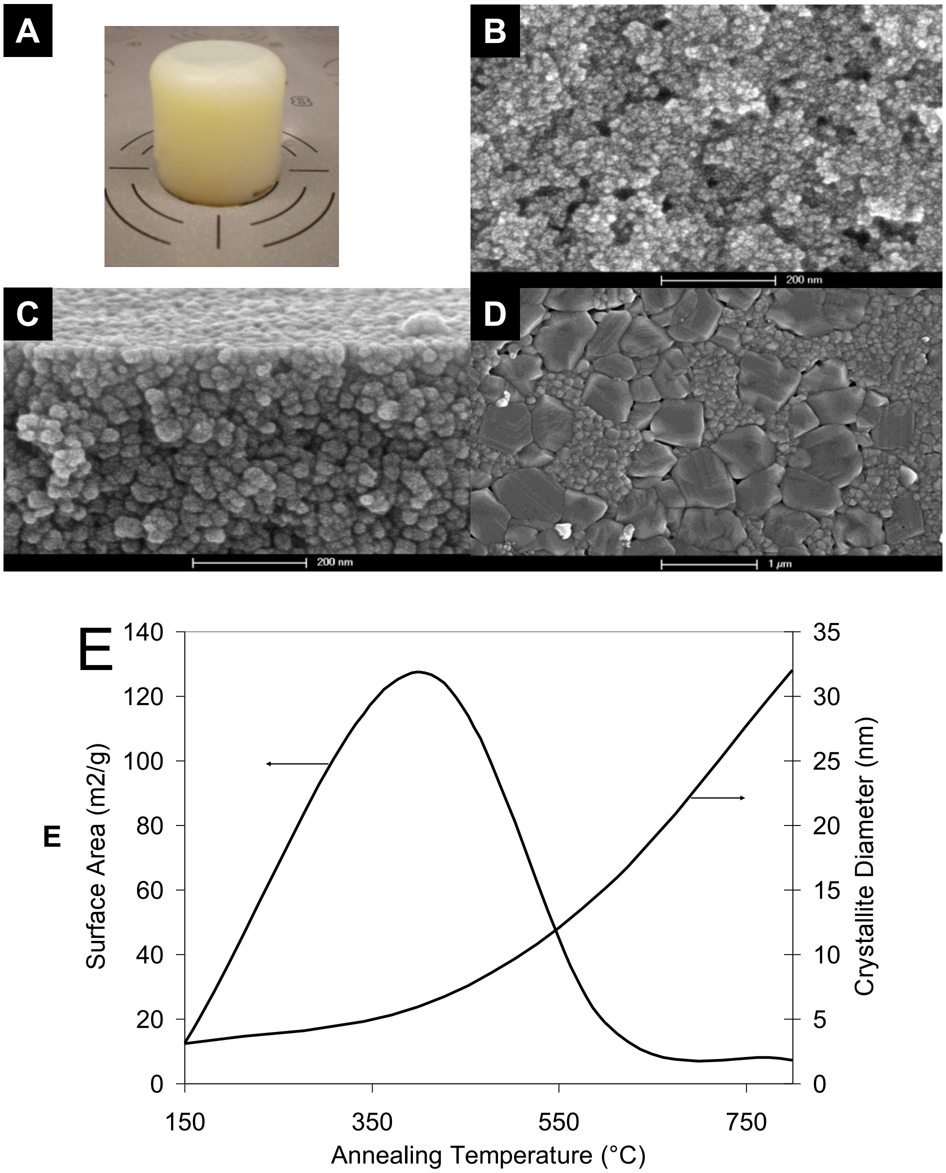

Figure 22. A) Image of TiO_2-PVA composite (directly from the reactor) formed from hydrothermal reaction at 150°C. SEM images of cube-sections of TiO_2-PVA composites after annealing in air for 1 hour at B) 400°C, C) 600°C, and D) 800°C. E) Specific surface area and crystallite diameters of TiO_2-polymer composites with increasing annealing temperatures demonstrating the reduction of surface area with significant grain growth.

4.4.2 Structural characterization of TiO_2-polymer composite.

At high polymer concentrations (PVA:Ti 1:100), a rigid and stable TiO_2-polymer composite is observed (shown in Figure 22a). We speculate that during the synthesis, either the hydrolyzed Ti species (e.g., $Ti(OH)_4$) or hydroxylated TiO_2 nanoparticles act as bridging ligands between polymer chains, effectively linking neighboring chains and increasing the viscosity of the solution illustrated in Figure 23a. Sufficient links between chains will enable the formation of the elastic composite structure observed.

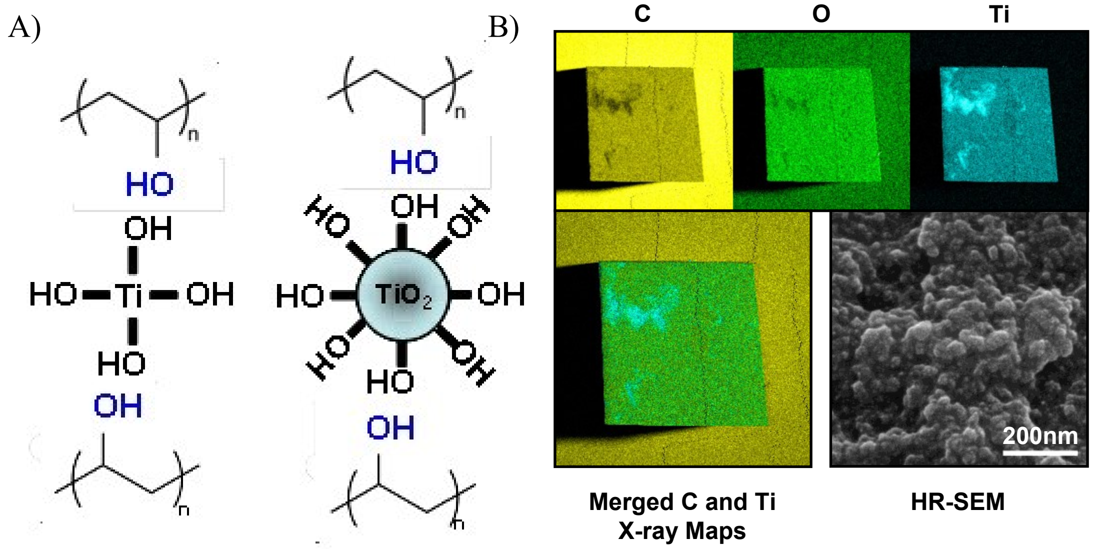

Figure 23. A) Illustration of polymer interactions to form the elastic composite structure. B) X-Ray elemental maps and a SEM image of the sectioned TiO_2-Polymer composite (without annealing).

Elemental mapping of a sectioned TiO_2-polymer composite reveals that although the samples have heterogeneities, it is largely homogeneous (Figure 23b). These observations indicate that during the synthesis, there is a small amount of phase separation between the polymer and the precursor / TiO_2 crystallites. It is likely that an increase in solution viscosity during the synthesis severely limits diffusion of Ti-species and / or TiO_2 crystallites, leading to these heterogeneities.

Thermal Gravimetric Analysis (TGA) was used to observe the decomposition of PVA from the composite with respect to temperature. TGA analyses of polymer alone (Figure 24a) exhibits significant weight loss by 400ºC, with most of the polymer removed by 500ºC, with 4% carbon remaining beyond 700ºC.

Fourier Transmission Infrared (FTIR) spectroscopy was used to identify the presence of polymer and any polymer-TiO_2 interactions in the composite at higher temperatures. Spectral peaks were identified based on appropriate references [80, 117-123]. The broad adsorption peak observed near 3500 cm^{-1} is due to the presence of hydroxyl groups, while peaks at 2980, 2925, and 2870 cm^{-1} are associated with the C–H stretching vibration from the lactato ligands of TiBALDH and the PVA. Several peaks between 1280 – 1440 cm^{-1} are due to C–H symmetric and asymmetric stretching with the exception of a sharp band observed at 1392 cm^{-1} (N–H stretching from residual ammonium ions). The two peaks at 1117 and 1053 cm^{-1} are from the $C–CH_3$ and C–O stretching, respectively. After hydrothermal treatment, the FTIR spectrum resembles the PVA spectrum (Figure 24b). With increasing annealing temperatures, the carbon signature (ca. 2900 cm^{-1} and 1280-1440 cm^{-1}) decreases. By 400°C, most of the polymer is removed, as indicated by the reduction of the carbon peaks described above. At 600°C, all peaks associated with carbon are no longer present, signifying complete pyrolysis of the polymer from the composite which is in agreement with the degradation of the polymer via TGA as seen in (Figure 24a).

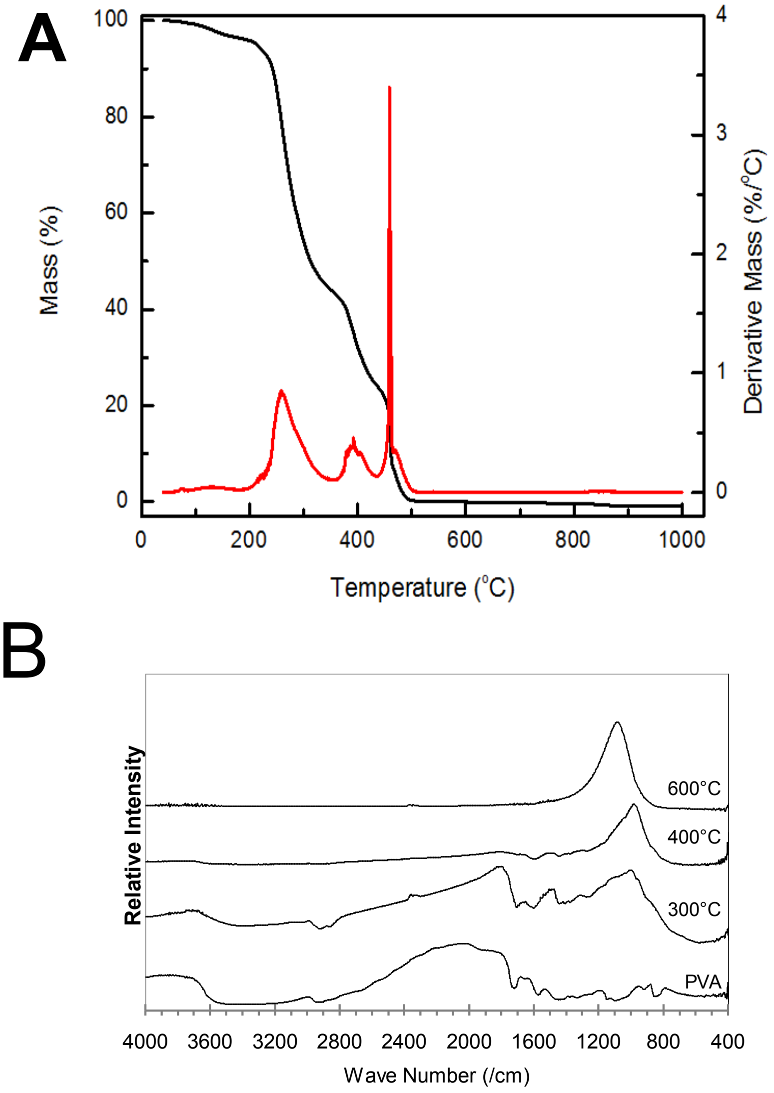

Figure 24. TGA analyses of A) PVA only B) FTIR spectra of TiO_2-PVA composites formed at 150°C pH 9, annealed at increasing temperatures.

Nitrogen adsorption (BET) measurements were conducted to evaluate the surface area of the TiO_2-polymer composite after heat treatments. At 400°C, the specific surface area is ~90-100 m2/g, which is the maximum surface area obtained after annealing the TiO_2-polymer composite (Figure 22e). This coincides with the degradation of the polymer within the composite (as observed in TGA, Figure 24). This pyrolysis yields a porous network of TiO_2 crystallites, which is responsible for the increase in the surface area of the composite. However, at 600°C, the surface area greatly decreases due to significant grain growth as illustrated in both Figure 22c and Figure 22e.

4.5 Conclusion.

In this work, we studied the phase development and growth TiO_2 under hydrothermal conditions from an organometallic precursor (TiBALDH) in the presence of a synthetic polymer, PVA, as a function of reaction time. In the absence of PVA, TiO_2 completely transforms to rutile by 72 hours. Upon addition of PVA to the reaction, larger anatase crystallites are observed due to the reduced number of nuclei formed. Under these conditions, complete transformation to rutile was not observed due to diffusion-limited growth of TiO_2 as well as the presence of an organic coating on the crystallites. By increasing the polymer concentration during the reaction a rigid and stable TiO_2-polymer composite is formed. This composite can be subsequently heat-treated in air to pyrolyze the polymer to develop a porous, high surface area TiO_2 nanoparticle composite.

Chapter 5.
Grain growth and phase transformation within porous photocatalytic membrane

In preparation.

Kinsinger, N. M.; Salinas, C.; Cotrez, P.; Solomon, L.; Major, T.; Nelson, K.; Dakak, N.; Dudchenko, A.; Kisailus, D., Growth and phase transformation within porous photocatalytic composite. *in preparation*

Abstract

Titanium dioxide (TiO_2) is an inexpensive semiconducting material since it is one of the most abundant materials found within the earth's crust. This makes it an attractive material for use as a photocatalyst to degrade the emerging organic contaminants that are causing concern for public health and safety. We investigated the effects of firing temperature, time, airflow rate, and solution processing temperature on the grain growth and phase transformation of TiO_2 within a porous membrane. The material properties evolved from these processing parameters ultimately impacts its photocatalytic performance. One such property that is critical to photocatalytic performance is crystalline phase. Here, we observed that air flow rate had a significant effect on the onset temperature of the anatase to rutile phase transformation. This is because air flow rate controls the rate of removal of the organic binder that ultimately controls how fast inorganic grains will impinge on one another, leading to phase transformation. The resulting transformation to rutile occurred at lower temperatures (750°C) at 100cm^3/min versus 10cm^3/min (850°C). Additional thermal experiments were performed to identify the rate of phase transformations, which revealed a dependence on mass density as well as temperature and time. Firing conditions were selected to perform photocatalytic degradation tests. Optimized synthesis conditions (TiO_2 membranes annealed at 700°C) resulted in 83% of analyte being removed within 30 minutes. Since cost is important in engineering application, we investigated the effects of reduced initial synthesis temperatures on grain growth and phase transformations. TiO_2-PVA samples that were initially prepared at 80°C initiated transformation to rutile at 700°C (4.7±1.2% rutile, increasing to 36.5±2.0% by 800°C). This transformation occurred a significantly lower temperature compared to samples initially prepared at 150°C (rutile observed at 850°C). Interestingly, the anatase crystallite size at the onset of rutile formation was approximately 30nm for both hydrothermal processing conditions.

Keywords. TiO_2, titania, phase transformation, anatase-rutile, photocatalysis,

---

5.1 Introduction.

With an increasing concern over the presence of endocrine disrupting compounds within drinking water sources, TiO_2 nanomaterials are gaining interest as photocatalytic agents in environmental remediation via degradation of organic pollutants[42, 54, 59]. The photocatalytic activity, bandgap, and surface area of TiO_2 are influenced by its crystalline phase and size. Therefore, investigation of grain growth and phase transformations in this material is critical [63, 71, 164]. Varying synthesis parameters such as pH, temperature, time, solvent, etc. have been demonstrated have an effect of the resulting phase and crystallite size[53, 77, 84].

Titanium is the fourth most abundant metal and the ninth most abundant element component in the earth's crust (~0.63%) [34]. It is found bound in minerals like ilmentite (titanium iron oxide) and perovskite (calcium titanium oxide) as well as more pure mineral forms of titanium dioxide: anatase, brookite, and rutile (which may contain up to 10% iron impurities) [10]. Approximately 98% of the world's production of TiO_2 is used for pigments. In the last 40 years, it has become the focus of photocatalytic research since the discovery by Fujishima and Honda of its ability to photocatalytically split water [34, 39]. Nanoceramics such as TiO_2 have attracted much attention for their unique properties such as photoactivity, corrosion resistance, high surface area, phase stability, and enhanced sinterability[58-63, 65]. Such advanced ceramics constitute 17% of a multibillion dollar ceramic industry and thus, there is constant competition to become more efficient and reduce processing costs[63].

Recently, we have reported the synthesis of a TiO_2-composite using a water soluble precursor and polyvinyl alcohol that once fired, yields a high surface area bulk photocatalytic material[165]. Here, we investigate the effect of polymer on the grain growth and phase transformation of TiO_2, which ultimately impacts photocatalytic performance. The use of this bulk photocatalytic material eliminates the need for downstream recovery systems, which represents a majority of the total costs for the implementation of slurry based photocatalyst systems. In order to reduce costs of such a material, we investigate the effect of reducing the processing temperatures of the green material (i.e., non-fired) on the resulting ceramic. The study of phase stability and transformation kinetics is critical since anatase (a metastable phase) has been observed experimentally to be the more photocatalytically active phase whereas a mixture of these phases (i.e., anatase and rutile) has been observed to be more photocatalytically active[59, 70, 71, 146]. Sintering and phase transformation of nanocrystalline materials occurs at lower temperatures than coarse crystals, which greatly affect processing conditions, time, and cost[62, 69].

There are three modes of anatase to rutile phase transformation: interface, surface, and bulk nucleation, which are dictated by temperature, crystal size, number of contacts, and surface defects[69, 93]. Anatase and rutile are both composed of octahedrally coordinated Ti; however, they have distinct structures that require breaking 7 out of 24 Ti–O bonds per unit cell to transform anatase to rutile[69]. At lower firing temperatures (~400°C-800°C), thermal fluctuations on the surface and within the bulk of anatase are not enough to induce a transformation from anatase to rutile. However, when anatase nanocrystals are in contact with one another, rutile-like elements may form and serve as a rutile nucleation site with a reduced activation energy than that of bulk or surface nucleation[69, 93]. Similarly, thermal fluctuations on the surface and within the bulk form rutile-like elements that serve as rutile nucleation sites at higher temperatures. Coarser anatase materials lack large numbers of interfaces for interface and surface nucleation of rutile and therefore increased sintering temperatures and times are required for bulk nucleation [69, 93]. Nanocrystalline anatase materials have higher surface areas and increased numbers of interfaces necessary for interface and surface nucleation, which reduce the temperature and time needed for phase transformation to rutile [69, 93]. Here, we investigate the effects of processing conditions such as synthesis and firing temperature, air flow rates during firing, and firing time on the grain growth, phase transformation, and surface area of the resulting porous TiO_2 membrane materials. TiO_2 has three crystalline phases: anatase, rutile, and brookite. Anatase and rutile are the two photocatalytically relevant phases; however, anatase, a metastable phase, has been observed to be more photocatalytically active than rutile [45, 46, 70, 71]. This study of crystal growth and phase transformation kinetics is critical since a mixture of anatase and rutile has been observed to be more photocatalytically active than either independent phase [59, 70, 71, 146, 164].

5.2 Materials and Methods.

TiO_2 powders were chemically synthesized under hydrothermal conditions using Titanium bis (ammonium lactato) dihydroxide (TiBALDH) solution as the precursor (50 wt % in water, Sigma Aldrich). 1M TiBALDH solutions were prepared by diluting with deionized (DI) water. The pHs of these solutions were modified with ammonium hydroxide (30 wt%, Acros Organics). Immediately following pH modification, solutions were placed in Pyrex glass test tubes, sealed, and heated at selected temperatures (i.e., 80°C and 150°C) for varying reaction times (i.e., 15 minutes to 12 hours). Reactors were removed and subsequently cooled under ambient conditions. The resulting products were washed with DI water, sonicated (Branson 2510, Danbury, CT) for 30 minutes between washes to remove any unreacted precursor and reaction by-products, and dried in air at 100°C for 24 hours.

TiO_2-organic composites were chemically synthesized under hydrothermal conditions with polyvinyl alcohol (PVA, MW ~ 40,000, 98-99%, Sigma Aldrich), ball milled to particle sizes less than 149 μm, and a TiBALDH solution. TiBALDH and PVA solutions were mixed to make a 1M solution (molar ratio PVA:TiBALDH = 1:100) that was modified to pH=9, as previously described[85]. Immediately following pH modification, solutions were placed in Pyrex glass test tubes, sealed, and heated at selected temperatures (i.e., 80°C and 150°C) for varying reaction times (i.e., 15 minutes to 12 hours). Following synthesis, the resulting rigid composites (i.e., PVA-TiO_2) were cut into discs and then dehydrated using ethanol to remove absorbed water while maintaining their structural integrity. Subsequently, the dried, green materials were fired at high temperatures (i.e., 400°C – 900°C in 50°C increments) for 1 hour at 10cm^3/min or 100cm^3/min air flow rates and a heating rate of 10°C/min to remove the organic template and yield a high surface area TiO_2 nanocrystalline ceramic network.

5.2.1 Material Characterization.

TiO_2 specimens were characterized using X-Ray Diffraction (XRD), Scanning Electron Microscopy (SEM), Transmission Electron Microscopy (TEM), Fourier Transform Infrared Spectroscopy (FTIR), Thermal Gravimetric Analysis (TGA) and Nitrogen Adsorption Surface Area Measurements (BET). Phase identification was determined by XRD (Rigaku Smartlab) using Cu Kα radiation. Using the XRD patterns, crystallite diameters of anatase and rutile crystals were calculated based on the (1 0 1) and (1 1 0) reflections, respectively, from the Scherer formula (equation 6):

$$D_{(hkl)} = \frac{\kappa\lambda}{\beta\cos\theta} \tag{6}$$

where, κ is the shape factor, λ the wavelength of the Cu Kα radiation, β the full width at half maximum (FWHM) of the (h k l) peak, and θ the diffraction angle. The relative composition of crystalline rutile was determined via the following equation (equation 7):

$$x_r = \frac{I_R}{I_R + 0.884 I_A} \tag{7}$$

where, I_A and I_R are the integrated intensities of anatase (101) and rutile (110) peaks, respectively [69]. In order to corroborate these results, specimens were observed using TEM (T-12, FEI) bright field imaging and electron diffraction analyses. TiO_2 nanocrystals were dispersed in ethanol, sonicated for 5 minutes using a tip-horn ultrasonic processor (Hielscher UP100H, Ringwood, NJ), and subsequently deposited onto ultrathin carbon films on holey carbon supports with a 400 mesh copper grid (Ted Pella, Redding, CA). SEM imaging (FEI X-30, Netherlands) was used to characterize the morphology and particle size. TiO_2-polymer composite samples were mounted with conductive adhesive on pin studs (Ted Pella, Redding, CA). The samples were then sputter coated with Pt-Pd for 30 seconds.

FTIR was used to determine the extent of burnout of the polymer. Powder samples were prepared by grinding Potassium Bromide (KBr) with 1wt% TiO_2 sample in a mortar and pestle, and drying for 4 hours at 100°C. 100 mg pellets were pressed using a 13 mm die (International Crystal Laboratories, #0012-2477) at 6000 psig. The pellet was placed in a Bruker Equinox 55 FTIR instrument and analyzed (100 scans) from 4000 cm^{-1} to 400 cm^{-1} at increments of 2 cm^{-1}.

The degradation of the polymer and the TiO_2-polymer composite were observed using thermal gravimetric analysis (TGA) and differential scanning calorimetry (DSC, TA Instruments SDT Q600, New Castle, DE). TGA samples (~10mg) were heated in air at 10°C/min from 25°C to 800°C. The air flow was set at $20cm^3/min$. DSC samples (~10mg) were heated at 10°C/min from 25°C to 800°C in dry argon at $20cm^3/min$.

The surface area of the powders and sectioned composites (following heat treatment) were determined via BET nitrogen adsorption at 77K (Micromeritics ASAP 2020, Norcross, GA). Prior to analysis, samples (~30mg) were degassed at 150°C for 6 hours under vacuum. The adsorption isotherms of nitrogen at 77K were obtained using 40 relative pressure values ranging from 0.01 to 0.95 for BET surface area and pore size distribution measurements.

Synchrotron X-ray data was collected at the X13B beamline at the National Synchrotron Light Source, Brookhaven National Laboratory, using 19 keV X-rays (λ= 0.65 Å) and a beam spot focused to ca. 5μm × 5μm. Specimens consisting of fired composites embedded in Epofix resin and sliced with a diamond saw to create 0.5 mm thick slices, which were mounted onto the beamline sample holder in transmission geometry. Transmitted x-ray intensity was recorded using a photodiode detector fixed beyond the sample at the beam stop and normalized by the incident intensity measured with an upstream ion chamber. Diffraction data were acquired with a Princeton Instruments CCD detector approximately 15 cm beyond the sample. Using a sintered rutile standard, the software package Datasqueeze, and a JCPDS data card for rutile, the detector pixel positions were calibrated to Q-values. X-ray composition maps were acquired across the cross-sectional samples, with each spot separated by 100μm in the x-direction and 50μm in the y-direction. The relative compositions were measured via integrated intensities of (1 0 1) and (1 1 0) reflections of anatase and rutile, respectively, and calculated using equation 7.

5.2.2 Photocatalytic Performance.

The efficiency and effects of membrane processing conditions on photocatalytic activity were determined by measuring the degradation of Methylene Blue (MB) in the presence of TiO_2 suspensions (ground membranes) under UV illumination. Prior to degradation testing, TiO_2 suspensions were prepared by dispersing the TiO_2 powders in filtered deionized water (0.22μm, Millipore), adjusting the pH to 7 with hydrochloric acid or ammonium hydroxide, and sonicating for 5 minutes using a tip-horn ultrasonic processor (Hielscher UP100H, Ringwood, NJ). Any residual organics remaining on the surface of the TiO_2 photocatalytic material (i.e., from the synthesis process) were removed by irradiating the material for 24 hours prior to testing with UV light (Phillips UV (A) 40 Watt bulb at $1mW/cm^2$).

In a typical degradation reaction, a glass reactor was filled with 100mL containing (i) a 500mg/L TiO_2 suspension and (ii) 13μM solution of Methylene Blue (MB) maintained at 25°C and magnetically stirred at 500 rpm. The photon source was a Phillips UV (A) 40 Watt bulb operated at $1mW/cm^2$. At the start of each degradation experiment, MB (under dark conditions) was allowed to absorb onto the suspended TiO_2 for one hour prior to irradiation, followed by direct irradiation with the photon source. The photocatalytic activity was monitored by measuring the absorbance of MB via UV-Visible Spectroscopy (Beckman Coulter DU 800 Spectrophotometer) between 200 – 800nm (λ_{max}=668nm).

Reaction rates were determined by fitting the MB degradation over time with pseudo-first order equation:

$$C_t = C_o e^{-kt} \tag{8}$$

where, C_t is the concentration of MB in solution at time t, C_o is the initial concentration of MB in solution, and k is the pseudo-first order rate constant.

5.3 Results and Discussion.

5.3.1 Isochronal Crystal growth and phase transformation.

Anatase is a metastable phase of TiO_2, which is often the initial solution synthesis product due to its higher stability than rutile at crystal sizes less then 14nm [52, 59, 61, 62, 67, 68, 129]. X-Ray diffraction of green composites and powders revealed diffraction peaks from anatase (JCPDS # 01-084-1286)[165]. Firing of powder samples at an air flow rate of 10cm^3/min results in an increased growth of anatase crystals from 4.6 ± 0.3nm at 400°C to 28.8 ± 0.3nm at 850°C (as observed in XRD, Figure 25a). Increasing the air flow rate to 100cm^3/min does not significantly affect crystal growth or the phase transformation to rutile (Figure 26a). Due to minimal residual organic (~30% organic and adsorbed water via TGA, Figure 27a) present in powder samples as compared to the composite samples, which has a significant amount of organic (~85% organic as determined by TGA), it is expected that increased air flow will have a negligible effect. The presence of rutile is first observed at 650°C for both flow conditions, with complete conversion to rutile observed at 850°C. The anatase crystal size at the onset of rutile is 13.0 ± 0.5nm, which is consistent with previous studies [62, 68]. At sufficiently small crystal sizes (i.e., < 14 nm), the free energy of rutile (bulk and surface) is higher than that of anatase and thus, the relative phase stability of anatase and rutile is reversed [68]. The transition point (i.e., crystallite size) at which rutile becomes the more stable phase has been observed to occur around anatase crystal sizes of 14nm [62].

Subsequent firing of green materials at an air flow rate of 10cm^3/min produces porous materials with an increased grain growth of anatase crystals from 4.6 ± 1.5nm at 400°C to 34.5 ± 3.2nm at 850°C (as measured by XRD, Figure 25b). Increasing the air flow rate to 100cm^3/min during firing results in a subtle increase in the anatase crystal size (7.0 ± 1.1nm at 400°C to 36.5 ± 0.6nm at 850°C). Under either air flow conditions (i.e., 10 or 100cm^3/min), 100% conversion to rutile is observed by 900°C. However, the onset of rutile formation at 100cm^3/min occurred at 700°C (vs. 800°C at 10cm^3/min, Figure 26b).

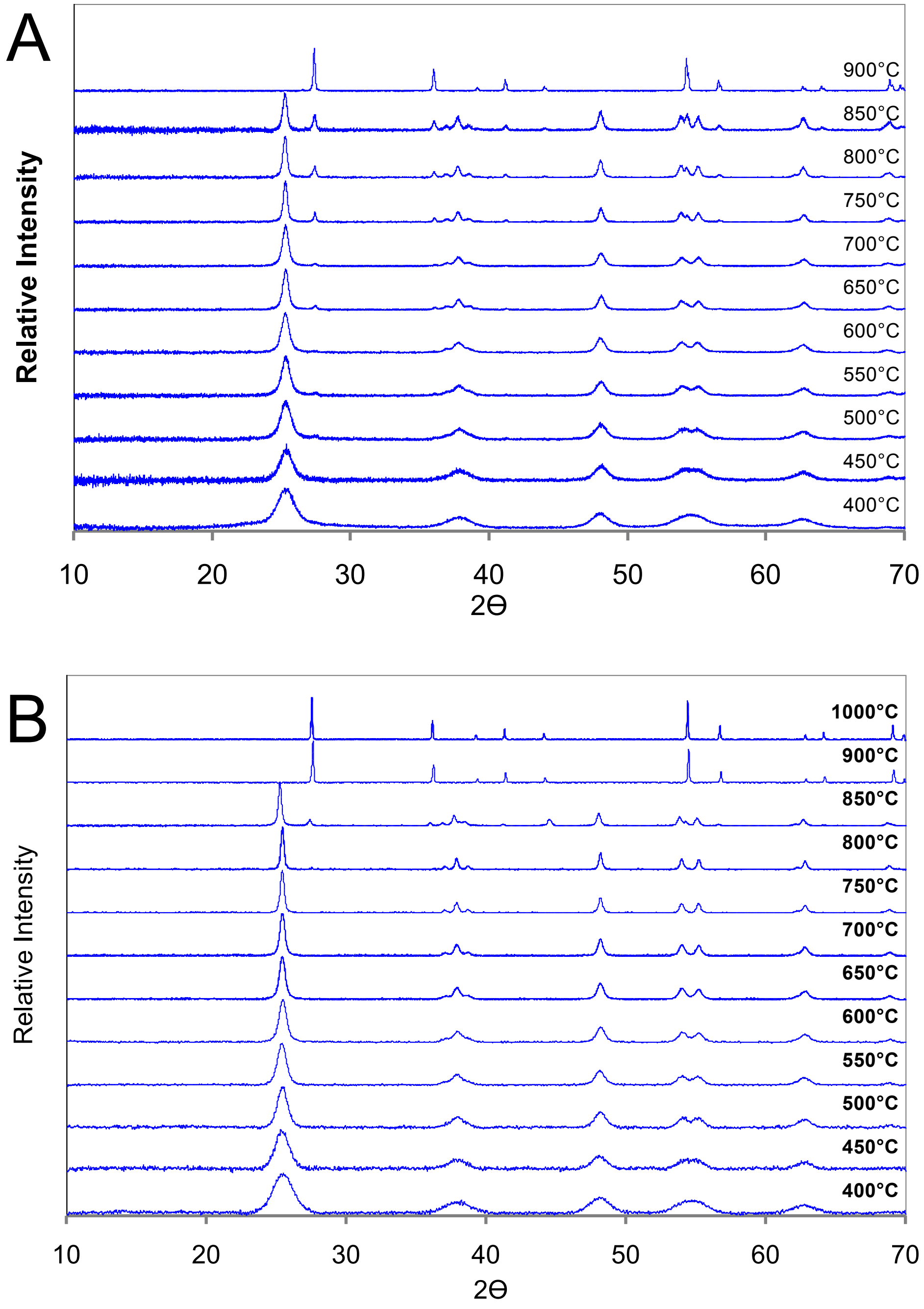

Figure 25: Representative X-ray Diffraction patterns of A) TiO_2 powders without PVA; B) TiO_2 prepared with PVA (composites).

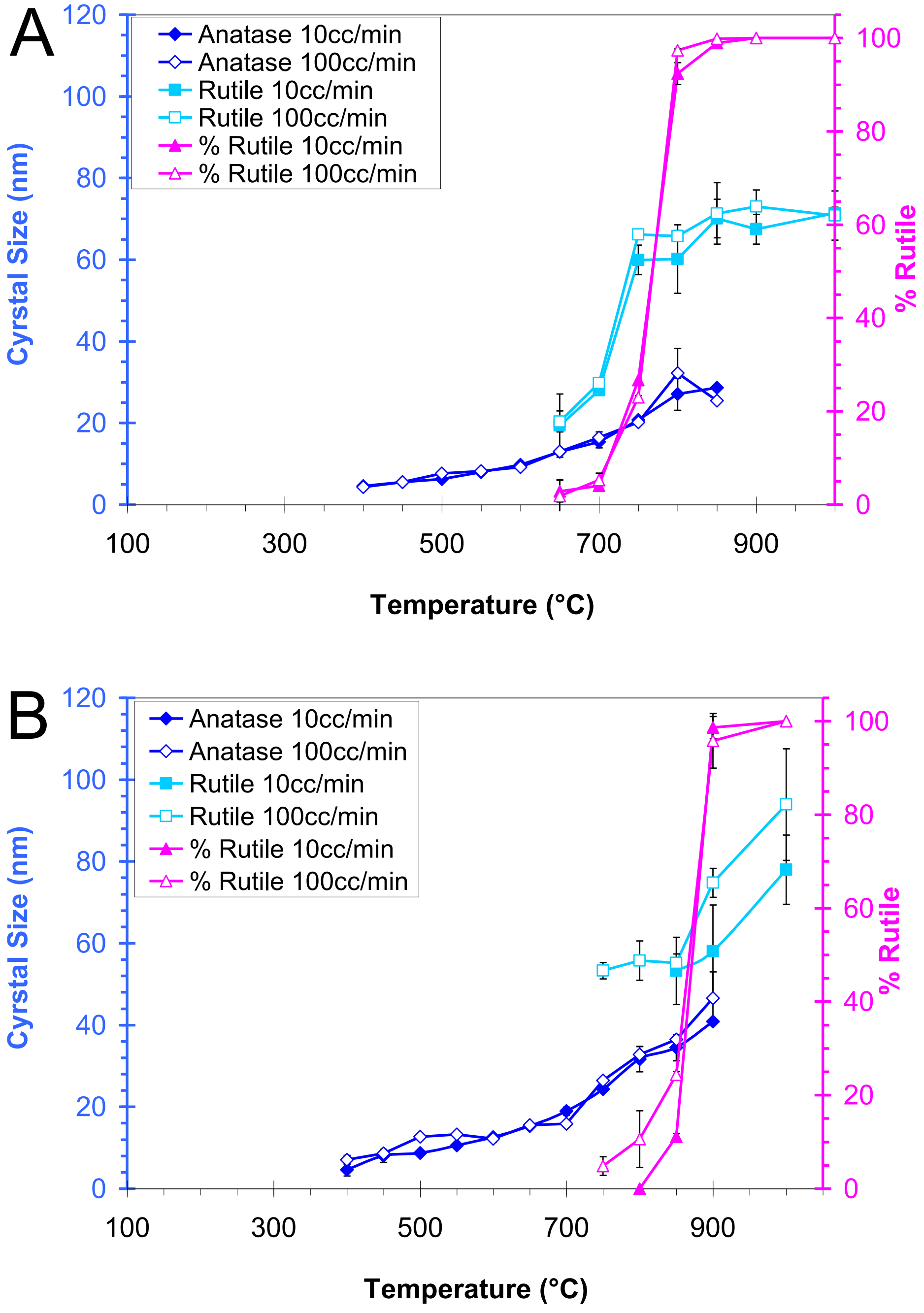

Figure 26: Anatase and Rutile crystal size and percent rutile of composite materials versus firing temperature A) TiO_2 powders without PVA; B) TiO_2 prepared with PVA (composites).

The presence of PVA in the composite material, as observed previously[85], retards the phase transformation to rutile (as compared to the powder samples during isochronal firing). In contrast to the ~13nm anatase crystal size observed at the onset of rutile formation in the powders, anatase crystal sizes at the onset of rutile formation were 34.5±3.2nm and 29.6±1.9nm in composite materials fired at 10cm^3/min at 100cm^3/min, respectively. This indicates that the polymer restricts the anatase-anatase particle contacts, thus limiting interfacial nucleation and diminishing the rate of phase transformation to rutile [69, 93, 166]. However, increasing the air flow rate subsequently lowers the temperature at which rutile is first observed, suggesting that oxygen required for the combustion of the polymer is the limiting reactant. Therefore, at the higher flow rate, there is more complete removal of the polymer at lower temperatures increasing the probability of more anatase-anatase particle interactions that may lead to the phase transformation to rutile. Thermal gravimetric analysis (Figure 27b) highlights the effect of the air flow rate on the removal of carbon compounds from the composite.

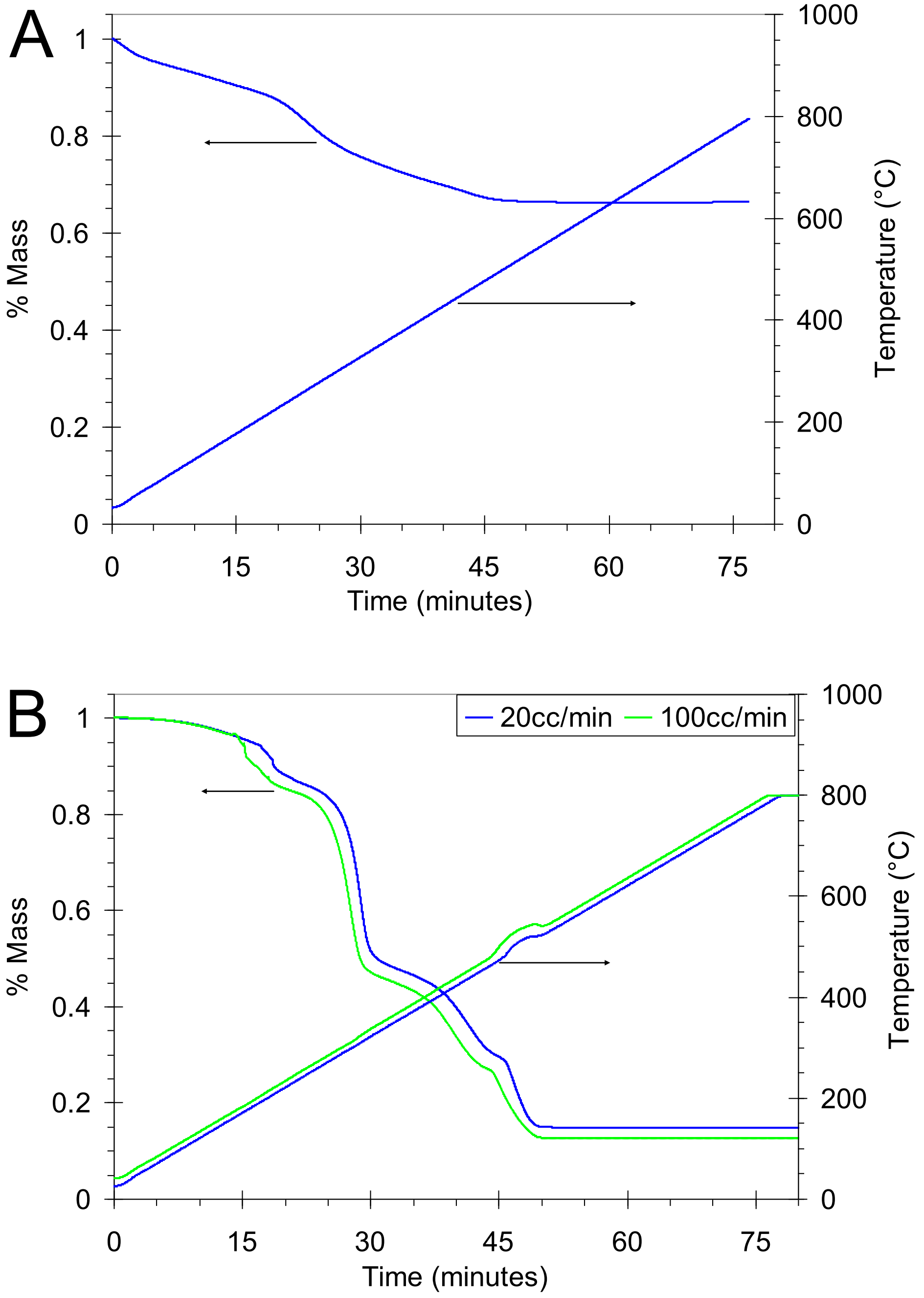

Figure 27: TGA of A) TiO_2 powders without PVA; B) TiO_2 prepared with PVA (composites) under the different air flow conditions.

Using synchrotron X-ray diffraction of thinned sections of composite, the initial formation of rutile within the composite was observed (Figure 28). The broad pore size distributions (up to 1mm) that are observed both in the synchrotron beam transmission plot and optical image (Figure 28a) are attributed to the heterogeneity of the polymer and titanium dioxide distribution within the green material. EDS mapping (Figure 28c) confirms these observations. The distribution of rutile through the annealed sample (Figure 28b, d) reveals elevated concentrations of rutile along the pore walls. The anatase crystal sizes on the outside surfaces of pore walls are larger since they will have a higher diffusivity than those within the wall (bulk). Thus, the transformation is more likely to occur on the wall than within the wall. During the firing of the composite materials, significant heat is released from the combustion of the PVA (as observed in the exothermic peak shown in Figure 27, starting at 45 minutes). The presence of the large pockets of polymer may result in localized heating of the sample that yield higher concentrations of rutile within these pore walls. Additionally there is an increased mass density within these pore walls, increasing the probability of anatase interactions and promoting the interface nucleation.

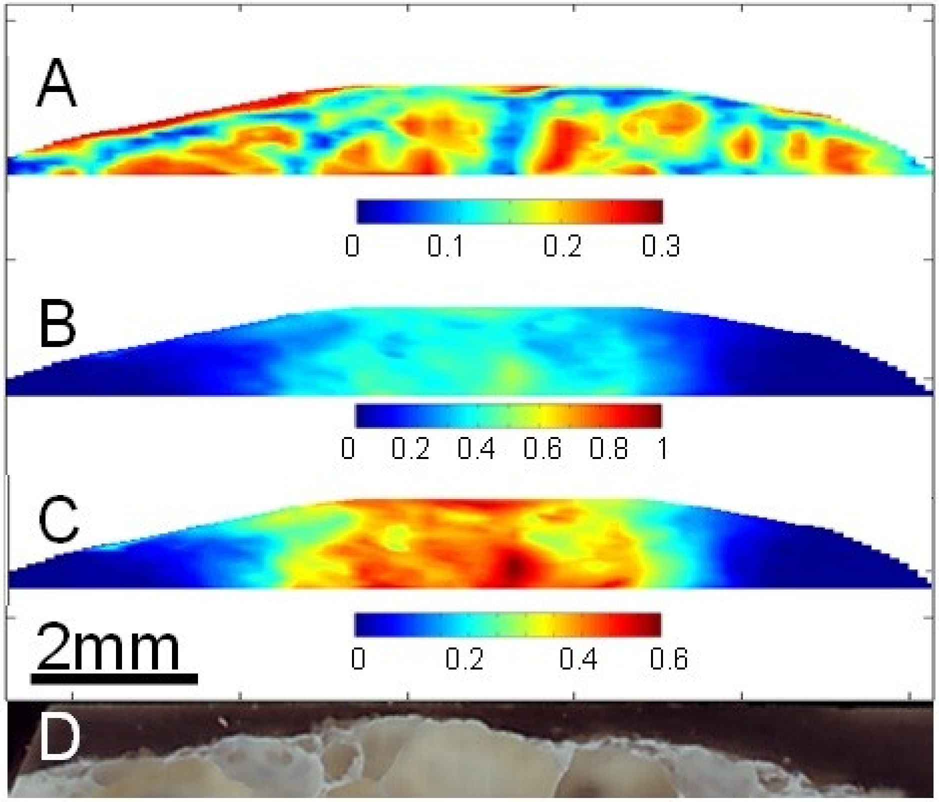

Figure 28: Synchrotron map of membrane fired at 800°C for 1 hour at an air flow rate of $10cm^3/min$. A) X-ray transmission map (relative to sample thickness), B) percentage of rutile (0-100% scale), C) percentage of rutile (0-60% scale) and D) optical micrograph of scanned sample.

Consistent with the increase of large pores with temperature as observed in synchrotron transmission maps, there is an observed increase in the average pore size and size distribution as measured via N_2 adsorption (Figure 29). The large pockets of carbon-based species (likely PVA) that are observed in EDS maps of green materials (Figure 23b) and are subsequently removed upon burnout and produce large pores in the membrane. The large pores only continue to grow since the grains are significantly smaller than the large pores (pores >1.5 x grains: 31.7±3.1nm anatase crystals at

800°C)[60]. This promotes the development of even larger pores and the elimination of small pores with increasing firing temperatures [60]. This ultimately limits the control of porosity and reduces the surface area of the material.

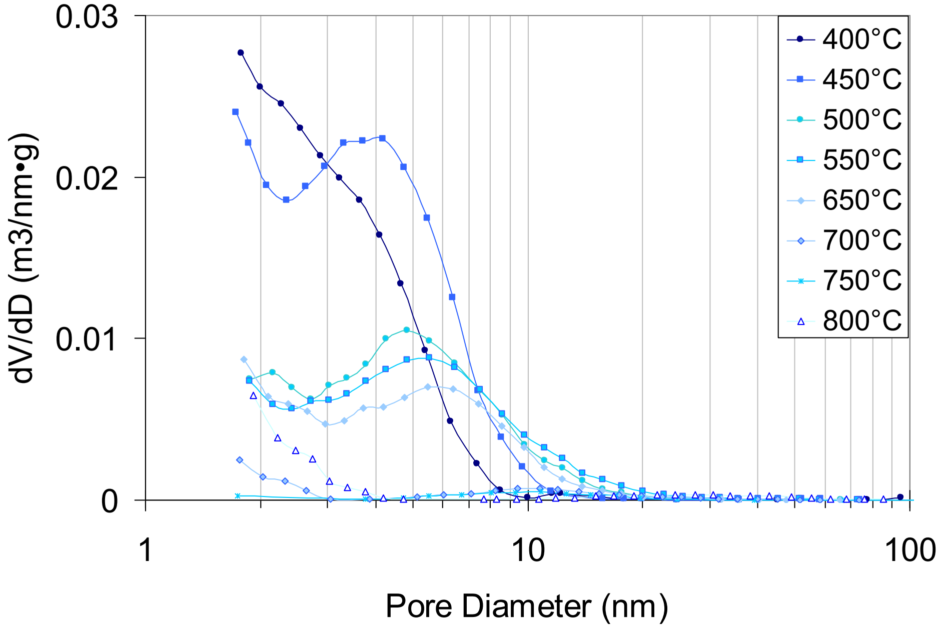

Figure 29: Pore size distributions of composite materials after firing as measured using N_2 adsorption.

5.3.2 Isothermal Crystal growth and phase transformation.

Firing experiments were conducted at 800°C, 850°C, and 900°C to determine the kinetics of rutile phase transformations within the composite materials. Consistent with observations from the isochronal firing (Figure 26), increased anatase and rutile crystal sizes are observed at elevated temperatures and at higher air flow rates (Figure 30). As has been previously observed, there is a sinusoidal fluctuation in both anatase and rutile crystal sizes [61]. This fluctuation (i.e. as observed at 12 hours) is attributed to the preferential phase transformation of the larger anatase crystals resulting in an average decrease in the anatase and rutile crystal sizes (i.e., rutile fluctuations are observed due to production of “new” smaller rutile crystals from the anatase phase transformations). As expected, temperature has a significant effect on the rate of rutile transformation. For example, 40.2±8.6% rutile is observed at 800°C after 24 hours compared to 100% rutile at 900°C for 1 hour (2% mass detection limit). Air flow rate also has a significant effect on the rate of phase transformation. For example, when heating samples to 800°C at different flow rates, 40.2±8.6% rutile is observed after 24 hours at $10cm^3$/min versus 40.8±3.1% at after only 12 hours at $100cm^3$/min. In addition, there is a “step” in the transformation to rutile in the 800°C kinetic experiments there is a “step” in the transformation to rutile at both air flow conditions. The higher air flow rate reduces the onset time of this “step”.

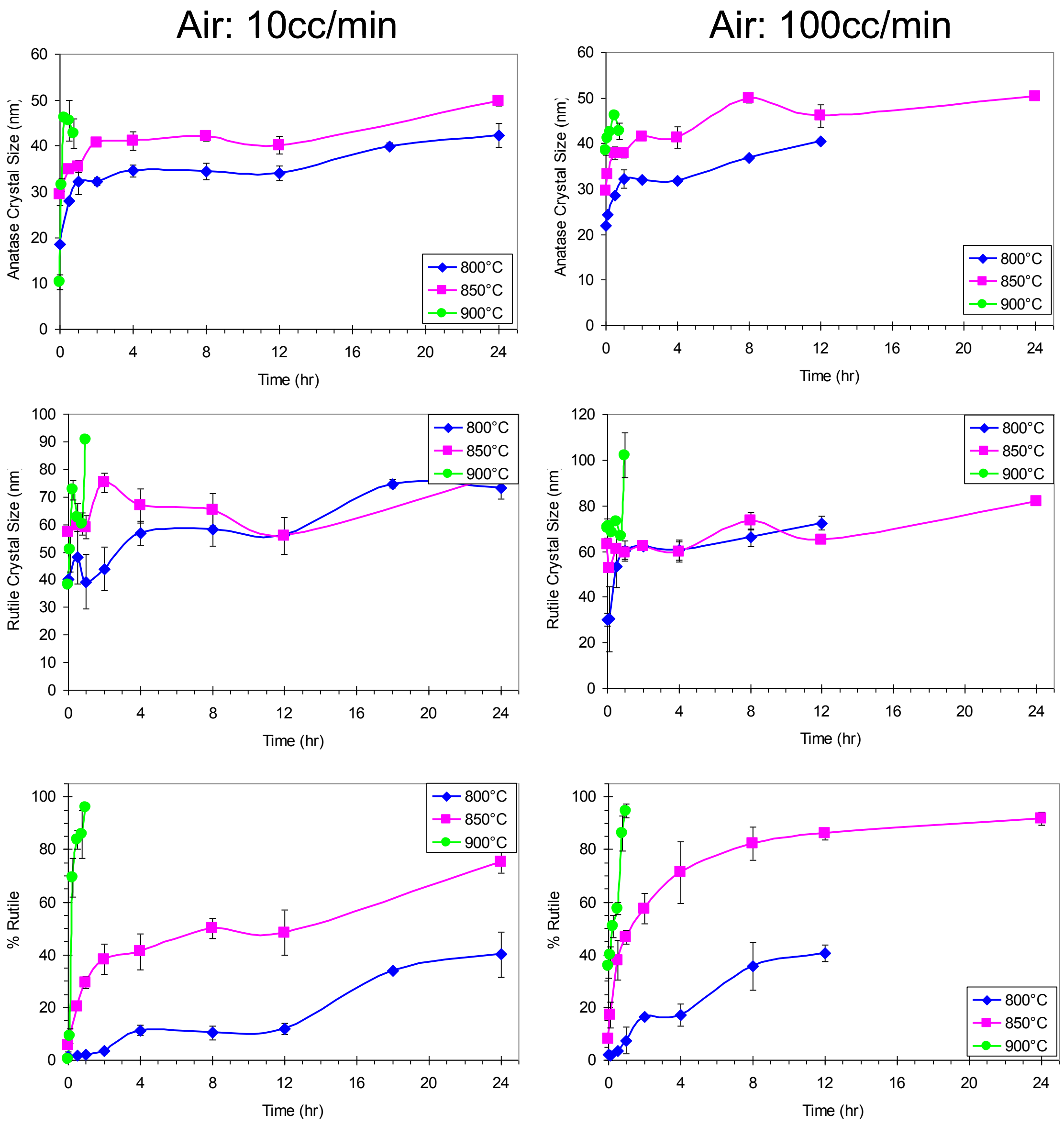

Figure 30: Crystal sizes of anatase and rutile, and fraction of rutile versus temperature at air flow rates of 10cc/min and 100cc/min.

Several traditional models have been applied previously to the nanocrystalline anatase to rutile phase transformations and have been found to be invalid [69]. Phase transformations of nanocrystalline materials occurs at reduced temperatures versus those of coarse crystals. This is due to crystal size, number of contacts, and surface defects [62, 69, 93]. The different modes of transformation that have been observed and account for nanocrystalline effects are: interface, surface, and bulk nucleation[62, 69, 93]. At lower firing temperatures (~400°C-800°C), thermal fluctuations on the surface and within the bulk of anatase are not enough to induce transformation of anatase to rutile. However, anatase nanocrystals that are in contact with one another may induce the formation of rutile-like elements that subsequently serve as a rutile nucleation sites with reduced activation energy versus those of bulk or surface nucleation[69, 93]. Similarly, thermal fluctuations on the surface and within the bulk of anatase form rutile-like elements that serve as rutile nucleation sites at higher temperatures. Coarse grained anatase lacks large numbers of interfaces and high surface area necessary to observe either interface and surface nucleation of rutile [69, 93].

Zhang and Banfield (1999)[93] developed a model for interface nucleation, which accounts for the effect of nanocrystalline anatase on phase transformations at temperatures between 465°C and 525°C. The interface nucleation is attributed the rate of nucleation due to the probability of two anatase crystals contacting each other (i.e., related to "concentration" of anatase particles), resulting in the derived interface nucleation kinetic equation [93]:

$$\frac{(D_a / D_o)^3}{(1-\alpha)} - 1 = (k_2 N_O)t \tag{9}$$

where, D_a is the mean size of anatase crystal as measured by X-ray diffraction (XRD), D_o is the mean initial size of anatase crystals as measured by (XRD), t is time, α is the weight fraction of rutile measured by XRD, N_o is the initial number of anatase crystals, and k_2 is the kinetic constant for interface nucleation. The kinetic constant is relevant to the sample volume and the initial sample characteristics and therefore k_2N_o can be defined as a complex constant.

However, at temperatures greater than 600°C, nucleation on free surfaces of anatase crystals (i.e., without anatase-anatase contact) becomes a significant contribution to the phase transformation to rutile [69]. Zhang et al. developed a model that builds upon the interface nucleation adding surface nucleation, which becomes significant at higher temperatures [69]. The resulting kinetic model is as follows:

$$\frac{(D_a / D_o)^3}{(1-\alpha)} - 1 = \left(1 + \frac{k_2 N_O}{k_1}\right)\left(e^{k_1 t} - 1\right) \tag{10}$$

where, k_1 is the kinetic constant for surface nucleation. By plotting the left side of the equation versus time the kinetic constants and the mode of rutile nucleation can be determined. The kinetic analysis of the crystal size and phase (from Figure 30) is presented in Figure 31. As previously mentioned, there is an observed “step” in the 800°C and 850°C conditions, which does not fit the two step (interface then surface nucleation) model, as described by equation 11.

$$y = y(IN) + y(SN) \tag{11}$$

y(IN) and y(SN) represent the interface and surface nucleation contributions as described in equations 12 and 13, where, t_x is the period of time where interface nucleation is saturated.

$$y(IN) = k_2 N_o t_x \left(1 - e^{-t/t_x}\right) \tag{12}$$

$$y(SN) = e^{k_1 t} - 1 \tag{13}$$

A

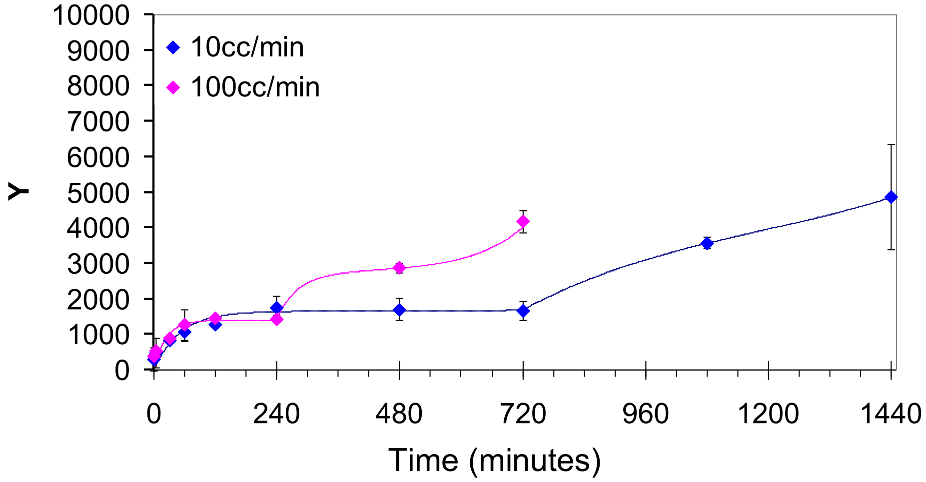
10000
9000
8000
7000
6000
5000
4000
3000
2000
1000
0
Y
10cc/min
100cc/min
0
240
480
720
960
1200
1440
Time (minutes)

B

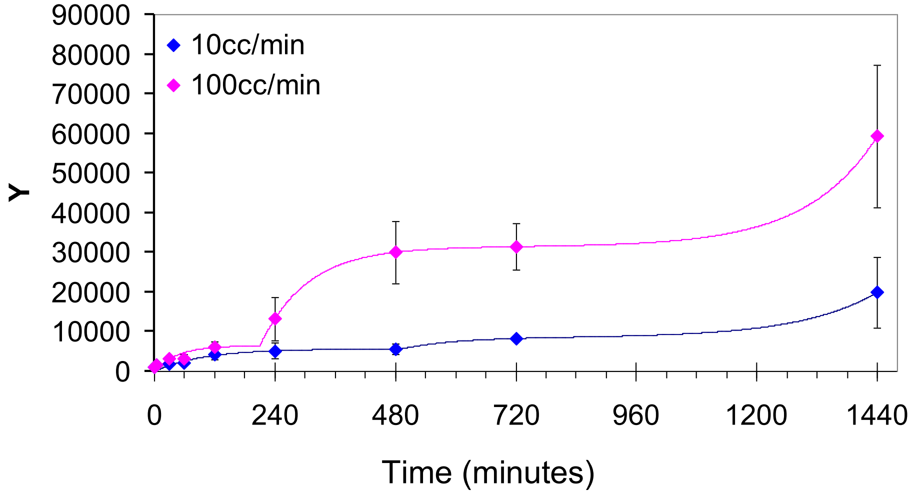
90000
80000
70000
60000
50000
40000
30000
20000
10000
0
Y
10cc/min
100cc/min
0
240
480
720
960
1200
1440
Time (minutes)

C

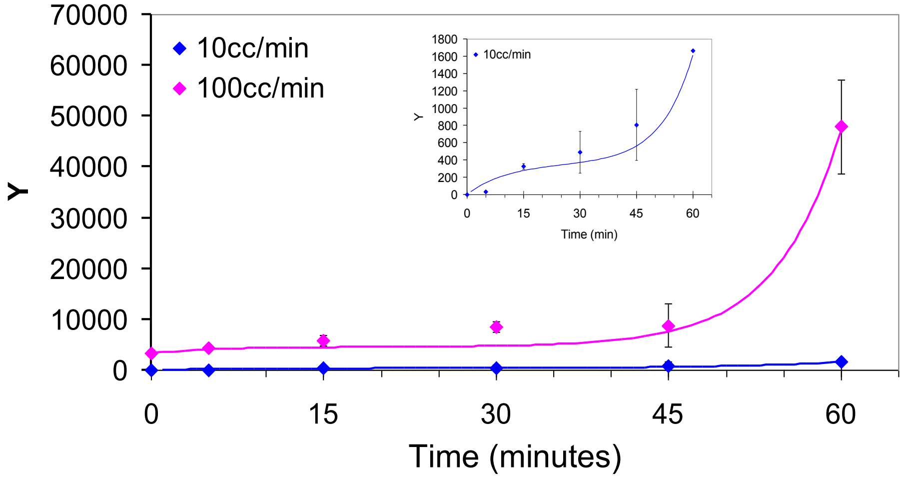
70000
60000
50000
40000
30000
20000
10000
0
Y
10cc/min
100cc/min
0
15
30
45
60
Time (minutes)
1800
1600
1400
1200
1000
800
600
400
200
0
Y
10cc/min
0
15
30
45
60
Time (min)

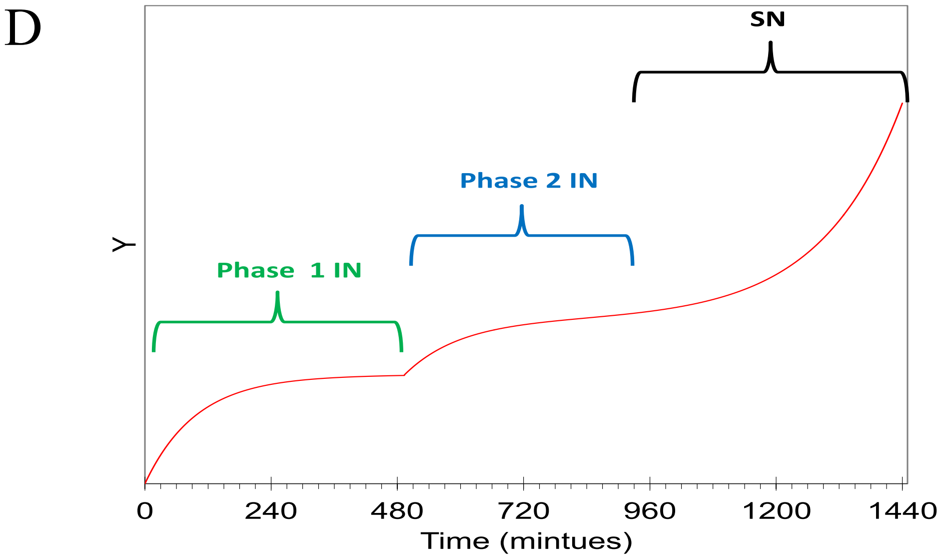

Figure 31: Plot of the function $y=(D_a/D_0)^3/(1-\alpha)-1$ versus time for composites fired at A) 800°C, B) 850°C, and C)900°C with air flow rates of $10cm^3/min$ and $100cm^3/min$ to model rutile interface and surface nucleation. D) Plot of ideal function y with phase 1 IN and phase 2 IN and SN identified.

The observed "step" in the thermal annealing data is attributed to the densification of the material due to its highly porous nature. This effect is observed due to the irregular and inconsistent pore sizes and distributions cause the shrinking of small pores. This results in increased anatase-anatase contacts, once again initiating a second interface nucleation prior to domination of the phase transformation via surface nucleation (as observed by Synchrotron mapping, indicating a high rutile concentration in pores walls, Figure 28). Thus, an additional interface nucleation step function term is required to describe the effect of densification within these porous materials. The k_3N_{o3} and t_{x3}

represent the kinetic terms for the secondary interface nucleation and t_s is the onset time of the second interfacial nucleation phase.

$$y = \begin{cases} k_2 N_o t_x \left(1 - e^{-t/t_x}\right) & t < t_s \\ k_2 N_o t_x + k_3 N_{o3} t_{x3} \left(1 - e^{-t/t_{x3}}\right) + e^{k_1 t} - 1 & t > t_s \end{cases} \tag{15}$$

The incorporation of the second "step" of interfacial nucleation into the rutile nucleation model kinetic analysis is presented in Figure 31. As expected, increasing the annealing temperature reduces the onset time of surface nucleation. By 900°C, surface nucleation dominates the rutile nucleation with a minimally observed interface nucleation contribution. Increasing the air flow rate during firing increases the rate of interfacial nucleation for both phases; this is caused by the increased rate of organic removal, increasing the number of anatase-anatase interactions.

Table 5: Fitted interface and surface nucleation model parameters

Temp (°C)	Air (cm^3/min)	k_1 (1/min)	k_2N_o (1/min)	T_x (min)	k_3N_{o3} (1/min)	T_{x3} (min)	T_s (min)
800	10	0.0047	32.3	51.2	7.8	354.3	720.2
800	100	0.0099	58.5	23.9	31.7	42.8	239.2
850	10	0.0065	58.3	97.3	27.1	105.9	493.6
850	100	0.0071	142.1	45.7	266.8	93.4	210.6
900	10	0.119	34.2	10.4			
900	100	0.178	1262.3	5.5			

Applying these models to the kinetics of phase transformation of our composite materials, we are able to determine the mode of transformation and evaluate the effect of processing parameters on the kinetic constants for our system. This is significant for such systems involving nanocrystalline materials to control the phase transformation and sintering of such materials and is fundamental to their properties and applications [53, 59, 68, 70, 71, 77, 84, 146].

5.3.3 Photocatalytic Characterization of Selected Isochronally Fired Materials.

Photocatalytic degradation of the analyte dye was performed on materials at selected firing conditions: 400°C, 600°C, 700°C, and 800°C. Membrane materials annealed up to 700°C that were prepared under both air flow conditions (10cm^3/min and 100cm^3/min) reveals increasing organic degradation rates (Figure 32). However, the degradation efficiency is greatly reduced in materials prepared at 800°C. The removal percentage of MB by 240 minutes by materials prepared at 400°C, 600°C, 700°C, and 800°C under 10cm^3/min air flow was 64%, 95%, 98%, and 77%, respectively, with 79% removed within 30 minutes by materials fired at 700°C. Similarly, removal of MB by 240 minutes using materials prepared at 400°C, 600°C, 700°C, and 800°C under 100cm^3/min air flow was 93%, 92%, 100%, and 56%, respectively, with 83% removed within 30 minutes by materials fired at 700°C. When irradiated with UV (A) light in the absence of the TiO_2 catalyst, no obvious degradation of MB was observed; therefore direct photolysis was negligible at all experimental conditions considered.

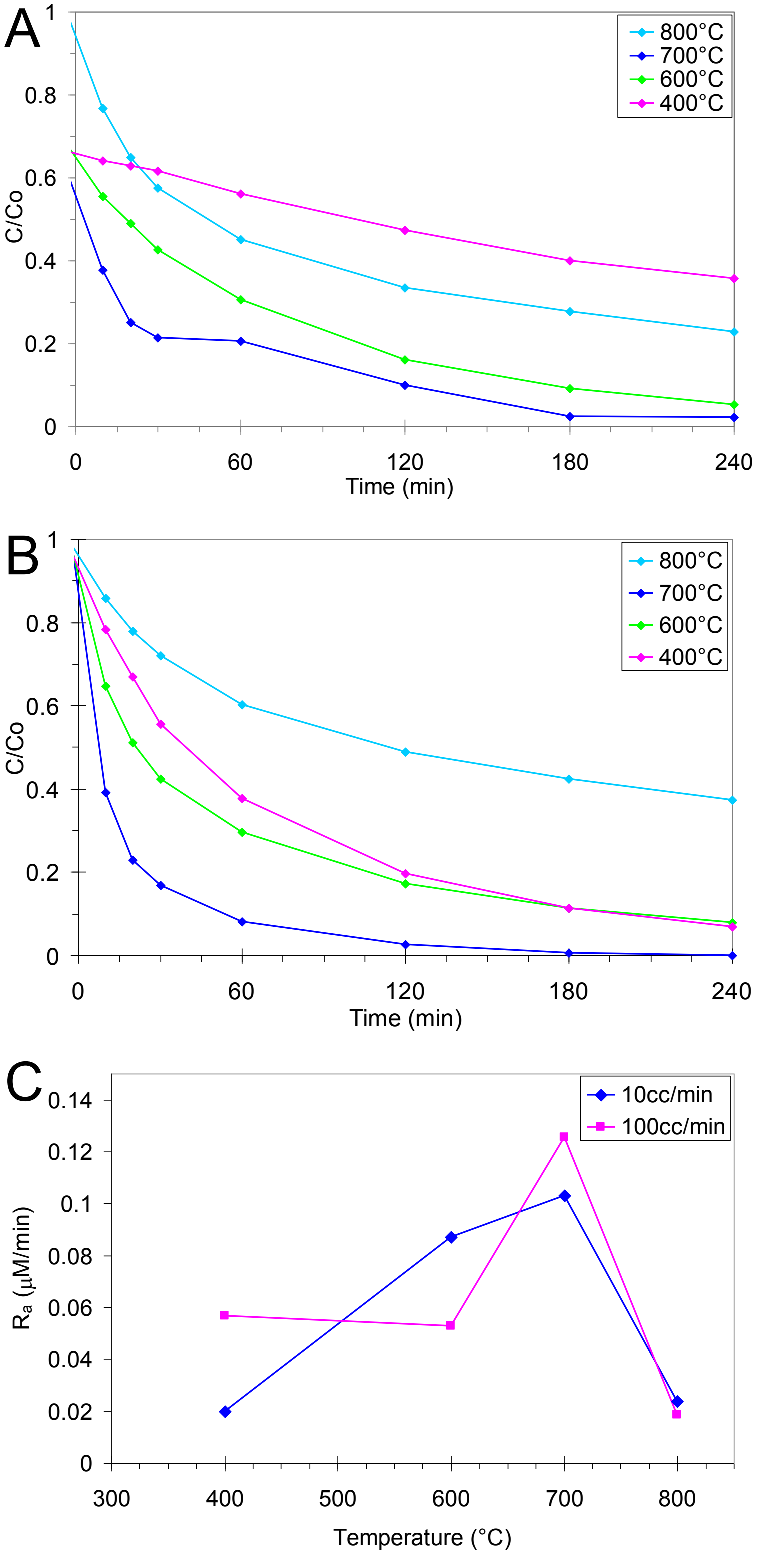
A
C/Co
0
0.2
0.4
0.6
0.8
1
0
60
120
180
240
Time (min)
800°C
700°C
600°C
400°C
B
C/Co
0
0.2
0.4
0.6
0.8
1
0
60
120
180
240
Time (min)
800°C
700°C
600°C
400°C
C
R_a (μM/min)
0
0.02
0.04
0.06
0.08
0.1
0.12
0.14
300
400
500
600
700
800
Temperature (°C)
10cc/min
100cc/min

Figure 32: Photocatalytic degradation of MB versus time. Reactions were performed using TiO_2 materials prepared by firing 150°C composites at A) $10cm^3/min$ and B) $100cm^3/min$ air flow suspended at pH = 7 (500mg/L TiO_2, $1mW/cm^2$ UV light intensity) and C) Initial degradation rate of MB versus temperature at air flow rate of $10cm^3/min$ and $100cm^3/min$ (lines drawn only as a guide).

The increasing performance observed between 400°C and 700°C was due to the increased crystallinity of the materials (Figure 26b) despite the significant loss of specific surface area (Figure 33). Despite increases in crystal size between 700°C and 800°C, a significant reduction in performance is observed, which is attributed to detrimental loss of specific surface area (Figure 33).

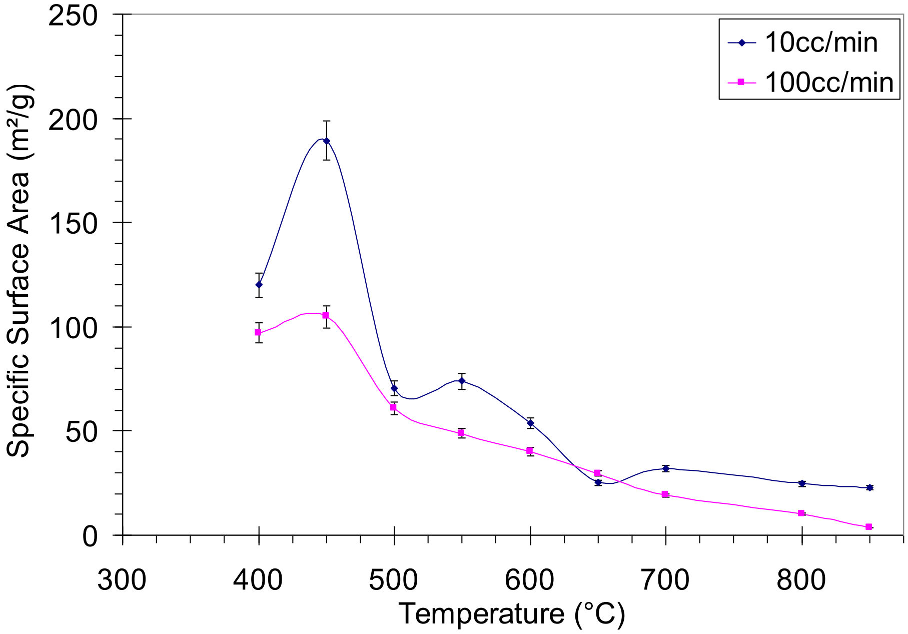

Figure 33: Specific surface area (as determined by low pressure 5-point BET adsorption) of composite materials initially prepared at 150°C and subsequently annealed in air.

Table 6: Percentage of organic removal by membrane materials fired at 700°C under both $10cm^3/min$ and $100cm^3/min$.

Time (min)	$10cm^3/min$	$100cm^3/min$
30	79%	83%
60	80%	92%
120	90%	97%
240	98%	100%

Based on pseudo-first-order reaction rate kinetic analysis, the initial reaction rate observed versus firing temperature at both air flow rates (i.e., $10cm^3/min$ and $100cm^3/min$) are illustrated in Figure 32c and the optimal firing temperature is 700°C due to the highest reaction rate observed. Degradation rates increased with increasing temperature for both air flow rates; however, the highest removal rate was observed using materials prepared at 700°C under $100cm^3/min$ air flow rate (Figure 32c and Table 6). The increased degradation rate using materials prepared under $100cm^3/min$ versus $10cm^3/min$ may be attributed to the presence of minute concentrations of rutile (not observable by XRD, detection limit of ~2-4 mass % and ~4% rutile is observed at 750°C). Several studies have reported enhanced photocatalytic performance with anatase-rutile mixtures due to a perceived synergistic mechanism between the anatase and rutile crystals [71, 90, 146, 157-159].

5.3.4 Effect of reduced processing temperature on crystal growth and phase transformation.

Anatase is a metastable phase of TiO_2, which is often the initial product formed from solution processing, due to a higher stability than rutile at crystal sizes less than 14nm [52, 59, 61, 62, 67, 68, 129]. X-Ray diffraction of unfired (i.e., green) composites prepared at 150°C revealed the presence of anatase [165]; however unfired composites prepared at 80°C revealed the presence of titanium hydroxide (corresponding to the broad peak at 23.2°) [167, 168] as well as the broad anatase (JCPDS # 01-084-1286) peak at 25.4° at all synthesis times (i.e., 15 minutes, 1, 2, and 12 hours) Figure 34. Increasing the synthesis time at 80°C did not appear to increase the crystallinity of the TiO_2 within composites due to apparent rapid gelation of the PVA and TiO_2/TiBALDH matrix, forming a stable composite within 15 minutes.

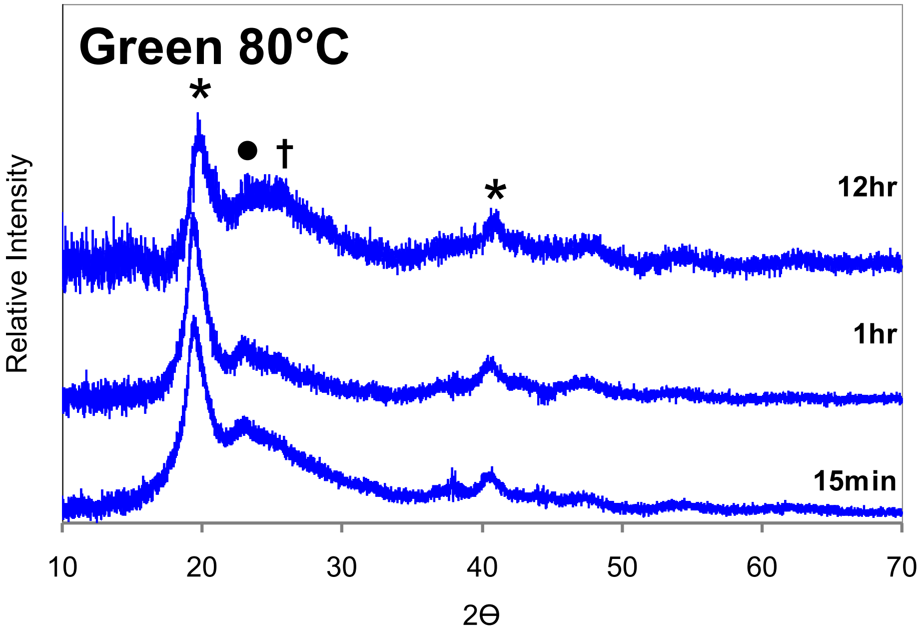

Figure 34: XRD patterns for the green composite materials synthesized at pH9 80°C for 15 minutes, 1 hour, and 12 hours; * denotes crystalline PVA peaks, • denotes broad amorphous peak, † denotes broad anatase peak.

X-Ray diffraction of composites post isochronal firing (1 hour plateau) revealed anatase (JCPDS # 01-084-1286) as the dominant phase. Transformation to rutile (JCPDS # 01-073-1765) was initially observed at 700°C (4.7±1.2% rutile) and increased to 36.5±2.0% rutile by 800°C (shown in Figure 35). Comparatively, the phase transformation from anatase to rutile in composites synthesized hydrothermally at 150°C, was not observed until 850°C (11.1±0.8% rutile). The size of anatase crystallites in materials prepared at 80°C following firing at 400°C was 6.0±0.9 nm and grew to 45.1±1.4 nm after firing at 800°C. Conversely, the size of anatase crystallites in materials prepared at 150°C following firing at 400°C was 23% smaller (ca. 4.6±1.5 nm), growing to 31.6±3.1 nm after firing at 800°C.

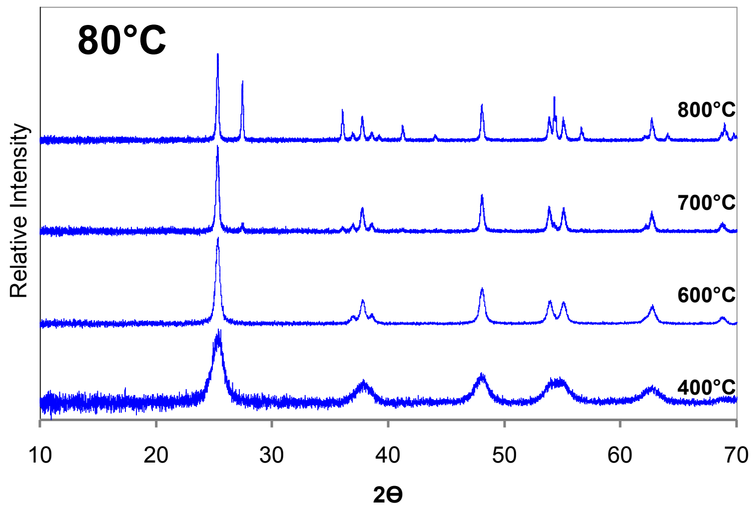
80°C
Relative Intensity
800°C
700°C
600°C
400°C
10
20
30
40
50
60
70
2Θ

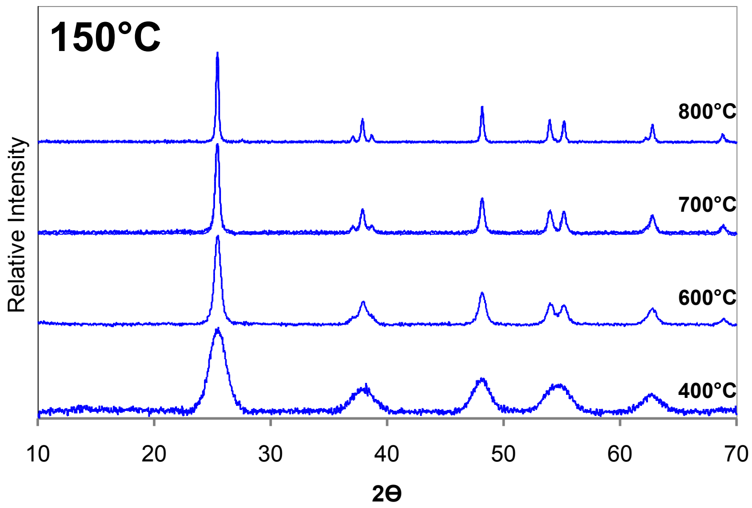
150°C
Relative Intensity
800°C
700°C
600°C
400°C
10
20
30
40
50
60
70
2Θ

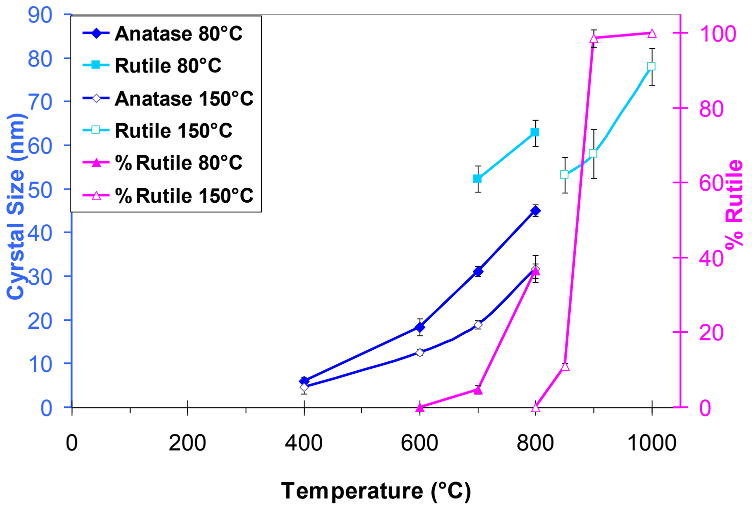
Anatase 80°C
Rutile 80°C
Anatase 150°C
Rutile 150°C
% Rutile 80°C
% Rutile 150°C
Cyrstal Size (nm)
90
80
70
60
50
40
30
20
10
0
% Rutile
100
80
60
40
20
0
0
200
400
600
800
1000
Temperature (°C)

Figure 35: XRD patterns for the isochronally fired composite materials synthesized at pH = 9 for 12 hours at 80°C (top); 150°C (middle); and (bottom) anatase and rutile crystallite sizes, percent rutile vs. annealing temperature.

The anatase crystal size upon first detection of rutile was 31.2 ± 1.2 nm (when initially synthesized at 80°C) and 31.6 ± 3.1 nm when initially synthesized at 150°C. However, samples initially prepared at 80°C exhibited more rapid anatase growth at lower temperatures (e.g., 150 % by 600°C and 180% by 700°C), as illustrated in Figure 35C. The anatase coarsening rate was observed to increase in the materials prepared at 80°C as compared to those prepared at 150°C, consequently reducing the temperature required to induce transformation to rutile (ca. 700°C versus 850°C). This increased coarsening is likely attributed to the presence of unreacted precursor and amorphous TiO_2 within the matrix, which provides nutrient for the growth of the crystals. Increasing the hydrothermal synthesis time from 15 minutes to 12 hours did not affect the size of the anatase crystallites. Elevated hydrothermal processing temperatures (such as 150°C) may have increased the rate of nucleation as observed by the decreased crystallite size (ca. 4.6 ± 1.5nm after 400°C). The decreased crystallite size is most likely due to the large number of nuclei formed, thus reducing the concentration of titanium species for growth of the initial nuclei.

TEM bright field micrographs of materials prepared at 80°C prior to firing and post firing are shown in Figure 36. In agreement with XRD mearsurements, green materials do not appear to be highly crystalline. Selected area electron diffraction exhibits diffuse rings, suggesting that the material is nanocrystalline TiO_2 within an amorphous organic matrix. Analysis of TEM micrographs in Figure 36 also confirms the observed crystallite size increase with firing temperature. SEM was also used to observe the grain growth within the materials after firing (Figure 37). By 800°C, rutile crystals were observed within materials prepared at all synthesis times. The size of the rutile crystals are approximately equivalent to those determined from XRD measurements.

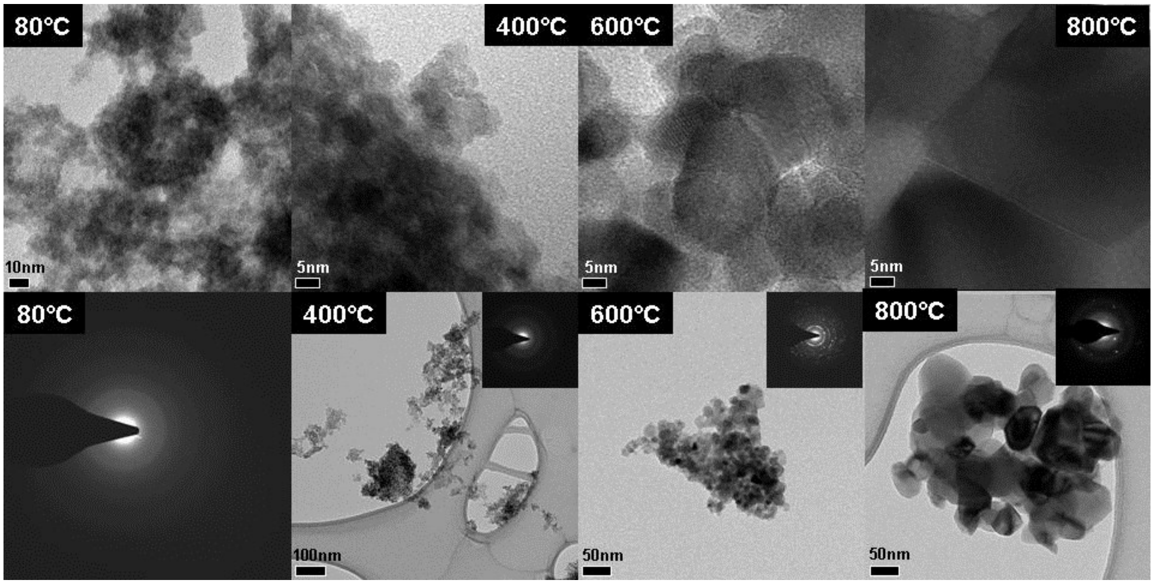

Figure 36: Transmission Electron Microscope micrographs of membrane materials initially prepared at 80°C for 12 hours and subsequently heated isochronally at 400°C, 600°C, 700°C, and 800°C for 1 hour.

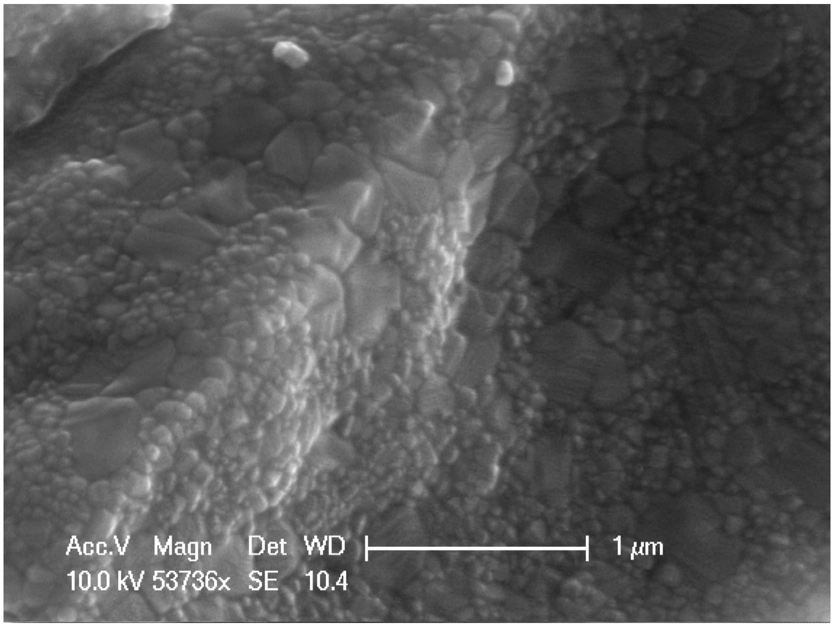

Figure 37: Representative Scanning Electron Microscope micrograph of a porous membrane initially prepared at 80°C for 1 hour and subsequently fired at 800°C for 1 hour.

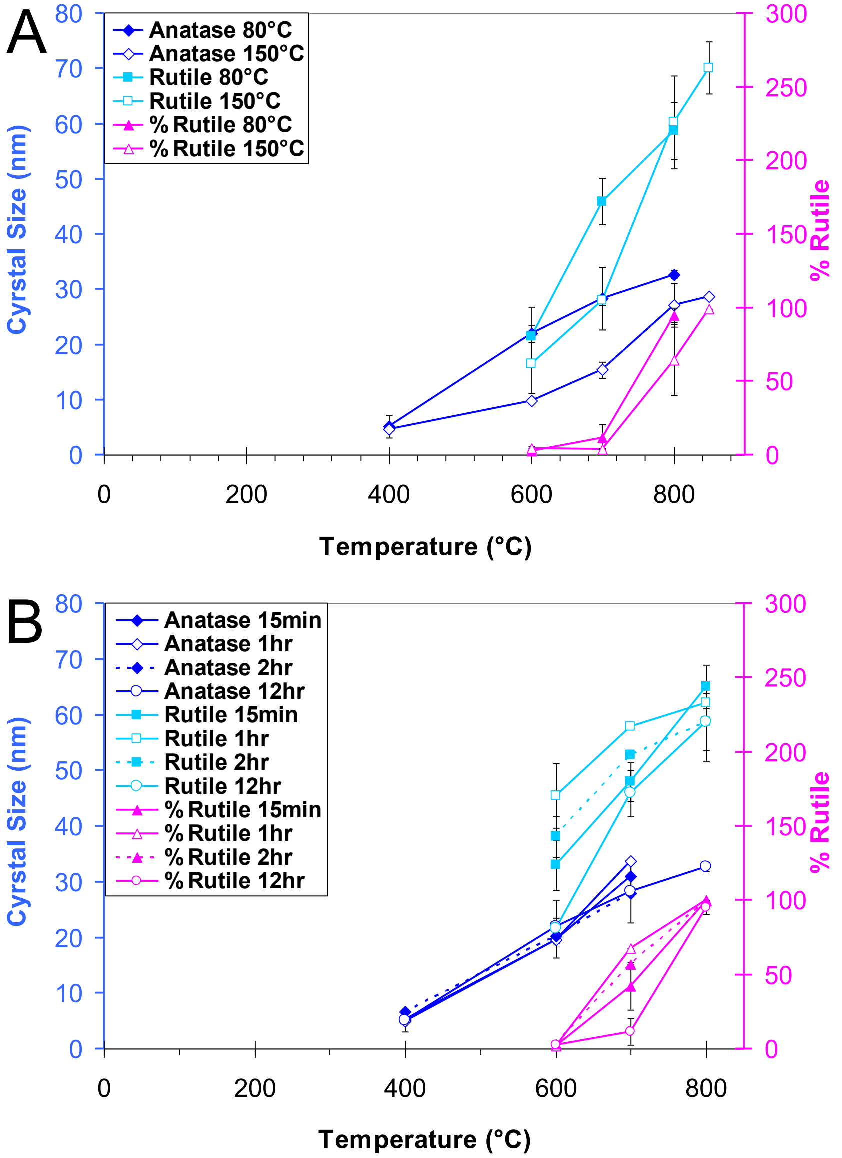

Figure 38: A) Anatase and Rutile crystal diameters and % Rutile vs. Temperature (as determined by XRD) for samples initially synthesized at pH = 9 at 80°C and 150°C for 12 hours without PVA and subsequently annealed at 400°C, 600°C, 700°C and 800°C for 1 hour. B) Anatase and Rutile crystal diameters and % Rutile vs. Temperature for samples prepared at 80°C for different synthesis durations: 15minutes, 1, 2, and 12 hours.

Similarly to TiO_2-PVA composites prepared at 80°C, TiO_2 powders prepared at 80°C exhibited more rapid coarsening versus those initially prepared at 150°C, which resulted in the onset of phase transformation to rutile at lower temperatures. Coarsening and transformation rates are strongly dependent on the initial degree of crystallinity and crystallite size[59]. However, the anatase crystal size observed at the onset of rutile formation for samples prepared at 80°C was 22.0 ± 1.6nm in contrast to those initially prepared at 150°C, which were at 31.2 ± 1.2nm (as seen Figure 35 and Figure 26, respectively) at the onset of rutile formation. Initial synthesis time did not affect the onset temperature for phase transformation to rutile. In fact, the anatase crystallite size was approximately 20nm for all synthesis times at 80°C. The presence of smaller anatase crystallites at the onset of rutile nucleation at the lower firing temperature of 600°C is indicative that the phase transformation to rutile was dominated by interface nucleation [69]. The rate of transformation via interfacial nucleation is dependent on the probability of contact of two anatase crystals, which is greatly diminished in the composite samples due to the presence of the polymer separating crystals [93, 166]. The presence of a PVA matrix and the low volume fraction of inorganic material within the composite reduces the number of interface nucleation sites, subsequently retarding the rate of phase transformation.

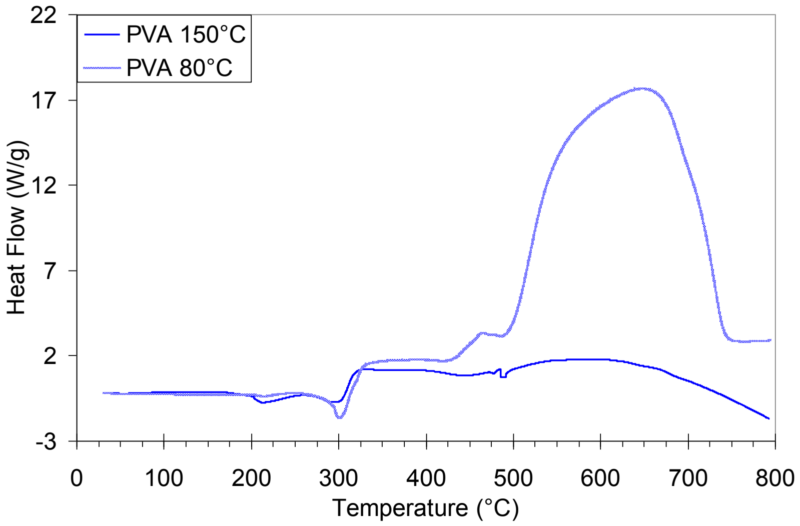

Figure 39: Differential Scanning Calorimetry of composites initially prepared at 80°C and 150°C and heated at 10°C/min to 800°C in argon flowing at 20cm^3/min.

The degree of crystallinity of the green materials was examined using differential scanning calorimetry (DSC). Three characteristic peaks were observed at 220°C, 300°C and 455°C in materials initially prepared at 80°C and 150°C. The endothermic peaks observed at 220°C are associated with the melting of PVA[169]. The heat of fusion increases with increasing degree of polymer crystallinity, which is measured by the area under the peak associated with the melting of PVA[169]. Analyses of these peaks indicate that the degree of PVA crystallinity after processing at 80°C is 21% of samples prepared at 150°C[169]. The second observed endothermic peak at 300°C is associated with the dehydroxylation of TiOH[170]. The larger peak from the sample prepared at 80°C indicates more dangling surface bonds and possibly the presence of more unreacted precursor (i.e., partially hydrolyzed or condensed Ti-OH species) trapped within the organic matrix [170].

This is consistent with the presence of the exothermic peak observed at 455°C in the sample prepared at 80°C, which is attributed to the heat of crystallization of amorphous TiO_2 to anatase [171-175]. The reduced synthesis temperature decreases the crystallinity of the polymer (by inhibiting polymer chains from untangling and aligning) and the TiO_2 as observed by the reduced heat of melting and the presence of the exothermic heat of crystallization. The smaller crystallites will have a greater rate of coarsening and will transform to rutile at a lower temperature, as observed in the samples initially prepared at 80°C. A large, broad exothermic peak observed in DSC that initiates at 500°C corresponds to grain growth of anatase and the initiation of anatase to rutile phase transformation, which is an irreversible exothermic reaction [170].

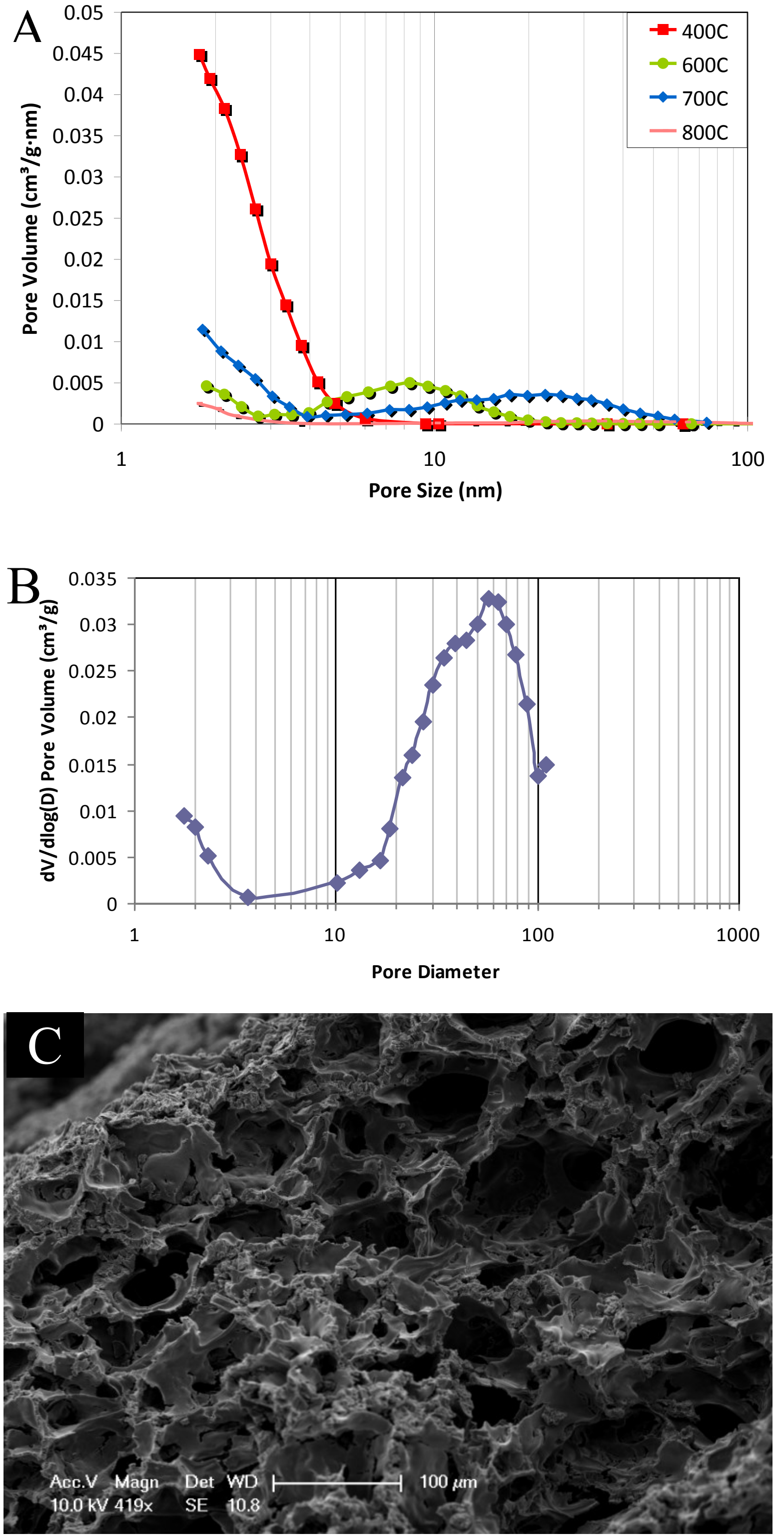
A
0.05
0.045
0.04
0.035
0.03
0.025
0.02
0.015
0.01
0.005
0
Pore Volume (cm³/g·nm)
1
10
100
Pore Size (nm)
400C
600C
700C
800C
B
0.035
0.03
0.025
0.02
0.015
0.01
0.005
0
dV/dlog(D) Pore Volume (cm³/g)
1
10
100
1000
Pore Diameter
C
Acc.V Magn Det WD
10.0 kV 419x SE 10.8
100 μm

Figure 40: (a) Pore size distribution of membrane materials, initially prepared at 80°C and annealed at different temperatures, (b) pore size distribution of the composite material initially prepared at 80°C and fired at 800°C for 1 hour, and (c) low resolution Scanning Electron micrograph of a membrane initially prepared at 80°C for 15 minutes, and fired at 800°C for 1 hour.

The pore size distribution within the porous membrane materials fired at 400°C for 1 hour is centered at 4 nm (Figure 40). Increasing the firing temperature increased the average pore size as well as shifted the pore size distribution to significantly larger pores. Analysis of low magnification SEM micrographs confirms the increased pore sizes and distributions as measured via N_2 adsorption (Figure 40b, C), which reveal a considerable range of pores sizes between 100 nm and 100 μm. Increased firing temperatures result in significant loss of surface area (80% of the surface area is lost between 400°C and 600°C) due to continued growth of the large pores and the formation of large rutile grains, eliminating small pores.

Table 7: Average surface area (as determined by low pressure 5-point BET adsorption) of composite materials initially prepared at 80°C and subsequently annealed in air.

	Surface Area (m^2/g)
400°C	166.2 ± 7.1
600°C	31.5 ± 4.1
700°C	40.2 ± 10.5
800°C	10.1 ± 4.7

Energy dispersive spectroscopy (EDS) mapping (Figure 41) highlights the broad pore size distributions, which are attributed to the heterogeneity of the polymeric matrix and titanium dioxide particle distribution within the green material. This type of pore structure promotes the development of even larger pores and the elimination of small pores[60]. As observed by XRD, there was no significant change in increased crystallinity by increasing the synthesis time. In addition, the heterogeneity of the composite (polymer and TiO_2 distribution) existed at short durations (ca. 15 minutes) and persisted after 12 hours, indicating that gelation was rapid. Thus, increasing initial synthesis time did not increase diffusion or mixing within the matrix, which would have improved homogeneity within the green composite. The large pockets of polymer that are removed upon burnout produced large pores that continued to grow since their size was significantly larger than the inorganic grains (>100nm pores versus 6.0 ± 0.9 nm anatase crystals). Thus, pores will continue to grow while the smaller pores will continue to shrink as is observed in the pore size distributions[60]. Despite the nucleation of large rutile crystals at 700°C, 52.3±3.0nm, the pores are still significantly larger (>1.5 X those of grains). Therefore, the pores will continue to increase in size further reducing the surface area [60]. This ultimately limits the control of porosity and reduces the surface area of the material.

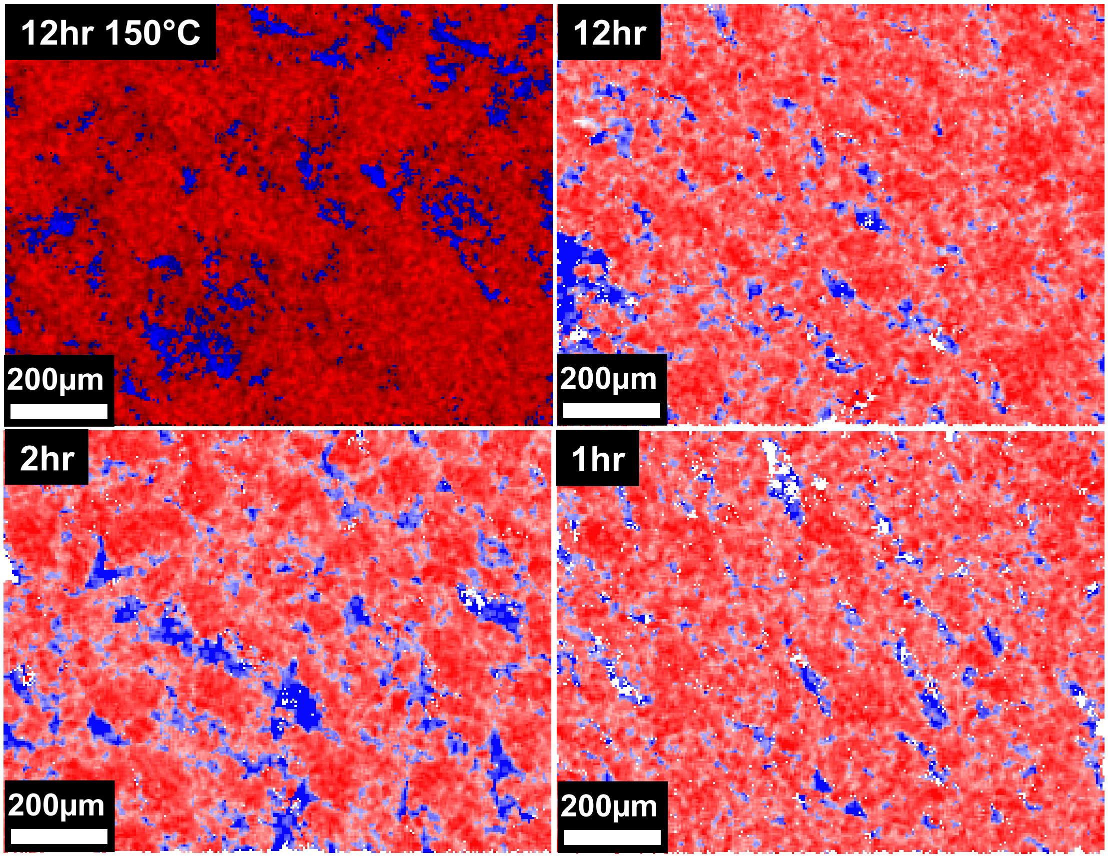

Figure 41: EDS maps of 1mm^2 area of green composites: Red-Carbon; Blue-Titanium

5.4 Conclusions.

The initial synthesis temperature (80°C vs 150°C) and air flow rate during firing greatly affect the resulting crystal growth and phase transformation within the porous ceramics. The crystal size and phase of TiO_2 ultimately impacts photocatalytic performance, thus it is crucial to understand and control grain growth and phase transformation behavior. The kinetic analysis of the grain growth and phase transformation within the porous TiO_2 revealed a step in the interfacial nucleation due to the increasing density of the highly porous material. As expected, the increasing air flow rate increases the probability of interface nucleation while increasing firing temperature increased the surface nucleation contribution to the phase transformation to rutile. Phase transformations were observed at lower firing temperatures in samples without polymer and the composites initially prepared at reduced temperatures. Rutile was initially observed at 700°C (4.7 ± 1.2% rutile) in samples prepared at 80°C (versus the 850°C onset temperature from samples initially prepared at 150°C). Interestingly, the anatase crystallite size at which rutile was first observed was 30 nm for both 80°C and 150°C initial processing conditions. The reduced temperature of initial phase transformation to rutile in the samples initially prepared at 80°C is likely attributed to the crystallization of amorphous TiO_2 remaining within the green material.

5.5 Acknowledgements.

This work was conducted with Government support under and awarded by DoD, Office of Naval Research, National Defense Science and Engineering Graduate (NDSEG) Fellowship, 32 CFR 168a.

Chapter 6.
Conclusions

The objective of this doctoral work was to investigate the fundamental nucleation and growth of TiO_2 used as a photocatalytic agent for the degradation of organic contaminants in water. Biology often uses organics (both structural and surface) to guide the nucleation and growth of minerals. In addition, minerals are formed under mild conditions (e.g., near neutral pH and low temperatures). This is exemplified in biomineralizing organisms such as the California Red Abalone, which uses aqueous-based mineral precursors that nucleate within an organic scaffold coated with chelating ligands. Based on inspiration from such organisms, TiBALDH was selected as the precursor due to the chelating organic ligands that afford stability at a near-neutral pH in an aqueous system. We selected PVA as the synthetic structural organic since it is hydrophilic and slightly acidic, similar to the structural organics observed in the biomineralizing organisms. The addition of the synthetic polymer during the hydrothermal synthesis of TiO_2 yields a TiO_2-organic composite that can be annealed to produce a bulk, porous membrane. This membrane will be implemented within a flow-through photocatalytic reactor, eliminating the need for downstream nanoparticle recovery systems, which are currently necessary in slurry-based reactors. This not only reduces capital and operational costs, but also expands the range of potential applications of such photocatalytic technologies. Due to increasing threats by emerging organic contaminants within our drinking water sources, we target residential and small business Point of Use (POU) applications (such as under-counter drinking water treatment systems) to supplement municipal water treatment processes. Currently 4 out of 10

Americans use POU treatment systems to remove such contaminants; however these systems do not degrade these emerging contaminants.

Chapter 2 discusses the fundamental nucleation and growth of TiO_2 using the water soluble and hydrolytically stable precursor, TiBALDH. The effect of pH and time were investigated and discussed from coordination chemistry and coarsening perspectives. The observed phase of TiO_2 formed at near neutral pH was pure rutile; conversely, at pHs greater than 10, only anatase TiO_2 was observed. Under both conditions (i.e., near neutral pH or pH >10), the phase developments were independent of reaction times. A mixture of anatase and rutile TiO_2 was formed at pH = 9, and is believed to enhance photocatalytic performance. Under this condition, the initial phase observed is anatase; however, with increasing reaction time, a phase transformation to rutile is observed. The resulting phase is dictated by the hydrolytic stability of the lactato ligands on the TiBALDH precursor. The Ti center is octahedrally coordinated with hydroxyl ligands coordinated along the z-axis and the bidentate lactato ligands within the x-y coordination plane. Due to the hydrolytic stability of the lactato ligands at pH = 7.8, condensation reactions were confined along the z-axis, resulting in octahedra with corner shared bonds (the predominant bonding configuration within the rutile structure). At pH conditions greater than 10, the lactato ligands are rapidly hydrolyzed, enabling condensation reactions to occur at both edges and corners. Thus, anatase can form due to its high concentration of edge sharing bonds (50%). The subsequent crystal growth was also dictated by reaction pH. At the lower pH conditions (i.e., pH = 7.8 and 9), the primary grain growth mechanism observed was oriented attachment. This is due to the lower solubility product of TiO_2. Interestingly, this oriented attachment-based growth of TiO_2 at pH = 9 resulted in the phase transformation of anatase to rutile. Under more basic conditions (i.e., pH = 10 and 11), the solubility product of TiO_2 is significantly higher (two orders of magnitude greater at pH = 11 versus pH = 9). Thus, Ostwald Ripening, growth of large crystals at the expense of smaller crystals, was observed to be the dominant grain growth mechanism. This resulted in an increased crystal size distribution with longer synthesis times.

In Chapter 3, we investigate the performance of photocatalytic TiO_2 with mixed phase (i.e., anatase and rutile). The photocatalytic characterization, performed at pH = 4, 7, and 10 revealed the activity was dependent on both particle-particle interactions and sobate-surface interactions. Under acidic conditions, the positively charged surface repels the positively charged dye molecules. This resulted in a hindered performance due to increase diffusion path and short lifetime of radicals. At pH = 7, the slightly negatively charged surface attracts the positively charged dye molecules, enhancing photocatalytic performance due to close proximity of analyte to the catalyst surface and improving the probability of degradation by radicals. Suspensions tested at pH = 10, displayed a reduced performance relative to those at pH = 7. This was due to a significantly increase of dye adsorption onto the catalyst surface. Therefore, suspensions at pH = 7 were ideal for investigation of phase effects on photocatalytic performance. The optimal ratio of anatase to rutile in photocatalytic performance was 80% anatase / 20% rutile. Under these conditions, 91% of the analyte was removed within 120 minutes. The optimal performance of the catalyst is attributed to the synergistic charge transfer of holes from rutile to anatase. This was confirmed by the photoreduction of a platinum (IV) complex to platinum (0), which subsequently deposited onto the catalyst surface as platinum metal, revealing the location of electron generation.

Chapter 4 revealed the impact of the addition of a synthetic polymer (PVA) on the nucleation and growth of the TiO_2. The presence of low concentrations of polymer reduced the rate of phase transformation of anatase to rutile. This was due to the adsorption of polymer on the crystal surfaces, which subsequently inhibited oriented attachment of anatase crystallites onto rutile crystals. High concentrations of polymer completely inhibited the formation and subsequent phase transformation of anatase to rutile. However, the high concentration of polymer resulted in the formation of a viscoelastic composite, which formed via crosslinking of the hydrolyzed precursor and/or the hydrolyzed nanoparticles with the hydrophilic polymer. XRD and TEM analysis of as-synthesized composites revealed 2nm anatase crystals embedded within the organic matrix. Subsequent firing removed the polymer matrix to yield a porous photocatalytic membrane with high surface area for use as a flow-through POU reactor. This firing also resulted in the grain growth of anatase crystals and eventual phase transformation to rutile (at 800°C).

Chapter 5 evaluates the effects of composite processing parameters on the resulting material properties. The effects of firing temperature, air flow rate during firing, firing time, and composite synthesis temperatures were considered. Higher firing temperatures increased crystal size; however, reduced composite synthesis temperatures and increased airflow during firing were observed to increase anatase crystal sizes. The anatase crystal size effected the phase transformation to rutile, which effects photocatalytic activity (Chapter 3). Air flow rate was observed to have a significant effect on the resulting porosity of the TiO_2 membrane since the synthetic polymer (binder) is removed by combustion. Increasing the air flow rate resulted in a larger fraction of organic removed at lower temperatures. This resulted in a more rapid transformation to rutile. Annealing experiments were performed to identify which of the phase transformation mechanisms dominated: interface, surface, or bulk nucleation. These mechanisms were observed to not only be temperature dependent, but also density dependent (due to the low loading of TiO_2 within the composite). Firing resulted in removal of micropores, which lead to increased anatase-anatase interactions and a greater rate of transformation to rutile. Firing conditions were selected to form materials used in photocatalytic degradation reactions. Increasing the anatase crystal size appeared to improve photocatalytic performance and the increased air flow rate also was observed to increase photocatalytic degradation. After 240 minutes, 93%, 92%, 100%, and 56%, of methylene blue was removed by the porous membranes fired at 400°C, 600°C, 700°C, and 800°C at $100cm^3$/min air flow rate, respectfully. The material with optimal performance (i.e., 700°C at $100cm^3$/min air flow rate) removed 83% of MB within 30 minutes. Reduction in processing temperature (composite synthesis temperature) was observed to reduce the subsequent firing temperatures required to achieve the initial phase transformation to rutile due to an increased presence of amorphous TiO_2 within the composite. The onset temperature of rutile for samples initially synthesized at 80°C was observed at 700°C (4.7±1.2% rutile, increasing to 36.5±2.0% rutile by 800°C). Samples initially prepared at 150°C did not form rutile until 850°C.

We have demonstrated control of TiO_2 crystal size, phase, and porosity using a low temperature, environmentally benign process. The addition of an exogenous organic (i.e., synthetic polymer) under the same reaction conditions produces a stable viscoelastic material that can be molded or cut into any desired size and shape to act as a stand-alone porous, photocatalytically active membrane [84, 85]. The objective was to develop a membrane for use in a POU reactor for residential or small business applications (such as under counter). However, several challenges need to be met to implement and optimize this membrane. In order to be implemented into a flow through reactor, the membrane must withstand the water pressure in the system. In addition, the membrane must maintain a sufficient porosity to maximize the photocatalytic activity via accessible surface area and minimize the backpressure induced by flow across the membrane. Following optimization, the membrane needs to be incorporated into a point of use prototyped system to demonstrate its utility.

This doctoral work has clearly demonstrated the fundamental mechanism of nucleation and growth of TiO_2 as well as phase transformations within a TiO_2-polymer composite, yielding a photocatalytically active membrane. These results have implications in the development and implementation of new photocatalytic technologies and broadens the range of these technologies to POU, which otherwise would not be feasible. This technological development is significant since it will reduce the potential release and exposure of nanoparticles into the environment, which may also be hazardous. Finally, this study supports the concept of a systematic development of new materials from a fundamental understanding of their nucleation and growth to utility in practical applications. With increasing awareness of water conservation and protection, and the increasing need for more drinking water, this technology may be able to play a role in increasing sustainability and reduce public health and safety concerns.

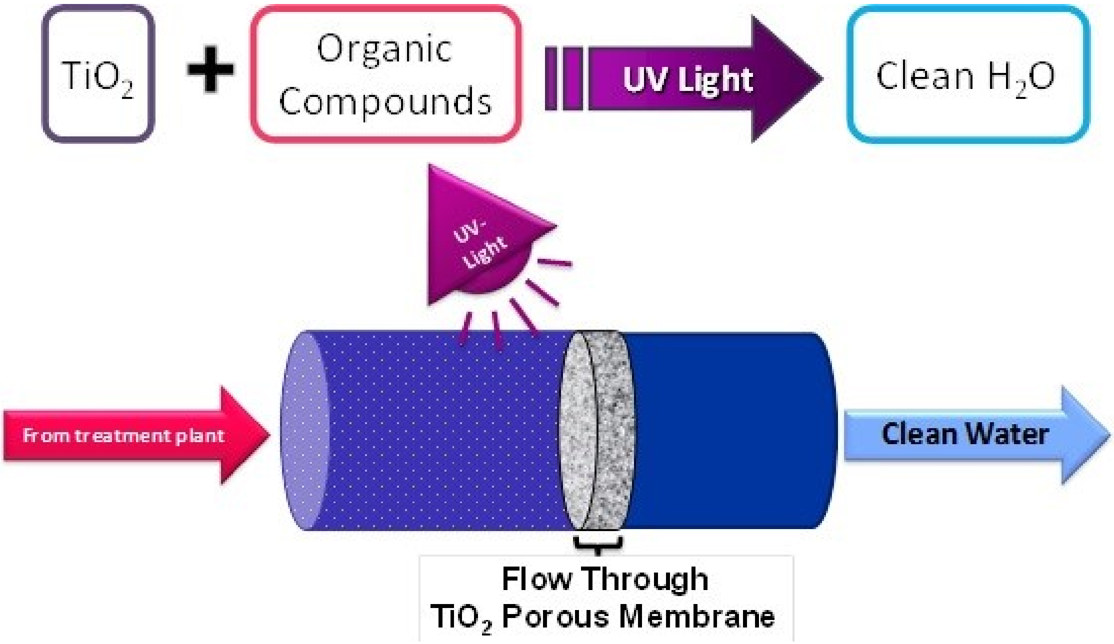

Figure 42: Future POU application of this membrane technology.

Chapter 7.
References

1. Bolong, N.; Ismail, A. F.; Salim, M. R.; Matsuura, T., A review of the effects of emerging contaminants in wastewater and options for their removal. *Desalination* **2009,** *239* (1-3), 229-246.
2. Snyder, S. A.; Westerhoff, P.; Yoon, Y.; Sedlak, D. L., Pharmaceuticals, personal care products, and endocrine disruptors in water: Implications for the water industry. *Environmental Engineering Science* **2003,** *20* (5), 449-469.
3. Resources, C. D. o. W., The California Water Plan Update 2009 - Administrative Draft. In *Bulletin 160-09 Department of Water Resources*, 2009; Vol. Highlights.
4. Diamanti-Kandarakis, E.; Bourguignon, J.-P.; Giudice, L. C.; Hauser, R.; Prins, G. S.; Soto, A. M.; Zoeller, R. T.; Gore, A. C., Endocrine-Disrupting Chemicals: An Endocrine Society Scientific Statement. *Endocrine Reviews* **2009,** *30* (4), 293-342.
5. Khetan, S. K.; Collins, T. J., Human pharmaceuticals in the aquatic environment: A challenge to green chemistry. *Chemical Reviews* **2007,** *107* (6), 2319-2364.
6. Stackelberg, P. E.; Furlong, E. T.; Meyer, M. T.; Zaugg, S. D.; Henderson, A. K.; Reissman, D. B., Persistence of pharmaceutical compounds and other organic wastewater contaminants in a conventional drinking-water-treatment plant. *Science of the Total Environment* **2004,** *329* (1-3), 99-113.
7. Pomati, F.; Castiglioni, S.; Zuccato, E.; Fanelli, R.; Vigetti, D.; Rossetti, C.; Calamari, D., Effects of a Complex Mixture of Therapeutic Drugs at Environmental Levels on Human Embryonic Cells. *Environmental Science & Technology* **2006,** *40* (7), 2442-2447.

8. Draper, A. J.; Jenkins, M. W.; Kirby, K. W.; Lund, J. R.; Howitt, R. E., Economic-engineering optimization for California water management. *Journal of Water Resources Planning and Management-Asce* **2003,** *129* (3), 155-164.

9. Newlin, B. D.; Jenkins, M. W.; Lund, J. R.; Howitt, R. E., Southern California water markets: Potential and limitations. *Journal of Water Resources Planning and Management-Asce* **2002,** *128* (1), 21-32.

10. Howitt, R. E., Empirical analysis of water market institutions: The 1991 California water market. *Resource and Energy Economics* **1994,** *16* (4), 357-371.

11. Resources), D. C. D. o. W., The California Water Plan Update 2009 - Administrative Draft. *Bulletin 160-09 Department of Water Resources* **2009,** *Highlights*.

12. Anderson, J., The environmental benefits of water recycling and reuse. *Water Scince and Technology: Water Supply* **2003,** *3* (4), 1-10.

13. Gleick, P. H., WATER IN CRISIS: PATHS TO SUSTAINABLE WATER USE. *Ecological Applications* **1998,** *8* (3), 571-579.

14. Leenheer, J. A.; Rostad, C. E.; Barber, L. B.; Schroeder, R. A.; Anders, R.; Davisson, M. L., Nature and Chlorine Reactivity of Organic Constituents from Reclaimed Water in Groundwater, Los Angeles County, California. *Environmental Science & Technology* **2001,** *35* (19), 3869-3876.

15. Roberts, P. H.; Thomas, K. V., The occurrence of selected pharmaceuticals in wastewater effluent and surface waters of the lower Tyne catchment. *Science of the Total Environment* **2006,** *356* (1-3), 143-153.

16. Buerge, I. J.; Buser, H. R.; Poiger, T.; Muller, M. D., Occurrence and fate of the cytostatic drugs cyclophosphamide and ifosfamide in wastewater and surface waters. *Environmental Science & Technology* **2006,** *40* (23), 7242-7250.

17. Carballa, M.; Omil, F.; Lema, J. M.; Llompart, M.; García-Jares, C.; Rodríguez, I.; Gómez, M.; Ternes, T., Behavior of pharmaceuticals, cosmetics and hormones in a sewage treatment plant. *Water Research* **2004,** *38* (12), 2918-2926.

18. Boyd, G. R.; Reemtsma, H.; Grimm, D. A.; Mitra, S., Pharmaceuticals and personal care products (PPCPs) in surface and treated waters of Louisiana, USA and Ontario, Canada. *The Science of The Total Environment* **2003,** *311* (1-3), 135-149.

19. Stackelberg, P. E.; Furlong, E. T.; Meyer, M. T.; Zaugg, S. D.; Henderson, A. K.; Reissman, D. B., Persistence of pharmaceutical compounds and other organic wastewater contaminants in a conventional drinking-water-treatment plant. *Science of the Total Environment* **2004,** *329* (1-3), 99-113.

20. Tchobanoglous, G.; Schroeder, E. E., *Water quality: Characteristics, modeling, modification*. 1985; p Medium: X; Size: Pages: 704.

21. Dalrymple, O. K.; Yeh, D. H.; Trotz, M. A., Removing pharmaceuticals and endocrine-disrupting compounds from wastewater by photocatalysis. *Journal of Chemical Technology and Biotechnology* **2007,** *82* (2), 121-134.

22. Falconer, I. R.; Chapman, H. F.; Moore, M. R.; Ranmuthugala, G., Endocrine-disrupting compounds: A review of their challenge to sustainable and safe water supply and water reuse. *Environmental Toxicology* **2006,** *21* (2), 181-191.

23. Petrovic, M.; Eljarrat, E.; de Alda, M. J. L.; Barcelo, D., Endocrine disrupting compounds and other emerging contaminants in the environment: A survey on new monitoring strategies and occurrence data. *Analytical and Bioanalytical Chemistry* **2004,** *378* (3), 549-562.

24. Westerhoff, P.; Yoon, Y.; Snyder, S.; Wert, E., Fate of Endocrine-Disruptor, Pharmaceutical, and Personal Care Product Chemicals during Simulated Drinking Water Treatment Processes. *Environmental Science & Technology* **2005,** *39* (17), 6649-6663.

25. Das, D. P.; Baliarsingh, N.; Parida, K. M., Photocatalytic decolorisation of methylene blue (MB) over titania pillared zirconium phosphate (ZrP) and titanium phosphate (TiP) under solar radiation. *Journal of Molecular Catalysis A: Chemical* **2007,** *261* (2), 254-261.

26. Li Puma, G.; Puddu, V.; Tsang, H. K.; Gora, A.; Toepfer, B., Photocatalytic oxidation of multicomponent mixtures of estrogens (estrone (E1), 17[beta]-estradiol (E2), 17[alpha]-ethynylestradiol (EE2) and estriol (E3)) under UVA and UVC radiation: Photon absorption, quantum yields and rate constants independent of photon absorption. *Applied Catalysis B: Environmental* **2010,** *99* (3-4), 388-397.

27. Richardson, S. D.; Thruston, A. D.; Collette, T. W.; Patterson, K. S.; Lykins, B. W.; Ireland, J. C., Identification of TiO2/UV disinfection byproducts in drinking water. *Environmental Science & Technology* **1996,** *30* (11), 3327-3334.

28. Vione, D.; Maddigapu, P. R.; De Laurentiis, E.; Minella, M.; Pazzi, M.; Maurino, V.; Minero, C.; Kouras, S.; Richard, C., Modelling the photochemical fate of ibuprofen in surface waters. *Water Research* **2011,** *45* (20), 6725-6736.

29. Mendez-Arriaga, F.; Esplugas, S.; Gimenez, J., Degradation of the emerging contaminant ibuprofen in water by photo-Fenton. *Water Research* **2010,** *44* (2), 589-595.

30. Gregory, J., *Particles in Water: Properties and Processes*. CRC PressTaylor & Francis Group: Boca Raton, 2006.

31. Ridgway, H. F.; Kelly, A.; Justice, C.; Olson, B. H., Microbial fouling of reverse-osmosis membranes used in advanced wastewater treatment technology: chemical, bacteriological, and ultrastructural analyses. *Applied and Environmental Microbiology* **1983,** *45* (3), 1066-1084.

32. Water Health Series: Filtration Facts. Agency, E. P., Ed. Washington DC, 2005.

33. Lambourne, R.; Strivens, T. A., Paint and Surface Coatings - Theory and Practice (2nd Edition). Woodhead Publishing: 1999.

34. Carp, O.; Huisman, C. L.; Reller, A., Photoinduced reactivity of titanium dioxide. *Progress in Solid State Chemistry* **2004,** *32* (1-2), 33-177.

35. Goodeve, C.; Kitchener, J., Photosensitisation by titanium dioxide. *Transactions of the Faraday Society* **1938,** *34*, 570-579.

36. Goodeve, C.; Kitchener, J., The mechanism of photosensitisation by solids. *Transactions of the Faraday Society* **1938,** *34*, 902-908.

37. Serpone, N.; Pelizzetti, E., *Photocatalysis : fundamentals and applications*. Wiley: New York [etc.], 1989.

38. Fujishima, A.; Zhang, X. T.; Tryk, D. A., TiO2 photocatalysis and related surface phenomena. *Surface Science Reports* **2008,** *63* (12), 515-582.

39. Fujishima, A.; Honda, K., Electrochemical Photolysis of Water at a Semiconductor Electrode. *Nature* **1972,** *238* (5358), 37.

40. Gupta, S.; Tripathi, M., A review of TiO2 nanoparticles. *Chinese Science Bulletin* **2011,** *56* (16), 1639-1657.

41. Hufschmidt, D.; Liu, L.; Selzer, V.; Bahnemann, D., Photocatalytic water treatment: fundamental knowledge required for its practical application. *Water science and technology: a journal of the International Association on Water Pollution Research* **2004,** *49* (4), 135.

42. Robert, D.; Malato, S., Solar photocatalysis: a clean process for water detoxification. *Science of the Total Environment* **2002,** *291* (1-3), 85-97.

43. Gaya, U. I.; Abdullah, A. H., Heterogeneous photocatalytic degradation of organic contaminants over titanium dioxide: A review of fundamentals, progress and problems. *Journal of Photochemistry and Photobiology C-Photochemistry Reviews* **2008,** *9* (1), 1-12.

44. Saien, J.; Soleymani, A. R., Degradation and mineralization of Direct Blue 71 in a circulating upflow reactor by UV/TiO2 process and employing a new method in kinetic study. *Journal of Hazardous materials* **2007,** *144* (1-2), 506-512.

45. Linsebigler, A. L.; Lu, G.; Yates, J. T., Photocatalysis on TiO2 Surfaces: Principles, Mechanisms, and Selected Results. *Chemical Reviews* **1995,** *95* (3), 735-758.

46. Mansilla, H. D.; Bravo, C.; Ferreyra, R.; Litter, M. I.; Jardim, W. F.; Lizama, C.; Freer, J.; Fernandez, J., Photocatalytic EDTA degradation on suspended and immobilized TiO2. *Journal of Photochemistry and Photobiology a-Chemistry* **2006,** *181* (2-3), 188-194.

47. Poole, A. J., Treatment of biorefractory organic compounds in wool scour effluent by hydroxyl radical oxidation. *Water Research* **2004,** *38* (14-15), 3458-3464.

48. Linsebigler, A. L.; Lu, G. Q.; Yates, J. T., Photocatalysis on Tio2 Surfaces - Principles, Mechanisms, and Selected Results. *Chemical Reviews* **1995,** *95* (3), 735-758.

49. Wei, L.; Shifu, C.; Wei, Z.; Sujuan, Z., Titanium dioxide mediated photocatalytic degradation of methamidophos in aqueous phase. *Journal of Hazardous materials* **2009,** *164* (1), 154-160.

50. Ollis, D. F. In *Photocatalytic purification and remediation of contaminated air and water*, Editions Scientifiques Medicales Elsevier: 2000; pp 405-411.

51. Chen, J. S.; Liu, M. C.; Zhang, J. D.; Ying, X. Y.; Jin, L. T., Photocatalytic degradation of organic wastes by electrochemically assisted TiO2 photocatalytic system. *Journal of Environmental Management* **2004,** *70* (1), 43-47.

52. Barnard, A. S.; Zapol, P., Effects of particle morphology and surface hydrogenation on the phase stability of Ti O2. *Physical Review B* **2004,** *70* (23), 235403.

53. Cheng, H. M.; Ma, J. M.; Zhao, Z. G.; Qi, L. M., Hydrothermal Preparation of Uniform Nanosize Rutile and Anatase Particles. *Chemistry of Materials* **1995,** *7* (4), 663-671.

54. Diebold, U., The surface science of titanium dioxide. *Surface Science Reports* **2003,** *48* (5-8), 53-229.

55. Mendez-Arriaga, F.; Esplugas, S.; Gimenez, J., Photocatalytic degradation of non-steroidal anti-inflammatory drugs with TiO2 and simulated solar irradiation. *Water Research* **2008,** *42* (3), 585-594.

56. Ohno, T.; Sarukawa, K.; Tokieda, K.; Matsumura, M., Morphology of a TiO2 Photocatalyst (Degussa, P-25) Consisting of Anatase and Rutile Crystalline Phases. *Journal of Catalysis* **2001,** *203* (1), 82-86.

57. Datye, A. K.; Riegel, G.; Bolton, J. R.; Huang, M.; Prairie, M. R., Microstructural Characterization of a Fumed Titanium Dioxide Photocatalyst. *Journal of Solid State Chemistry* **1995,** *115* (1), 236-239.

58. Averback, R. S.; Höfler, H. J.; Hahn, H.; Logas, J. C., Sintering and grain growth in nanocrystalline ceramics. *Nanostructured Materials* **1992,** *1* (2), 173-178.

59. Gribb, A. A.; Banfield, J. F., Particle size effects on transformation kinetics and phase stability in nanocrystalline TiO2. *American Mineralogist* **1997,** *82* (7-8), 717-728.

60. Mayo, M. J.; Hague, D. C., Porosity-grain growth relationships in the sintering of nanocrystalline ceramics. *Nanostructured Materials* **1993,** *3* (1-6), 43-52.

61. Zhang, H.; Banfield, J. F., Size Dependence of the Kinetic Rate Constant for Phase Transformation in TiO2 Nanoparticles. *Chemistry of Materials* **2005,** *17* (13), 3421-3425.

62. Zhang, H. Z.; Banfield, J. F., Thermodynamic analysis of phase stability of nanocrystalline titania. *Journal of Materials Chemistry* **1998,** *8* (9), 2073-2076.

63. Introduction. In *Ceramic Materials*, Springer New York: 2007; pp 3-14.

64. Li Puma, G.; Brucato, A., Dimensionless analysis of slurry photocatalytic reactors using two-flux and six-flux radiation absorption-scattering models. *Catalysis Today* **2007,** *122* (1-2), 78-90.

65. Reh, H.; Händle, F., Current Classification of Ceramic Materials
Extrusion in Ceramics. Springer Berlin Heidelberg: 2007; pp 35-57.

66. Weir, A.; Westerhoff, P.; Fabricius, L.; Hristovski, K.; von Goetz, N., Titanium Dioxide Nanoparticles in Food and Personal Care Products. *Environmental Science & Technology* **2012,** *46* (4), 2242-2250.

67. Marinescu, C.; Sofronia, A.; Rusti, C.; Piticescu, R.; Badilita, V.; Vasile, E.; Baies, R.; Tanasescu, S., DSC investigation of nanocrystalline TiO2 powder. *Journal of Thermal Analysis and Calorimetry* **2011,** *103* (1), 49-57.

68. Zhang, H.; F. Banfield, J., Thermodynamic analysis of phase stability of nanocrystalline titania. *Journal of Materials Chemistry* **1998,** *8* (9), 2073-2076.

69. Zhang, H. Z.; Banfield, J. F., Phase transformation of nanocrystalline anatase-to-rutile via combined interface and surface nucleation. *Journal of Materials Research* **2000,** *15* (2), 437-448.

70. Lei, S.; Weng, D., Highly active mixed-phase TiO2 photocatalysts fabricated at low temperature and the correlation between phase composition and photocatalytic activity. *Journal of Environmental Sciences-China* **2008,** *20* (10), 1263-1267.

71. Ohno, T.; Tokieda, K.; Higashida, S.; Matsumura, M., Synergism between rutile and anatase TiO2 particles in photocatalytic oxidation of naphthalene. *Applied Catalysis a-General* **2003,** *244* (2), 383-391.

72. Reyes, C.; Fernandez, J.; Freer, J.; Mondaca, M. A.; Zaror, C.; Malato, S.; Mansilla, H. D., Degradation and inactivation of tetracycline by TiO2 photocatalysis. *Journal of Photochemistry and Photobiology a-Chemistry* **2006,** *184* (1-2), 141-146.

73. van Grieken, R.; Marugán, J.; Sordo, C.; Pablos, C., Comparison of the photocatalytic disinfection of E. coli suspensions in slurry, wall and fixed-bed reactors. *Catalysis Today* **2009,** *144* (1-2), 48-54.

74. Long, T. C.; Saleh, N.; Tilton, R. D.; Lowry, G. V.; Veronesi, B., Titanium Dioxide (P25) Produces Reactive Oxygen Species in Immortalized Brain Microglia (BV2): Implications for Nanoparticle Neurotoxicity&#x2020. *Environmental Science & Technology* **2006,** *40* (14), 4346-4352.

75. Desset, S.; Spalla, O.; Cabane, B., Redispersion of Alumina Particles in Water. *Langmuir* **2000,** *16* (26), 10495-10508.

76. Chowdhury, I.; Cwiertny, D. M.; Walker, S. L., Combined Factors Influencing the Aggregation and Deposition of nano-TiO2 in the Presence of Humic Acid and Bacteria. *Environmental Science & Technology* **2012,** *46* (13), 6968-6976.

77. Chen, X.; Mao, S. S., Titanium Dioxide Nanomaterials: Synthesis, Properties, Modifications, and Applications. *Chemical Reviews* **2007,** *107* (7), 2891-2959.

78. Park, J.-H.; Sudarshan, T., *Chemical vapor deposition*. ASM International: 2001; Vol. 2.

79. Bickmore, C. R.; Waldner, K. F.; Baranwal, R.; Hinklin, T.; Treadwell, D. R.; Laine, R. M., Ultrafine titania by flame spray pyrolysis of a titanatrane complex. *Journal of the European Ceramic Society* **1998,** *18* (4), 287-297.

80. Shin, Y.; Exarhos, G. J., Template synthesis of porous titania using cellulose nanocrystals. *Materials Letters* **2007,** *61* (11-12), 2594-2597.

81. Chang, H.; Kim, S. J.; Jang, H. D.; Choi, J. W., Synthetic routes for titania nanoparticles in the flame spray pyrolysis. *Colloids and Surfaces A: Physicochemical and Engineering Aspects* **2008,** *313*, 282-287.

82. Suchanek, W. L.; Riman, R. E., Hydrothermal synthesis of advanced ceramic powders. *Advances in Science and Technology* **2006,** *45*, 184-193.

83. Rao, C. N. R.; Ramakrishna Matte, H. S. S.; Voggu, R.; Govindaraj, A., Recent progress in the synthesis of inorganic nanoparticles. *Dalton Transactions* **2012,** *41* (17), 5089-5120.

84. Kinsinger, N. M.; Wong, A.; Li, D.; Villalobos, F.; Kisailus, D., Nucleation and Crystal Growth of Nanocrystalline Anatase and Rutile Phase TiO2 from a Water-Soluble Precursor. *Crystal Growth & Design* **2010,** *10* (12), 5254-5261.

85. Kinsinger, N.; Tantuccio, A.; Sun, M. W.; Yan, Y. S.; Kisailus, D., Photocatalytic Titanium Dioxide Composite. *Journal of Nanoscience and Nanotechnology* **2011,** *11* (8), 7015-7021.

86. Chae, S. Y.; Park, M. K.; Lee, S. K.; Kim, T. Y.; Kim, S. K.; Lee, W. I., Preparation of size-controlled TiO2 nanoparticles and derivation of optically transparent photocatalytic films. *Chemistry of Materials* **2003,** *15* (17), 3326-3331.

87. Andersson, M.; Osterlund, L.; Ljungstrom, S.; Palmqvist, A., Preparation of nanosize anatase and rutile TiO2 by hydrothermal treatment of microemulsions and their activity for photocatalytic wet oxidation of phenol. *Journal of Physical Chemistry B* **2002,** *106* (41), 10674-10679.

88. Sayilkan, F.; Erdemoglu, S.; Asilturk, M.; Akarsu, M.; Sener, S.; Sayilkan, H.; Erdemoglu, M.; Arpac, E., Photocatalytic performance of pure anatase nanocrystallite TiO2 synthesized under low temperature hydrothermal conditions. *Materials Research Bulletin* **2006,** *41* (12), 2276-2285.

89. Chan, K. Y. S.; Goh, G. K. L., Solution Epitaxy of TiO2 Thin Films. *Journal of the Electrochemical Society* **2009,** *156* (7), D231-D235.

90. Kinsinger, N. M. D., A.; Wong, A.; Kisailus, D., Synergistic Effect of pH and Phase in a Nanocrystalline Titania Photocatalyst. *Applied Materials & Interfaces* **2013,** *in review*.

91. Mazaheri, M.; Zahedi, A. M.; Haghighatzadeh, M.; Sadrnezhaad, S. K., Sintering of titania nanoceramic: Densification and grain growth. *Ceramics International* **2009,** *35* (2), 685-691.

92. Gupta, S.; Tripathi, M., A review on the synthesis of TiO2 nanoparticles by solution route. *Central European Journal of Chemistry* **2012,** *10* (2), 279-294.

93. Zhang, H. Z.; Banfield, J. F., New kinetic model for the nanocrystalline anatase-to-rutile transformation revealing rate dependence on number of particles. *American Mineralogist* **1999,** *84* (4), 528-535.

94. Harada, H.; Ueda, T., Photocatalytic activity of ultra-fine rutile in methanol-water solution and dependence of activity on particle size. *Chemical Physics Letters* **1984,** *106* (3), 229-231.

95. Lowenstam, H. A.; Weiner, S., Phosphatic Shell Plate Of The Barnacle Ibla (Cirripedia) - A Bone-Like Structure. *Proceedings of the National Academy of Sciences of the United States of America* **1992,** *89* (22), 10573-10577.

96. Addadi, L.; Moradian, J.; Shay, E.; Maroudas, N. G.; Weiner, S., A Chemical-Model for the Cooperation Of Sulfates and Carboxylates In Calcite Crystal Nucleation - Relevance to Biomineralization. *Proceedings of the National Academy of Sciences of the United States of America* **1987,** *84* (9), 2732-2736.

97. Rusenko, K. W.; Donachy, J. E.; Wheeler, A. P., Purification and Characterization Of A Shell Matrix Phosphoprotein from The American OysterPurification and Characterization Of A Shell Matrix Phosphoprotein from The American Oyster. *ACS Symposium Series* **1991,** *444*, 107-124.

98. Baskaran, S.; Song, L.; Liu, J.; Chen, Y. L.; Graff, G. L., Titanium Oxide Thin Films on Organic Interfaces through Biomimetic Processing. *Journal of the American Ceramic Society* **1998,** *81* (2), 401-408.

99. Falini, G.; Albeck, S.; Weiner, S.; Addadi, L., Control of Aragonite or Calcite Polymorphism by Mollusk Shell Macromolecules. *Science* **1996,** *271* (5245), 67-69.

100. Kenny, J. F.; Barber, N. L.; Hutson, S. S.; Linsey, K. S.; Lovelace, J. K.; Maupin, M. A., Estimated Use of Water in the United States in 2005. **2009,** (cir1344).

101. Shala, L.; Foster, G., Surface Water Concentrations and Loading Budgets of Pharmaceuticals and Other Domestic-Use Chemicals in an Urban Watershed (Washington, DC, USA). *Archives of Environmental Contamination and Toxicology* **2010,** *58* (3), 551-561.

102. Dougherty, J. A.; Swarzenski, P. W.; Dinicola, R. S.; Reinhard, M., Occurrence of Herbicides and Pharmaceutical and Personal Care Products in Surface Water and Groundwater around Liberty Bay, Puget Sound, Washington. *J. Environ. Qual.* **2010,** *39* (4), 1173-1180.

103. Sharma, V. K., Oxidative transformations of environmental pharmaceuticals by Cl-2, ClO2, O-3, and Fe(VI): Kinetics assessment. *Chemosphere* **2008,** *73* (9), 1379-1386.

104. Barnard, A. S.; Zapol, P., Predicting the Energetics, Phase Stability, and Morphology Evolution of Faceted and Spherical Anatase Nanocrystals. *The Journal of Physical Chemistry B* **2004,** *108* (48), 18435-18440.

105. Barnard, A. S.; Curtiss, L. A., Prediction of TiO2 Nanoparticle Phase and Shape Transitions Controlled by Surface Chemistry. *Nano Letters* **2005,** *5* (7), 1261-1266.

106. Barnard, A. S.; Zapol, P.; Curtiss, L. A., Anatase and rutile surfaces with adsorbates representative of acidic and basic conditions. *Surface Science* **2005,** *582* (1-3), 173-188.

107. Hoebbel, D.; Reinert, T.; Schmidt, H.; Arpac, E., On the hydrolytic stability of organic ligands in Al-, Ti- and Zr-alkoxide complexes. *Journal of Sol-Gel Science and Technology* **1997,** *10* (2), 115-126.

108. Hemmes, P.; Rich, L. D.; Cole, D. L.; Eyring, E. M., Kinetics of hydrolysis of ferric ion in dilute aqueous solution. *The Journal of Physical Chemistry* **1971,** *75* (7), 929-932.

109. Gustafson, R. L., Polymerization of metal chelates in aqueous solution. *Journal of Chemical Education* **1960,** *37* (11), 603-null.

110. Ciavatta, L.; Grimaldi, M., On the hydrolysis of the iron(III) ion, Fe3+, in perchlorate media. *Journal of Inorganic and Nuclear Chemistry* **1975,** *37* (1), 163-169.

111. Sapieszko, R. S.; Patel, R. C.; Matijevic, E., Ferric hydrous oxide sols. 2. Thermodynamics of aqueous hydroxo and sulfato ferric complexes. *The Journal of Physical Chemistry* **1977,** *81* (11), 1061-1068.

112. Flynn, C. M., Hydrolysis of inorganic iron(III) salts. *Chemical Reviews* **1984,** *84* (1), 31-41.

113. Livage, J.; Henry, M.; Sanchez, C., Sol-gel chemistry of transition metal oxides. *Progress in Solid State Chemistry* **1988,** *18* (4), 259-341.

114. Casey, W. H.; Phillips, B. L.; Nordin, J. P.; Sullivan, D. J., The rates of exchange of water molecules from Al(III)-methylmalonate complexes: the effect of chelate ring size. *Geochimica et Cosmochimica Acta* **1998,** *62* (16), 2789-2797.

115. Mockel, H.; Giersig, M.; Willig, F., Formation of uniform size anatase nanocrystals from bis(ammonium lactato)titanium dihydroxide by thermohydrolysis. *Journal of Materials Chemistry* **1999,** *9* (12), 3051-3056.

116. Hamad, S.; Catlow, C. R. A.; Woodley, S. M.; Lago, S.; Mejias, J. A., Structure and Stability of Small TiO2 Nanoparticles. *The Journal of Physical Chemistry B* **2005,** *109* (33), 15741-15748.

117. Ivanda, M.; Music, S.; Popovic, S.; Gotic, M., XRD, Raman and FT-IR spectroscopic observations of nanosized TiO2 synthesized by the sol-gel method

based on an esterification reaction. *Journal of Molecular Structure* **1999,** *480-481*, 645-649.

118. Zhou, Z.-H.; Hou, S.-Y.; Cao, Z.-X.; Wan, H.-L.; Ng, S.-W., Syntheses, crystal structures and biological relevance of glycolato and S-lactato molybdates. *Journal of Inorganic Biochemistry* **2004,** *98* (6), 1037-1044.

119. Guerrero, G.; Mutin, P. H.; Vioux, A., Mixed nonhydrolytic/hydrolytic sol-gel routes to novel metal oxide/phosphonate hybrids. *Chemistry of Materials* **2000,** *12* (5), 1268-1272.

120. Lopez, T.; Sanchez, E.; Bosch, P.; Meas, Y.; Gomez, R., FTIR and UV-Vis (diffuse reflectance) spectroscopic characterization of TiO2 sol-gel. *Materials Chemistry and Physics* **1992,** *32* (2), 141-152.

121. Ohya, T.; Ito, M.; Yamada, K.; Ban, T.; Ohya, Y.; Takahashi, Y., Aqueous Titanate Sols from Ti Alkoxide-α-Hydroxycarboxylic Acid System and Preparation of Titania Films from the Sols. *Journal of Sol-Gel Science and Technology* **2004,** *30* (2), 71-81.

122. Robinson, S. D.; Uttley, M. F., Complexes Of Platinum Metals .2. Carboxylato(Triphenylphosphine) Derivatives Of Ruthenium, Osmium, Rhodium, And IridiumComplexes Of Platinum Metals .2. Carboxylato(Triphenylphosphine) Derivatives Of Ruthenium, Osmium, Rhodium, And Iridium. *Journal of the Chemical Society-Dalton Transactions* **1973,** (18), 1912-1920.

123. Morales-Cruz, A. L.; Tremont, R.; Martínez, R.; Romañach, R.; Cabrera, C. R., Atomic force measurements of 16-mercaptohexadecanoic acid and its salt with

CH3, OH, and CONHCH3 functionalized self-assembled monolayers. *Applied Surface Science* **2005,** *241* (3-4), 371-383.

124. Bokhimi, X.; Morales, A.; Aguilar, M.; Toledo-Antonio, J. A.; Pedraza, F., Local order in titania polymorphs. *International Journal of Hydrogen Energy* **2001,** *26* (12), 1279-1287.

125. Mo, S.-D.; Ching, W. Y., Electronic and optical properties of three phases of titanium dioxide: Rutile, anatase, and brookite. *Physical Review B* **1995,** *51* (19), 13023.

126. Burdett, J. K.; Hughbanks, T.; Miller, G. J.; Richardson, J. W.; Smith, J. V., Structural-electronic relationships in inorganic solids: powder neutron diffraction studies of the rutile and anatase polymorphs of titanium dioxide at 15 and 295 K. *Journal of the American Chemical Society* **1987,** *109* (12), 3639-3646.

127. Kobayashi, M.; Tomita, K.; Petrykin, V.; Yoshimura, M.; Kakihana, M., Direct synthesis of brookite-type titanium oxide by hydrothermal method using water-soluble titanium complexes. *Journal of Materials Science* **2008,** *43* (7), 2158-2162.

128. Flory, P. J.; Mandelkern, L.; Kinsinger, J. B.; Shultz, W. B., Molecular Dimensions of Polydimethylsiloxanes. *Journal of the American Chemical Society* **1952,** *74* (13), 3364-3367.

129. Zhang, H.; Banfield, J. F., Understanding Polymorphic Phase Transformation Behavior during Growth of Nanocrystalline Aggregates: Insights from TiO2. *The Journal of Physical Chemistry B* **2000,** *104* (15), 3481-3487.

130. Penn, R. L.; Banfield, J. F., Oriented attachment and growth, twinning, polytypism, and formation of metastable phases: Insights from nanocrystalline TiO2. *American Mineralogist* **1998,** *83* (9-10), 1077-1082.

131. Penn, R. L.; Banfield, J. F., Morphology development and crystal growth in nanocrystalline aggregates under hydrothermal conditions: insights from titania. *Geochimica et Cosmochimica Acta* **1999,** *63* (10), 1549-1557.

132. Colfen, H.; Antonjeiti, M., *Mesocrystals and Nonclassical Crystallization*. CPI Antony Rowe: Chippenilam, Wiltshire, 2008.

133. Finnegan, M. P.; Zhang, H.; Banfield, J. F., Anatase Coarsening Kinetics under Hydrothermal Conditions As a Function of Ph and Temperature. *Chemistry of Materials* **2008,** *20* (10), 3443-3449.

134. Hirano, S.; Masuya, K.; Kuwabara, M., Multi-Nucleation-Based Formation of Oriented Zinc Oxide Microcrystals and Films in Aqueous Solutions. *The Journal of Physical Chemistry B* **2004,** *108* (15), 4576-4578.

135. Ma, B.; Goh, G. K. L.; Ma, J.; White, T. J., Growth Kinetics and Cracking of Liquid-Phase-Deposited Anatase Films. *Journal of the Electrochemical Society* **2007,** *154* (10), D557-D561.

136. Knauss, K. G.; Dibley, M. J.; Bourcier, W. L.; Shaw, H. F., Ti(IV) hydrolysis constants derived from rutile solubility measurements made from 100 to 300°C. *Applied Geochemistry* **2001,** *16* (9-10), 1115-1128.

137. Huang, F.; Zhang, H.; Banfield, J. F., The Role of Oriented Attachment Crystal Growth in Hydrothermal Coarsening of Nanocrystalline ZnS. *The Journal of Physical Chemistry B* **2003,** *107* (38), 10470-10475.

138. Chen, J. S.; Liu, M. C.; Zhang, L.; Zhang, J. D.; Jin, L. T., Application of nano TiO2 towards polluted water treatment combined with electro-photochemical method. *Water Research* **2003,** *37* (16), 3815-3820.

139. Jassby, D.; Farner Budarz, J.; Wiesner, M., Impact of Aggregate Size and Structure on the Photocatalytic Properties of TiO2 and ZnO Nanoparticles. *Environmental Science & Technology* **2012**.

140. Grzechulska, J.; Morawski, A. W., Photocatalytic decomposition of azo-dye acid black 1 in water over modified titanium dioxide. *Applied Catalysis B: Environmental* **2002,** *36* (1), 45-51.

141. Daneshvar, N.; Salari, D.; Khataee, A. R., Photocatalytic degradation of azo dye acid red 14 in water: investigation of the effect of operational parameters. *Journal of Photochemistry and Photobiology A: Chemistry* **2003,** *157* (1), 111-116.

142. Lachheb, H.; Puzenat, E.; Houas, A.; Ksibi, M.; Elaloui, E.; Guillard, C.; Herrmann, J.-M., Photocatalytic degradation of various types of dyes (Alizarin S, Crocein Orange G, Methyl Red, Congo Red, Methylene Blue) in water by UV-irradiated titania. *Applied Catalysis B: Environmental* **2002,** *39* (1), 75-90.

143. Suttiponparnit, K.; Jiang, J. K.; Sahu, M.; Suvachittanont, S.; Charinpanitkul, T.; Biswas, P., Role of Surface Area, Primary Particle Size, and Crystal Phase on

Titanium Dioxide Nanoparticle Dispersion Properties. *Nanoscale Research Letters* **2011,** *6*.

144. Tschirch, J.; Dillert, R.; Bahnemann, D.; Proft, B.; Biedermann, A.; Goer, B., Photodegradation of methylene blue in water, a standard method to determine the activity of photocatalytic coatings? *Research on Chemical Intermediates* **2008,** *34* (4), 381-392.

145. Sagara, T.; Iizuka, J.; Niki, K., Electroreflectance study of the redox reaction of methylene blue adsorbed on a pyrolytic graphite electrode. *Langmuir* **1992,** *8* (3), 1018-1025.

146. Henderson, M. A., A surface science perspective on photocatalysis. *Surface Science Reports* **2011,** *66* (6-7), 185-297.

147. Kosmulski, M., Compilation of PZC and IEP of sparingly soluble metal oxides and hydroxides from literature. *Advances in Colloid and Interface Science* **2009,** *152* (1-2), 14-25.

148. Kosmulski, M., pH-dependent surface charging and points of zero charge. IV. Update and new approach. *Journal of Colloid and Interface Science* **2009,** *337* (2), 439-448.

149. Jiang, Y.; Sun, Q.; Jiang, Z.; Zhang, L.; Li, J.; Li, L.; Sun, X., The improved stability of enzyme encapsulated in biomimetic titania particles. *Materials Science and Engineering: C* **2009,** *29* (1), 328-334.

150. Bullard, J. W.; Cima, M. J., Orientation Dependence of the Isoelectric Point of TiO2 (Rutile) Surfaces. *Langmuir* **2006,** *22* (24), 10264-10271.

151. Kartha, S. S.; Chacko, C. E.; Bumpous, J. M.; Fleming, M.; Lentsch, E. J.; Flynn, M. B., Toxic metabolic encephalopathy after parathyroidectomy with methylene blue localization. *Otolaryngology-Head and Neck Surgery* **2006,** *135* (5), 765-768.

152. Bach, K. K.; Lindsay, F. W.; Berg, L. S.; Howard, R. S., Prolonged postoperative disorientation after methylene blue infusion during parathyroidectomy. *Anesthesia and Analgesia* **2004,** *99* (5), 1573-1574.

153. Konstantinou, I. K.; Albanis, T. A., TiO2-assisted photocatalytic degradation of azo dyes in aqueous solution: kinetic and mechanistic investigations - A review. *Applied Catalysis B-Environmental* **2004,** *49* (1), 1-14.

154. Tschirch, J.; Bahnemann, D.; Wark, M.; Rathouský, J., A comparative study into the photocatalytic properties of thin mesoporous layers of TiO2 with controlled mesoporosity. *Journal of Photochemistry and Photobiology A: Chemistry* **2008,** *194* (2-3), 181-188.

155. Tschirch, J.; Dillert, R.; Bahnemann, D., Photocatalytic degradation of methylene blue on fixed powder layers: Which limitations are to be considered? *Journal of Advanced Oxidation Technologies* **2008,** *11* (2), 193-198.

156. Houas, A.; Lachheb, H.; Ksibi, M.; Elaloui, E.; Guillard, C.; Herrmann, J. M., Photocatalytic degradation pathway of methylene blue in water. *Applied Catalysis B-Environmental* **2001,** *31* (2), 145-157.

157. Cong, S.; Xu, Y. M., Explaining the High Photocatalytic Activity of a Mixed Phase TiO2: A Combined Effect of O-2 and Crystallinity. *Journal of Physical Chemistry C* **2011,** *115* (43), 21161-21168.

158. Bickley, R. I.; Gonzalezcarreno, T.; Lees, J. S.; Palmisano, L.; Tilley, R. J. D., A Structural Investigation of Titanium-Dioxide Photocatalysts. *Journal of Solid State Chemistry* **1991,** *92* (1), 178-190.

159. Hurum, D. C.; Agrios, A. G.; Gray, K. A.; Rajh, T.; Thurnauer, M. C., Explaining the Enhanced Photocatalytic Activity of Degussa P25 Mixed-Phase TiO2 Using EPR. *The Journal of Physical Chemistry B* **2003,** *107* (19), 4545-4549.

160. Sun, B.; Vorontsov, A. V.; Smirniotis, P. G., Role of platinum deposited on TiO2 in phenol photocatalytic oxidation. *Langmuir* **2003,** *19* (8), 3151-3156.

161. Liqiang, J.; Xiaojun, S.; Jing, S.; Weimin, C.; Zili, X.; Yaoguo, D.; Honggang, F., Review of surface photovoltage spectra of nano-sized semiconductor and its applications in heterogeneous photocatalysis. *Solar Energy Materials and Solar Cells* **2003,** *79* (2), 133-151.

162. Torimoto, T.; Nakamura, N.; Ikeda, S.; Ohtani, B., Discrimination of the active crystalline phases in anatase-rutile mixed titanium(iv) oxide photocatalysts through action spectrum analyses. *Physical Chemistry Chemical Physics* **2002,** *4* (23), 5910-5914.

163. Ohno, T.; Sarukawa, K.; Matsumura, M., Crystal faces of rutile and anatase TiO2 particles and their roles in photocatalytic reactions. *New Journal of Chemistry* **2002,** *26* (9), 1167-1170.

164. Zhang, H. Z.; Banfield, J. F., Size dependence of the kinetic rate constant for phase transformation in TiO2 nanoparticles. *Chemistry of Materials* **2005,** *17* (13), 3421-3425.

165. Kinsinger, N.; Tantuccio, A.; Sun, M.; Yan, Y.; Kisailus, D., Photocatalytic Titanium Dioxide Composite. *Journal of Nanoscience and Nanotechnology* **2011,** *11* (8), 7015-7021.

166. Fang, X. M.; Zhang, Z. G.; Chen, Q. L., Nitrogen doped TiO2 photocatalysts with visible-light activity. *Progress in Chemistry* **2007,** *19* (9), 1282-1290.

167. Zhao, B.; Chen, F.; Jiao, Y.; Zhang, J., Phase transition and morphological evolution of titania/titanate nanomaterials under alkalescent hydrothermal treatment. *Journal of Materials Chemistry* **2010,** *20* (37), 7990-7997.

168. Miyauchi, M.; Tokudome, H., Low-reflective and super-hydrophilic properties of titanate or titania nanotube thin films via layer-by-layer assembly. *Thin Solid Films* **2006,** *515* (4), 2091-2096.

169. Peppas, N. A.; Merrill, E. W., Differential scanning calorimetry of crystallized PVA hydrogels. *Journal of Applied Polymer Science* **1976,** *20* (6), 1457-1465.

170. Kumar, K.-N. P.; Keizer, K.; Burggraaf, A. J., Textural evolution and phase transformation in titania membranes: Part 1.-Unsupported membranes. *Journal of Materials Chemistry* **1993,** *3* (11), 1141-1149.

171. Lam, R. C. W.; Leung, M. K. H.; Leung, D. Y. C.; Vrijmoed, L. L. P.; Yam, W. C.; Ng, S. P., Visible-light-assisted photocatalytic degradation of gaseous

formaldehyde by parallel-plate reactor coated with Cr ion-implanted TiO2 thin film. *Solar Energy Materials and Solar Cells* **2007,** *91* (1), 54-61.

172. Ao, C. H.; Lee, S. C.; Yu, J. C., Photocatalyst TiO2 supported on glass fiber for indoor air purification: effect of NO on the photodegradation of CO and NO2. *Journal of Photochemistry and Photobiology A: Chemistry* **2003,** *156* (1-3), 171-177.

173. Ohtani, B.; Ogawa, Y.; Nishimoto, S.-i., Photocatalytic Activity of Amorphous Anatase Mixture of Titanium(IV) Oxide Particles Suspended in Aqueous Solutions. *The Journal of Physical Chemistry B* **1997,** *101* (19), 3746-3752.

174. Svadlak, D.; Shanelova, J.; Malek, J.; Perez-Maqueda, L. A.; Criado, J. M.; Mitsuhashi, T., Nanocrystallization of anatase in amorphous TiO2. *Thermochimica Acta* **2004,** *414* (2), 137-143.

175. Xie, H.; Zhang, Q.; Xi, T.; Wang, J.; Liu, Y., Thermal analysis on nanosized TiO2 prepared by hydrolysis. *Thermochimica Acta* **2002,** *381* (1), 45-48.

Appendix.
Investigation of Processing Parameters for Enhanced Membrane Structural Integrity

Introduction.

Existing water and wastewater treatment facilities are mostly designed for the removal of the well-known "priority" pollutants specified in current regulations [1, 2]. Powder Activated Carbon (PAC), chlorination, and ozonation have demonstrated a high removal efficiency [2, 3]. However, PAC is known to adsorb the organic compounds, but does not induce degradation. Instead, PAC transfers the contaminants to a new phase [2, 4, 5]. Chlorination is a common oxidant used, but produces chlorinated by-products that may be more dangerous than the original contaminant [3, 6]. EDCs and PPCPs have been found in drinking water sources on the order of μg/L to n/L, indicating that the current wastewater treatment technologies are not adequately removing these compounds causing increasing concern for public health and safety [2, 7, 8].

Photocatalysts have been proven to effectively mineralize a wide range of organic species. Titanium dioxide (TiO_2) is the most common photocatalytic material because it is inexpensive, abundant, photostable, and non-toxic [4, 5, 9]. Beyond photocatalysis, we have developed a porous composite material (as described elsewhere)[10] that has a wide variety of applications and commercialization potential since it maintains high surface area, but unlike nanoparticle suspensions, does not requiring a downstream recovery process. These recovery processes are necessary in photocatalytic reactors that use suspended solids or slurry reactor technologies, resulting in intensive capital investment and operating costs. The elimination of a nanoparticle recovery step will not only reduce the operating costs of a photocatalytic system for water treatment, but will make this process economically feasible for a wide variety of applications.

The photocatalytically active TiO_2 membrane is intended for end user applications such as under-cabinet or refrigerator water filters for residential or small businesses needs. This technology will reduce the public exposure to organic pollutants that are persistent even after tradition wastewater treatments, environmental degradation mechanisms, and/or drinking water treatments. The end-user application will also reduce concerns about deterioration of water quality (i.e., existence of industrial and pharmaceutical compounds) due to aquifer recharge, discharge into waterways, and water recycling in regions with limited fresh water resources [11].

Our objective is to develop a point of use scale prototype capable of treating a minimum capacity of 0.8 gpm under 80 psig water pressure, which is representative of residential drinking water systems [12]. There are still several limitations that must be overcome to achieve a functional photocatalytic membrane prototype. One significant limitation of this material is the enhancement of its structural integrity. As a flow-through membrane, the material must be able to withstand the sustained and applied compressive pressures of the water in a flow-through system. Optimization of this membrane must be achieved in order to withstand the sustained and applied compressive pressures (i.e., 100 psig) of the water in a flow-through system, while maintaining porosity. Another limitation is increasing and controlling porosity within the membrane while maintaining its structural integrity. Here, we aim to minimize the backpressures caused by the presence of a membrane, while increasing the accessible surface area (i.e., photocatalytically active sites).

Materials and Methods.

TiO_2-organic composites were chemically synthesized by mixing polyvinyl alcohol (PVA, MW ~ 40,000, 98-99%, Sigma Aldrich), ball milled to particle size less than 100mesh, with a TiBALDH solution and processing under hydrothermal conditions. Here, TiBALDH and PVA solutions were combined to make a 1M Ti solution (molar ratio PVA:TiBALDH = 1:100) at pH = 9, as previously described[10]. Immediately following pH modification, solutions were placed in Pyrex glass test tubes, sealed, and heated at 150°C for 12 hours. Following synthesis, the resulting rigid, viscoelastic composites were cut into discs and then dehydrated using ethanol to remove absorbed water while maintaining their structural integrity. Subsequently, the green materials were heated to 800°C at 10°C/min and held for 1 hour under flowing air ($100cm^3/min$). This annealing process was used to remove the organic template and yield a high surface area TiO_2 nanocrystalline ceramic network. Subsequent reactions were carried out on the porous membranes using the TiBALDH precursor under acid conditions in a hydrothermal reactor (i.e., membranes placed within reactor during secondary synthesis) at 200°C for 3 hours.

Material Characterization.

TiO_2 specimens were characterized using X-Ray Diffraction (XRD) and Scanning Electron Microscopy (SEM). Phase identification was determined by XRD (Rigaku Smartlab) using Cu $K\alpha$ radiation. The relative composition of crystalline rutile was determined via the following equation (equation 1):

$$x_r = \frac{I_R}{I_R + 0.884 I_A} \quad (1)$$

where, I_A and I_R are the integrated intensities of anatase (101) and rutile (110) peaks, respectively [13]. Specimens were observed using SEM imaging (FEI X-30, Netherlands) was used to characterize the morphology and particle size. TiO_2-polymer composite samples were mounted with conductive adhesive on pin studs (Ted Pella, Redding, CA). The samples were then sputter coated with Pt-Pd for 30 seconds.

Results and Discussions.

It is known that enhancing particle packing with minor amounts of particle bridging via sintering necks percolated throughout the structure will enhance the body strength [14]. Increasing the TiO_2 loading while optimizing annealing conditions to induce particle necking should increase the durability and compressive strength of the material [14]. The SEM micrograph in Figure 44 reveals spherulites consisting of rutile rods growing off of the surface of the membrane. This increases the connectivity of the particles within the membrane, which should result in an increased strength, without filling in the pores. XRD analysis (Figure 43) reveals an increase in the percentage of rutile (37.0 ± 3.9% rutile) after the secondary growth as compared to 10.6 ± 6.0% rutile in the membranes prior to the secondary growth that were fired at 800°C, 1 hour, $100 cm^3/min$. The increase in the percentage of rutile within the membranes after the secondary growth is due to the growth of the rutile rods on the surface of the membrane.

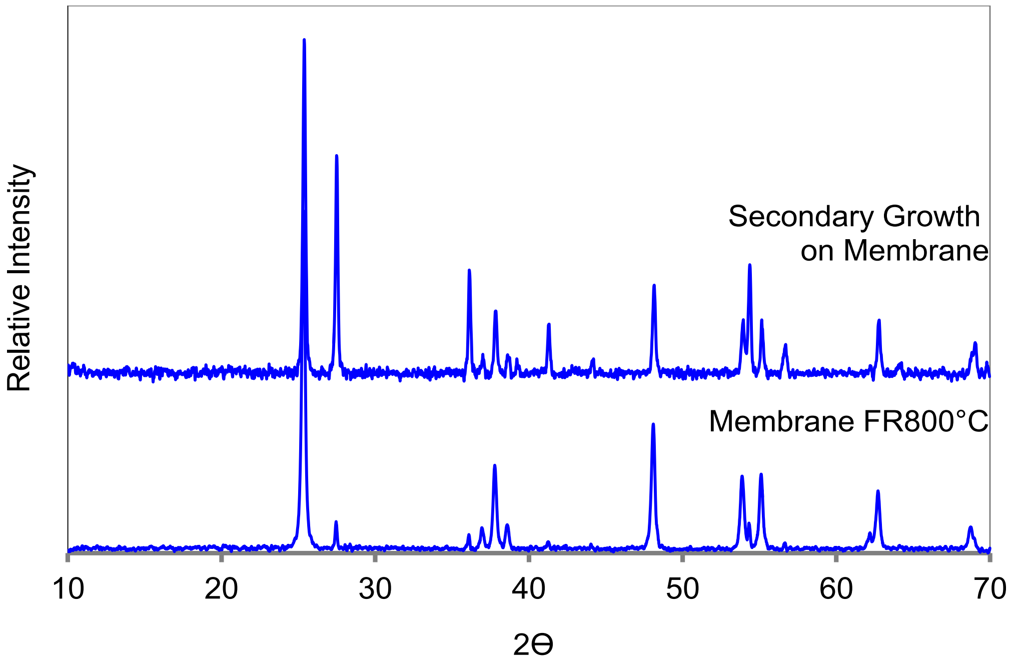

Figure 43: X-ray diffraction of membrane (fired at 800°C, 1 hour, 100cm^3/min) prior to secondary growth and after secondary growth at 200°C for 3 hours under acidic solution conditions.

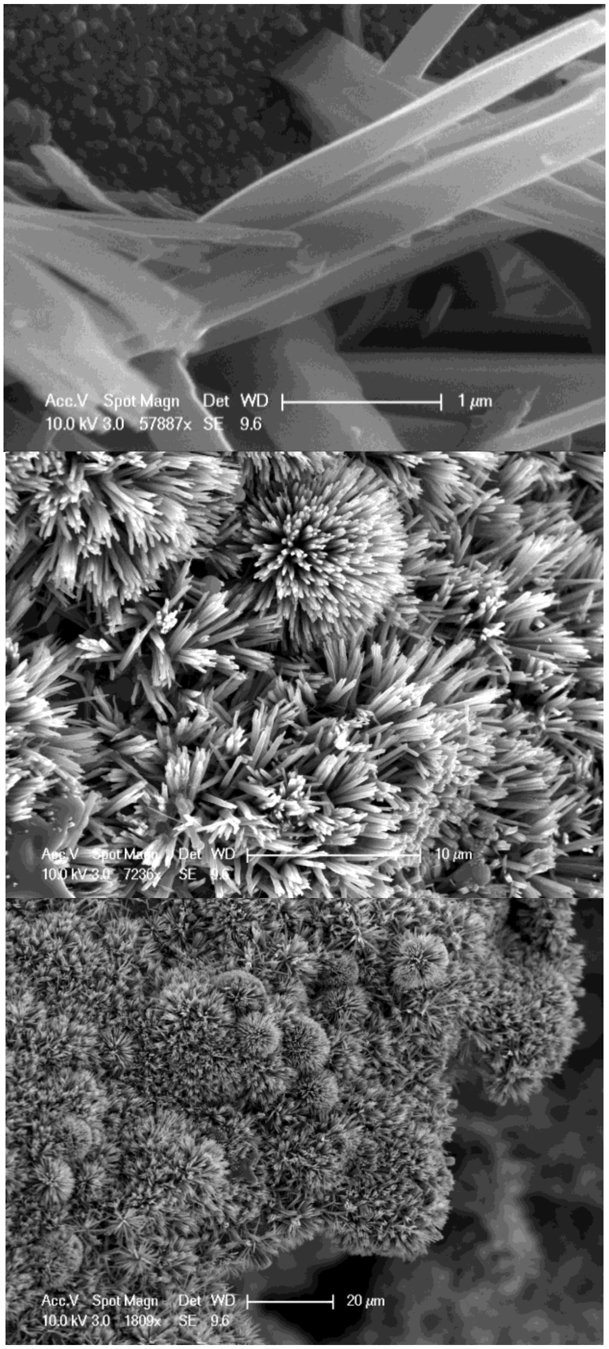

Figure 44: Scanning Electron Micrographs of membrane following secondary growth at 200°C for 3 hours under acidic solution conditions and subsequent firing at 800°C for 1 hour in air.

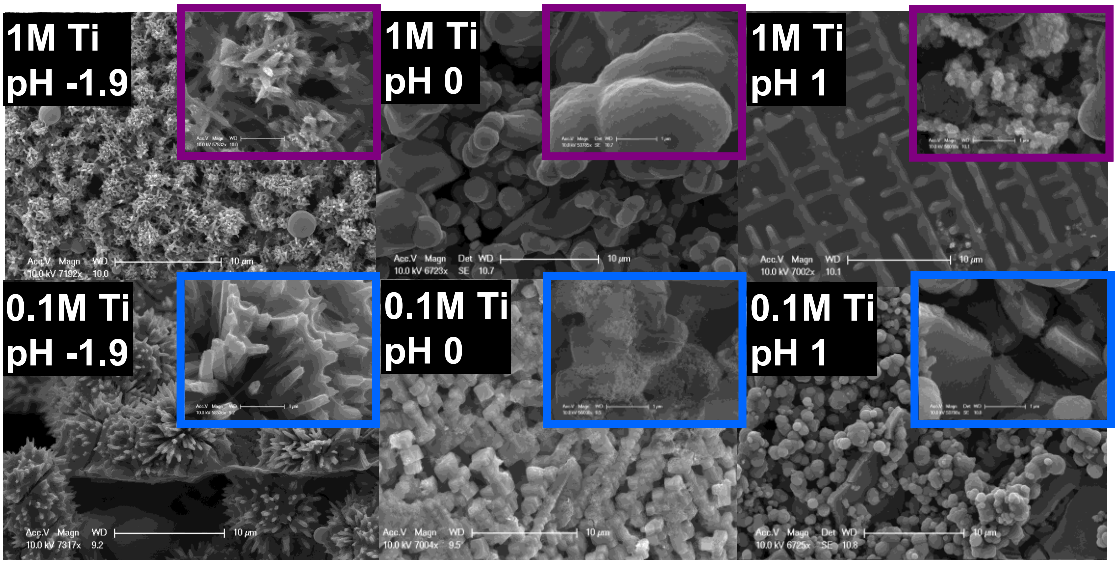

Figure 45: Scanning Electron Micrograph of nanoparticles prepared by hydrothermal synthesis for 3 hours at 200°C under acidic conditions.

Syntheses performed without the presence of the membrane result in similar morphologies (i.e., spherulites) under the acidic conditions, similar to that seen by Li et al. using an alkoxide precursor[15]. However, without the presence of the membrane, a ~20 micron thick film is formed consisting of rutile rods (Figure 45). Under this extremely low pH and at low precursor concentration, rutile is the favored phase due to the complexation of the chloride ion with the titanium center (Figure 46) [15, 16], which restricts the formation of edge sharing bonds required to form anatase. Increasing the pH or precursor concentration results in a combination of anatase, brookite, and rutile phases with a very different morphology (Figure 45 and Figure 46). This is due to the increased concentration of water at higher pHs (i.e., pH = 0, 1) and the reduced ratio of chloride ions to precursor, increasing the probability of hydroxyl ligands interacting with the titanium centers and thus, enabling condensation along octahedral edges to form anatase[16, 17].

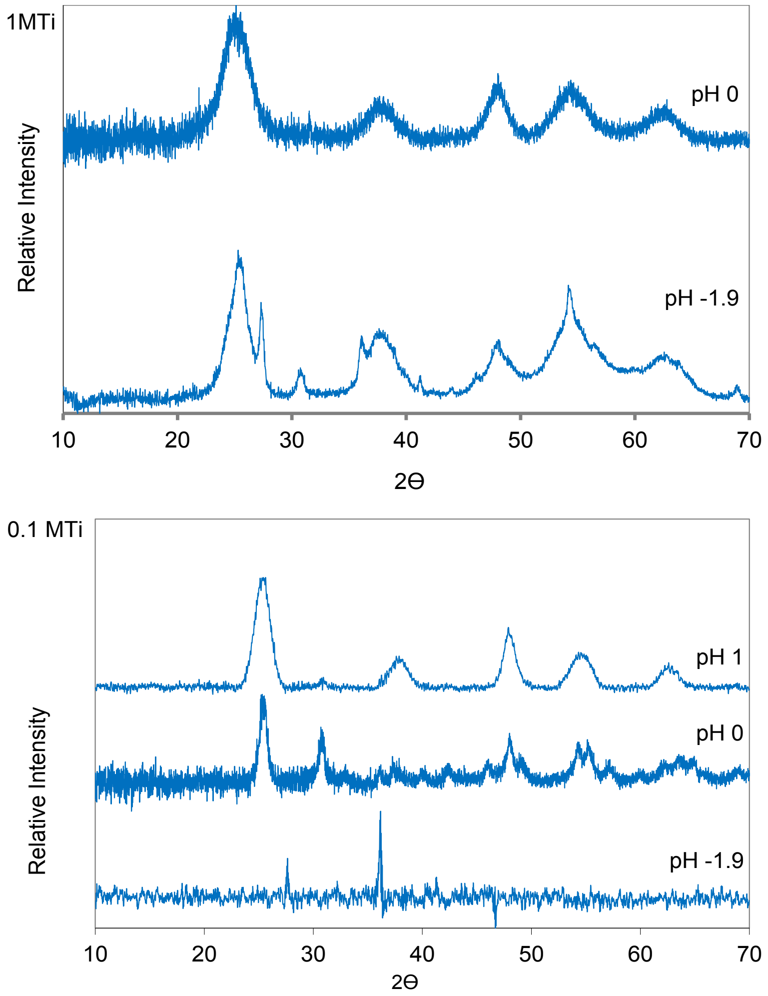

Figure 46: X-ray diffraction of nanoparticles prepared by hydrothermal synthesis for 3 hours at 200°C under acidic conditions

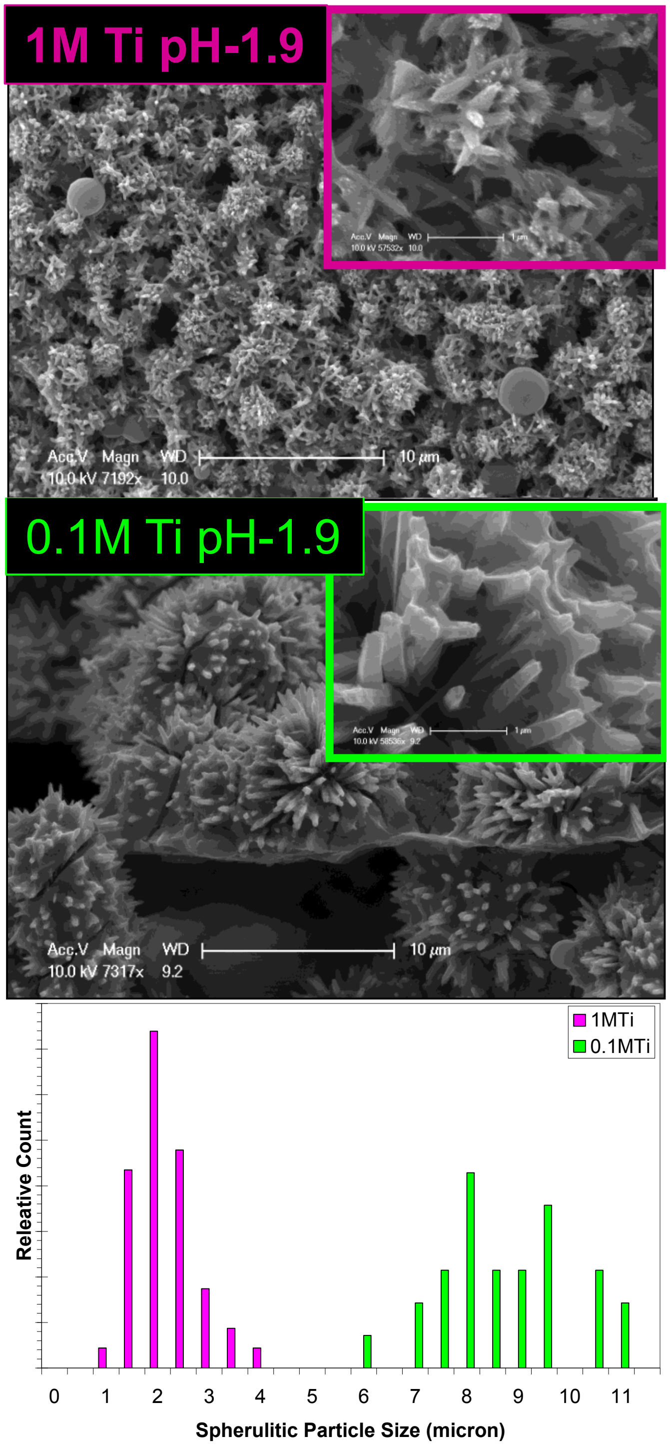
1M Ti pH-1.9
Acc.V Magn WD 10 µm
10.0 kV 7192x 10.0
Acc.V Magn WD 1 µm
0.1M Ti pH-1.9
Acc.V Magn WD 10 µm
10.0 kV 7317x 9.2
Acc.V Magn WD 1 µm
1MTi
0.1MTi
Releative Count
0
1
2
3
4
5
6
7
8
9
10
11
Spherulitic Particle Size (micron)

Figure 47: Scanning Electron Micrograph of nanoparticles prepared by hydrothermal synthesis for 3 hours at 200°C under acidic conditions (without membrane, on the left) and particle size distribution of the corresponding preparation conditions (on the right).

Particle size analysis of samples (i.e., spherulitic particles composed of rods) prepared under acidic conditions at 1M TiBALDH and 0.1M TiBALDH, respectively (Figure 47) reveal that reduced precursor concentration increases the particle size. This is expected, in agreement with previous studies, which is indicative of a higher number of nuclei that form at higher precursor concentrations facilitating the formation of more spherulites [16]. A similar result is observed when the pH is reduced. Rutile rods are observed under both pH conditions at the 0.5M TiBALDH precursor concentration. However, there is a significant difference in particle diameter. Increasing the relative concentration of chloride ions to TiBALDH molecules restricts the nucleation rate (Figure 48).

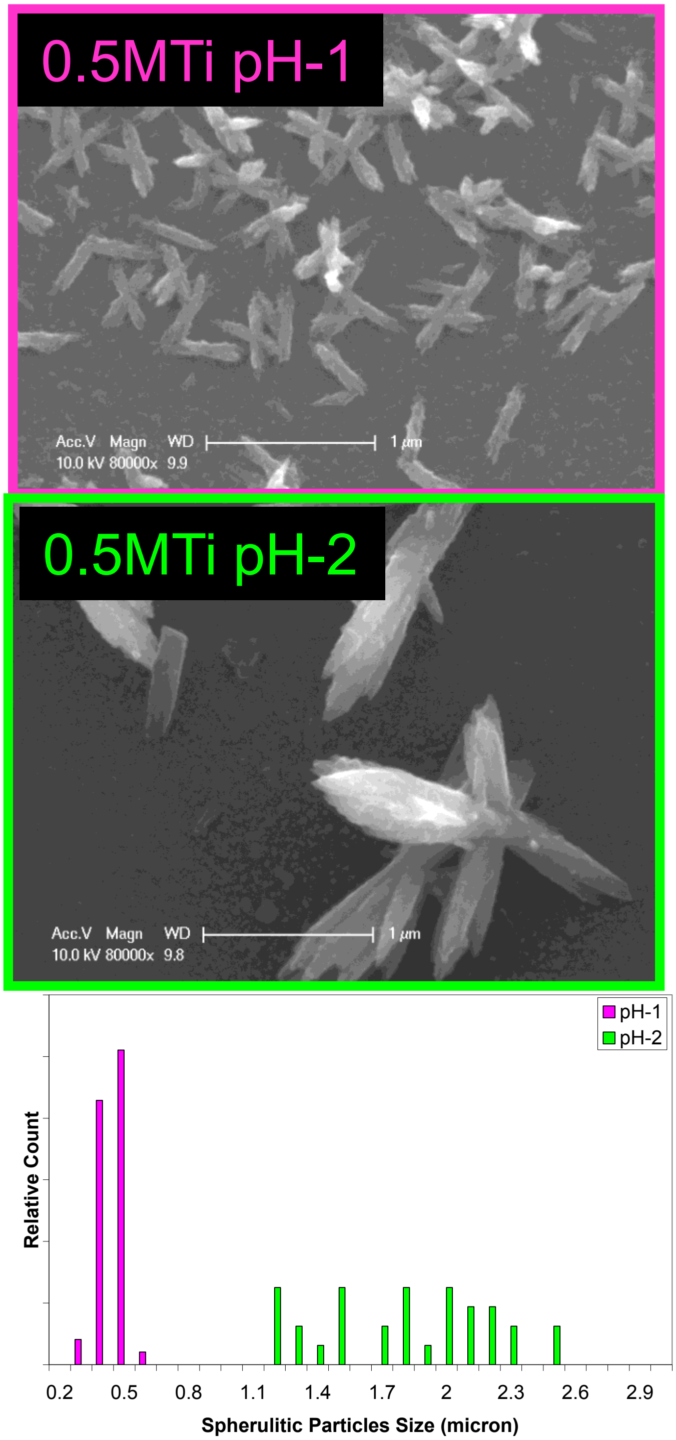

Figure 48: Scanning Electron Micrograph of TiO_2 nanoparticles prepared by hydrothermal synthesis for 3 hours at 200°C under acidic conditions.

Conclusions.

To improve the structural integrity of the porous photocatalytic membrane, which is intended for use in such applications as point of use residential or small commercial application, the use of secondary syntheses and acid synthesis conditions were initiated. The membrane will need to withstand water pressures on the order of 80 psig, which is representative of residential drinking water systems [12]. The secondary synthesis, using the TiBALDH precursor, under acidic conditions, may improve the strength of the membrane as well as increase the relative concentration TiO_2 within the membrane. This also increased the rutile content within the membrane, which may improve photocatalytic activity due to the synergistic effect between anatase and rutile. Nanoparticles synthesized in the absence of the membrane resulted in rutile at 0.1M TiBALDH and pHs ≤ 0 while anatase and brookite were observed between pH 0 and 2 at both 1M and 0.1M TiBALDH . At pH > 1 and 0.1M TiBALDH, only anatase is observed. Finally, it was observed that pH also controlled the particle diameter. This is likely due to different complexes of Ti ions forming, which will affect their efficacy in condensation reactions. Future work will involve further investigation of this effect as well as quantitative analysis of strength and photocatalytic activity of membranes containing TiO_2 from secondary growth processes described here.

Appendix References.

1. Falconer, I. R.; Chapman, H. F.; Moore, M. R.; Ranmuthugala, G., Endocrine-disrupting compounds: A review of their challenge to sustainable and safe water supply and water reuse. *Environmental Toxicology* **2006,** *21* (2), 181-191.
2. Bolong, N.; Ismail, A. F.; Salim, M. R.; Matsuura, T., A review of the effects of emerging contaminants in wastewater and options for their removal. *Desalination* **2009,** *239* (1-3), 229-246.
3. Westerhoff, P.; Yoon, Y.; Snyder, S.; Wert, E., Fate of Endocrine-Disruptor, Pharmaceutical, and Personal Care Product Chemicals during Simulated Drinking Water Treatment Processes. *Environmental Science & Technology* **2005,** *39* (17), 6649-6663.
4. Das, D. P.; Baliarsingh, N.; Parida, K. M., Photocatalytic decolorisation of methylene blue (MB) over titania pillared zirconium phosphate (ZrP) and titanium phosphate (TiP) under solar radiation. *Journal of Molecular Catalysis A: Chemical* **2007,** *261* (2), 254-261.
5. Li Puma, G.; Puddu, V.; Tsang, H. K.; Gora, A.; Toepfer, B., Photocatalytic oxidation of multicomponent mixtures of estrogens (estrone (E1), 17[beta]-estradiol (E2), 17[alpha]-ethynylestradiol (EE2) and estriol (E3)) under UVA and UVC radiation: Photon absorption, quantum yields and rate constants independent of photon absorption. *Applied Catalysis B: Environmental* **2010,** *99* (3-4), 388-397.

6. Richardson, S. D.; Thruston, A. D.; Collette, T. W.; Patterson, K. S.; Lykins, B. W.; Ireland, J. C., Identification of TiO2/UV disinfection byproducts in drinking water. *Environmental Science & Technology* **1996,** *30* (11), 3327-3334.

7. Buerge, I. J.; Buser, H. R.; Poiger, T.; Muller, M. D., Occurrence and fate of the cytostatic drugs cyclophosphamide and ifosfamide in wastewater and surface waters. *Environmental Science & Technology* **2006,** *40* (23), 7242-7250.

8. Carballa, M.; Omil, F.; Lema, J. M.; Llompart, M.; García-Jares, C.; Rodríguez, I.; Gómez, M.; Ternes, T., Behavior of pharmaceuticals, cosmetics and hormones in a sewage treatment plant. *Water Research* **2004,** *38* (12), 2918-2926.

9. Li Puma, G.; Brucato, A., Dimensionless analysis of slurry photocatalytic reactors using two-flux and six-flux radiation absorption-scattering models. *Catalysis Today* **2007,** *122* (1-2), 78-90.

10. Kinsinger, N.; Tantuccio, A.; Sun, M. W.; Yan, Y. S.; Kisailus, D., Photocatalytic Titanium Dioxide Composite. *Journal of Nanoscience and Nanotechnology* **2011,** *11* (8), 7015-7021.

11. Sharma, V. K., Oxidative transformations of environmental pharmaceuticals by Cl-2, ClO2, O-3, and Fe(VI): Kinetics assessment. *Chemosphere* **2008,** *73* (9), 1379-1386.

12. Guidelines, W. P., H**igh-Efficiency Lavatory Faucet Specification**. **2007**.

13. Zhang, H. Z.; Banfield, J. F., Phase transformation of nanocrystalline anatase-to-rutile via combined interface and surface nucleation. *Journal of Materials Research* **2000,** *15* (2), 437-448.

14. Mackenzie, J. D.; Ulrich, D. R., *Ultrastructure processing of advanced ceramics*. 1988; p Medium: X; Size: Pages: (1043 p).

15. Li, D.; Soberanis, F.; Fu, J.; Hou, W.; Wu, J.; Kisailus, D., Growth mechanism of highly branched titanium dioxide nanowires via oriented attachment. *Crystal Growth & Design* **2013,** *13* (2), 422-428.

16. Cheng, H. M.; Ma, J. M.; Zhao, Z. G.; Qi, L. M., Hydrothermal Preparation of Uniform Nanosize Rutile and Anatase Particles. *Chemistry of Materials* **1995,** *7* (4), 663-671.

17. Kinsinger, N. M.; Wong, A.; Li, D.; Villalobos, F.; Kisailus, D., Nucleation and Crystal Growth of Nanocrystalline Anatase and Rutile Phase TiO2 from a Water-Soluble Precursor. *Crystal Growth & Design* **2010,** *10* (12), 5254-5261.